



UNIVERSITÀ DEGLI STUDI DI MILANO

FACOLTÀ DI SCIENZE E TECNOLOGIE

Corso di Laurea Triennale in Fisica

Tesi di Laurea Triennale in Fisica

**Measurement of the electrons faking photons
background searching for Dark Matter in the
mono-photon channel with 140 fb^{-1} of pp collisions
recorded by the ATLAS detector.**

P.A.C.S. 14.80.-j

Relatore interno: Prof. Leonardo CARMINATI
Correlatori: Dott. Stefano MANZONI
Dott.ssa Silvia RESCONI

Tesi di Laurea di:
Laura NASELLA
Matr. 886561

Anno Accademico 2018 - 2019

Contents

1	Dark Matter	7
1.1	Evidences of the existence of Dark Matter	8
1.1.1	The rotation curves of spiral galaxies	8
1.1.2	The motion of galaxies in a cluster	9
1.1.3	The presence of gas in some clusters	9
1.1.4	Gravitational lensing	9
1.1.5	Cosmological evidence	10
1.2	Dark Matter candidates	11
1.2.1	WIMPs	12
1.3	Detection of Dark Matter	13
1.3.1	Indirect methods	13
1.3.2	Direct methods	14
1.3.3	Search at colliders	15
2	LHC and ATLAS	17
2.1	The Large Hadron Collider	17
2.1.1	CERN accelerator complex and LHC structure	17
2.1.2	Proton-proton interactions and luminosity	19
2.2	The ATLAS experiment	23
2.2.1	The Inner Detector	24
2.2.2	The Calorimeters	26
2.2.3	The Muon Spectrometer	28
2.2.4	The trigger system	28
3	Electrons and photons reconstruction with the ATLAS detector	30
3.1	Energy clusters and track reconstruction	30
3.1.1	Energy clusters in the Electromagnetic Calorimeter	30
3.1.2	Track reconstruction and matching	31
3.2	Electrons	32
3.2.1	Reconstruction	32
3.2.2	Identification	32
3.2.3	Isolation	33
3.3	Photons	33
3.3.1	Reconstruction	33
3.3.2	Mis-reconstruction of electrons as photons	36
3.3.3	Identification	37
3.3.4	Isolation	38

4	The Mono-Photon analysis	40
4.1	Overview	40
4.2	Event selection	40
4.2.1	Pre-selection of events	41
4.2.2	Object definition	41
4.2.3	Event selection in the Signal Region	42
4.3	Background estimation	43
4.3.1	Background sources	43
4.3.2	Control Regions	44
4.3.3	Monte-Carlo simulations and the simultaneous fit technique	45
4.3.4	Fake- γ background estimation	46
4.4	Results	47
5	Measurement of the electrons faking photons background for the Mono-Photon analysis	50
5.1	The electron-to-photon fake rate	50
5.1.1	Definition of the e-to- γ fake rate	50
5.1.2	Event selection, Overlap Removal and selection of the <i>best couple</i>	52
5.1.3	Invariant mass distributions for the fake rate estimation	53
5.1.4	Background subtraction	57
5.1.5	Systematic uncertainties	60
5.1.6	Results	62
5.2	Background from electrons faking photons	76
6	Conclusions	78

Introduction

The existence of Dark Matter (DM) is well established by several astrophysical and cosmological observations: all these evidences agree on the fact that the ordinary matter, composed of Standard Model (SM) particles, cannot account for the total mass and energy in our Universe. Despite this fact, the nature of DM is still unknown. One of the most popular DM candidates is a Weakly Interacting Massive Particle (WIMP): WIMPs are neutral stable particles with a mass between 10 GeV to 1 TeV that interact weakly with SM particles. WIMPs are the most credited candidates on the nature of DM for various reasons: one of the most compelling is that stable particles, whose mass belongs to the WIMPs range with an interaction cross section with SM particles of the order of the weak scale, would account exactly for the amount of relic density of DM in the Universe measured by cosmology experiments.

To detect DM, especially WIMPs, several direct and indirect detection strategies have been designed; searches at colliders play a crucial role in this quest because, in principle, WIMPs could be produced in high energy pp collisions such as those that happen at the Large Hadron Collider (LHC). Dedicated searches for DM are therefore performed with the ATLAS experiment at the LHC: however, being WIMPs electrically neutral and weakly interacting with SM particles, they would not leave any detectable trace in the ATLAS detectors. Since the total transverse momentum in a pp collision is expected to be zero, DM particles would manifest themselves as a missing transverse momentum (E_T^{miss}), but only if they are produced in association with a detectable SM object, necessary to tag the event. These searches are called Mono-X where X is the SM particle (jet, photon, W/Z or Higgs bosons) used to tag the event: they look for an excess of events with the mono-X signature in a dedicated signal region with respect to SM processes with the same signature. The Mono-Photon analysis fits in the Mono-X framework, searching for events where the final state is characterized by a high p_T photon and large E_T^{miss} . This $E_T^{miss} + \gamma$ final state is relatively clean since only few processes exhibit such a final state in the SM. The evaluation of the background yields for the Mono-Photon analysis follows two different paths, whether the considered background source belongs to real- γ backgrounds such as $Z \rightarrow \nu\nu + \gamma$ or $W + \gamma$ events, or fake- γ backgrounds such as $W + \text{jet}$ or $Z + \text{jet}$ events where a jet or an e^- is misidentified as γ . Background yields from real- γ sources are predicted by Monte-Carlo (MC) simulations and are rescaled with a data-to-simulation ratio determined primarily in Control Regions (CRs), orthogonal to the Signal Region (SR) of the analysis, defined such that they are dominated by a single background process. However, the estimation of the yields of the two fake- γ backgrounds, electrons faking photons and jets faking photons, cannot rely on MC predictions because they cannot accurately reproduce photon reconstruction failures.

The work presented in this thesis consists in providing a new estimation of the background from electrons faking photons using data collected by the ATLAS detector between 2015 and 2018 (Run 2). Although the reconstruction algorithm for electrons and photons is designed to minimize ambiguities and to avoid misreconstruction of electrons as photons, a small fraction of electrons mistakenly reconstructed and identified as photons contaminates the

Signal Region of the Mono-Photon analysis. To estimate the number of such electron fakes, a two-step approach is employed. The first step consists in evaluating the *electron-to-photon fake rate* that can be seen as the probability for true electrons to be mistakenly reconstructed and identified as photons. The measurement of the fake rate is performed selecting $Z \rightarrow ee$ decays, where the two electrons in the final state can be reconstructed either as a ee or as a $e\gamma$ couple, where the γ is a fake photon. The ratio of reconstructed $e\gamma$ yields to reconstructed ee yields provides an estimation of the electron-to-photon fake rate. The e -to- γ fake rate is measured as a function of the pseudorapidity η and as a function of the transverse momentum p_T in different $|\eta|$ intervals. The second step consists in using the e -to- γ fake rate to compute the number of electron fakes for every region of the Mono-Photon analysis. For each region of the analysis an additional CR, the probe-electron CR, is defined: the probe- e CR is defined in the same way as the corresponding CR of the analysis, except that the requirements on the photon are replaced with a request to have an electron. The yield of electron fakes in each region of the analysis is the event yield in the corresponding probe- e CR rescaled with the e -to- γ fake rate.

This thesis is organized as follows. The first Chapter provides an overview of the quest for Dark Matter, including an introduction on the possible searches at colliders. In the second Chapter, the Large Hadron Collider and the ATLAS experiment are described. The reconstruction algorithm responsible for the parallel reconstruction of electrons and photons with the ATLAS detector is the focus of the third Chapter; a brief introduction on identification and isolation of electrons and photons is also present. The fourth Chapter presents the Mono-Photon analysis. The fifth Chapter includes a description of the methodology employed to measure the electron-to-photon fake rate and presents the electrons faking photons background yield for the Mono-Photon analysis obtained with the above-mentioned measurement. The conclusions are summarized in the sixth and final Chapter.

1 Dark Matter

In the 20th century physicists understood that everything in the universe is made from a few basic building blocks called elementary particles and that their interactions are governed by four fundamental forces. This understanding resulted in the creation of the Standard Model (SM) of particle physics (Figure 1), a gauge theory based on the local symmetry structure $SU(3)_C \times SU(2)_L \times U(1)_Y$ that describes the fundamental structure of matter, three of the four fundamental forces and predicts other important phenomena. Elementary particles are all *fermions*, thus they have half-integer spin, in particular $1/2$; they are divided in two groups called *quarks* and *leptons*. The six quarks are paired in three generations: the up quark and the down quark, the charm quark and strange quark and the top quark and bottom (or beauty) quark. The six leptons are similarly arranged in three generations: the electron and the electron neutrino, the muon and the muon neutrino and the tau and the tau neutrino. The four fundamental interactions are the strong force, the weak force, the electromagnetic force and the gravitational force: they work over different ranges and have different strengths. The first three are described by the SM and result from the exchange of force-carrier particles called *gauge bosons*: the strong interaction is mediated by the gluons, the electromagnetic force by the photons and the weak force by the W^+, W^- and Z bosons. The last particle in the SM is the *Higgs boson* H, which was hypothesized in 1964 to explain the mass of the massive gauge bosons and of the other fundamental particles and then detected in 2012 by the ATLAS and CMS experiments at the Large Hadron Collider [6] [7].

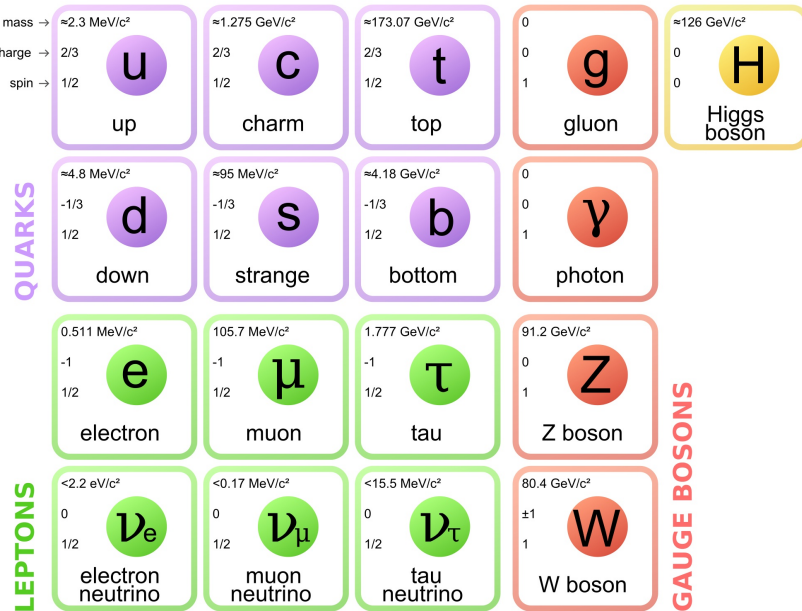


Figure 1: The Standard Model of particle physics.

However there are arguments indicating that the SM cannot be the ultimate model to describe our Universe, like the fact that the gravitational force is not described by the Standard Model. In addition experimental evidences from astrophysical observations (Section 1.1) led scientists to believe that something we have yet to detect directly is giving galaxies extra mass, in addition to the visible one we can measure. This strange matter was called Dark Matter since it does not interact with the electromagnetic radiation and thus it does not absorb, reflect or emit light. From the last observations, only 4% of the Universe is composed of visible ordinary matter, 23% of it is Dark Matter and the remaining 73% is Dark Energy. Since the nature of Dark Matter is still unknown, there are some candidates (some of them are more likely than the others, i.e. WIMPs, *Weakly Interacting Massive Particles*) and they will be discussed in Section 1.2. Dark Matter particles could be produced in pp collisions at the LHC (only if Dark Matter couples with ordinary matter): they would traverse the detectors without leaving any visible trace, but one possible sign of their existence would be an excess of events with a high energetic photon accompanied by missing transverse momentum (MET) with respect to the SM prediction (Section 1.3).

1.1 Evidences of the existence of Dark Matter

By now, there are compelling indirect gravitational and cosmological evidences of the existence of Dark Matter; the most important among them will be briefly illustrated in this section.

1.1.1 The rotation curves of spiral galaxies

The Westerbork Synthesis Radio Telescope (WSRT) [18] was completed in 1970 because physicists wanted to observe the dynamics of rotation of spiral galaxies: by studying them as disks, it is possible to model their *rotation curves*, the circular velocity profile $v(R)$ of the objects (stars, gas) in a galaxy as a function of their distance from the center of the galaxy. From the simple Newtonian dynamics, the centripetal force of the object of mass m is equal to the gravitational force between the considered object and the galaxy (of mass $M(R)$), $F_c = F_g$:

$$\frac{mv^2}{R} = \frac{GmM(R)}{R^2}, \quad (1)$$

thus leading to an expected power law $v(R) \sim \frac{1}{\sqrt{R}}$, known as *Keplerian decrease*. The observed rotation curves however show a flat behaviour, $v(R) \sim \text{constant}$, up to distances R greater than the galaxies' visible radius. They explained the experimental results by hypothesizing that a hidden Dark Matter halo is present in the outer region of galaxies. The fact that the rotation curves are flat therefore means that the distribution of the mass of the galaxies is $M(R) \sim R$. Figure 2 shows the expected and observed rotational curve of the spiral galaxy NGC 3198 and the dark halo contribution. This was a first clue that not all the galaxies' matter is visible.

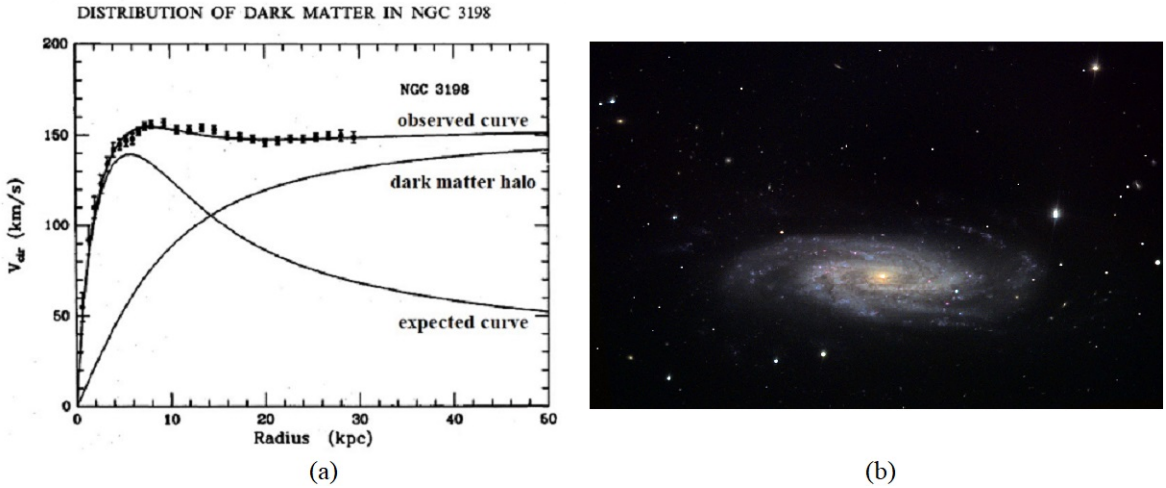


Figure 2: (a): The rotational curve of the spiral galaxy NGC 3198. (b): The spiral galaxy NGC 3198.

1.1.2 The motion of galaxies in a cluster

A galaxy cluster is a structure that consists of a collection of galaxies (from tens to thousands) that are bound together by gravitational attraction. In the 1930s, Zwicky found an anomaly in the velocity of the galaxies in the Coma Cluster (Abell 1656): the galaxies moved faster than what could have been expected from a cluster with a total mass equal to the visible mass. Zwicky was the first to infer the existence of unseen matter, but his considerations were taken seriously only after the study of the rotational curves in the 1970s.

1.1.3 The presence of gas in some clusters

ROSAT was a satellite X-ray telescope that worked between 1990 and 1999. Some of the pictures taken by ROSAT show a big gas cloud (in pink in Figure 3) in a cluster of galaxies that emits a small amount of X-rays; the only way to justify the presence of this confined cloud is that there has to be a strong gravitational attraction, more than the one that could derive from the visible mass of the galaxies. This is another clue of the presence of Dark Matter between the cluster's galaxies.

1.1.4 Gravitational lensing

Gravitational lensing is an effect of Einstein's theory of General Relativity. The light propagates following geodesic paths whose structure depends from the geometry of space-time dictated by the presence of a massive object. The gravitational field of a massive object will cause light rays passing close to that object to be bent and refocused somewhere else. Figure

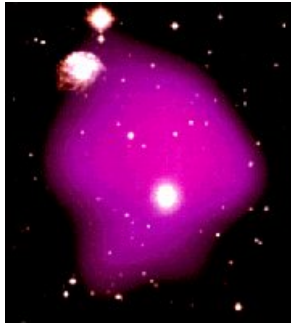


Figure 3: Picture of the gas cloud detected by ROSAT.

4) shows how this effect works. Since the gravitational lensing depends on the gravitational field of the massive object between the light source and the observer and, in turn, the field depends on the mass, this effect can be used to measure the mass of the interposed object. If the mass computed in this way is not equal to the mass of the visible matter, it means that there is a hidden mass, i.e. the Dark Matter.

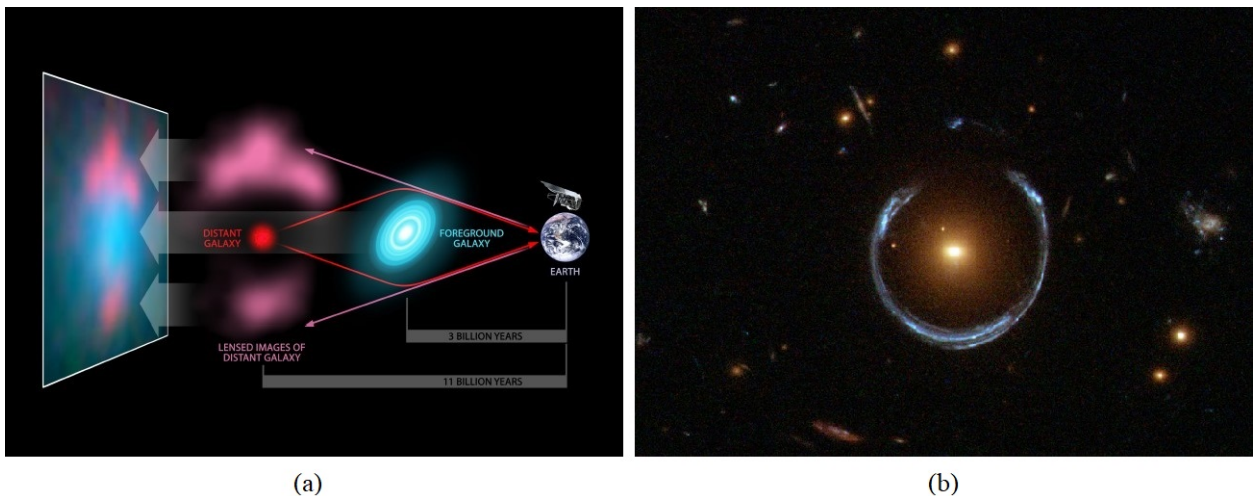


Figure 4: (a): A scheme of how gravitational lensing works. (b): An example of gravitational lensing where the light of a blue star (in the background) is bent by the presence of the yellow star in the foreground creating the blue ring.

1.1.5 Cosmological evidence

The dynamic of the Universe is described by the field equations of General Relativity solved by the Friedmann–Lemaître–Robertson–Walker (FLRW) metric. Defining the density parameter of the Universe Ω as the ratio of the observed density ρ to the critical density ρ_c ,

$\Omega = \frac{\rho}{\rho_c}$, where

$$\rho_c = \frac{3H_0^2}{8\pi G} = 5 \times 10^{-30} \text{ g/cm}^3 \quad (2)$$

with H_0 the Hubble constant, we can determine the overall geometry of the Universe. From the Friedmann equations follows that if $\Omega > 1$ the Universe has positive curvature, if $\Omega = 1$ the geometry of the universe is flat (Euclidean) and if $\Omega < 1$ it has negative curvature.

The *Cosmic Microwave Background* (CMB), Figure 5, is an electromagnetic cosmic background radiation filling all space with a black-body spectrum at a temperature of $T_{CMB} = 2.73$ K. It is a relic of an early stage of the Universe, the *epoch of recombination*, 379000 years after the Big Bang, when photons started to propagate in the Universe (before that time the Universe was not transparent to photons because light and matter were strongly coupled). The CMB is isotropic up to relative fluctuations of 10^{-5} : the experimental results for the measurement of the anisotropies show that $\Omega = 1$, thus the geometry of the Universe is flat. Nevertheless, other measurements of the density of the visible matter in the Universe from the power spectrum of the CMB show that $\Omega_{visible} = 0.003\text{-}0.01$ only, therefore the remaining part of Ω is due to the density of Dark Matter Ω_{DM} and Dark Energy.

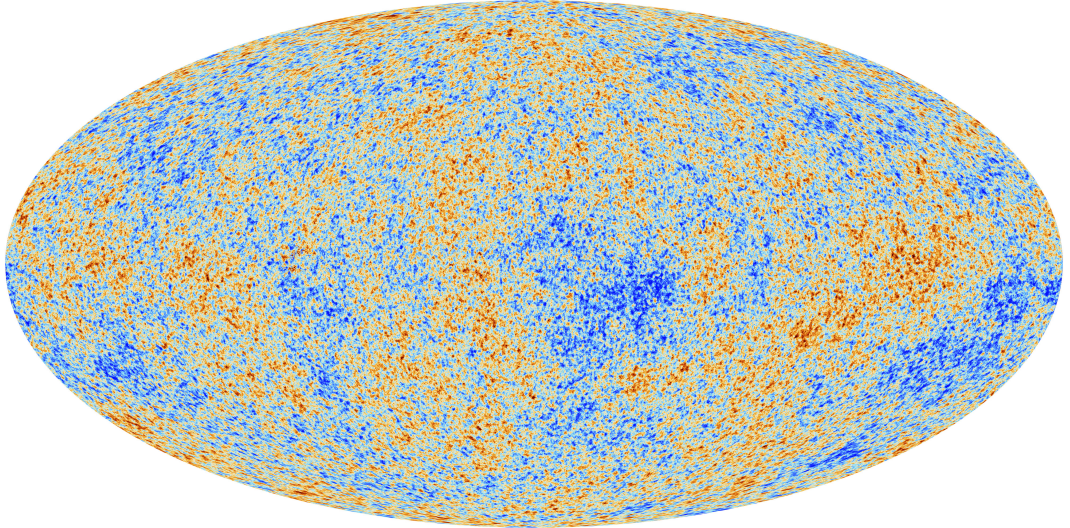


Figure 5: Anisotropies of the CMB measured by the Planck experiment (ESA) [9]

1.2 Dark Matter candidates

Thanks to the evidences of Section 1.1, physicist understood that Dark Matter constitutes the 23% of the Universe, but its nature and its characteristics are still unknown. There are some candidates:

- **Baryonic Dark Matter:** it is composed of ordinary baryonic matter like protons and neutrons. Baryonic dark matter may occur in *Massive Astrophysical Compact Halo Objects* (MACHOs), condensed objects such as black holes, neutron stars, white dwarfs or non-luminous objects like planets and brown dwarfs. Many candidates MACHOs have been observed; however their total mass and density is not sufficient to constitute the totality of Dark Matter of the Universe.
- **Non-baryonic Dark Matter:** it is not composed of ordinary baryonic matter. It is divided in relativistic hot Dark Matter and in non-relativistic cold Dark Matter. The hot DM may be composed of low mass and fast-moving particles which do not collect in galaxies, thus they may make up the Dark Matter present between galaxies in a cluster. A hot DM candidate is the neutrino; however the contribution of all neutrinos to the density parameter Ω is only $\Omega_\nu \sim 0.015$. For this reason, it is believed that the dominant role is played by the cold Dark Matter: it has a higher mass than the hot DM and it can collect in galaxies and clusters. The main cold DM candidates are WIMPs (*Weakly Interacting Massive Particles*) that will be discussed in the next Section.

1.2.1 WIMPs

WIMPs are neutral stable (or at least extremely long lived because they influenced the formation of the structure of the Universe) particles with a mass between 10 GeV to 1 TeV that interact very weakly with the other particles. Currently there are some theoretical frameworks incorporating WIMP-like particles:

- WIMPs are hypothesized in **Supersymmetry** (SUSY) theory, the supersymmetric extension of the Standard Model. Supersymmetry proposes a relationship between the two basic classes of elementary particles: bosons, which have an integer-valued spin, and fermions, which have a half-integer spin. Each particle from one group would have an associated particle in the other, which is known as its superpartner, the spin of which differs by a half-integer. The main WIMPs candidate is the neutralino χ^0 , the lightest neutral stable supersymmetric particle.
- There are some theories of **extra dimensions** that, trying to include all four fundamental interactions, propose additional space or time dimensions beyond the $(3 + 1)$ typical of observed spacetime. Some of these theories predict particles which can be viewed as DM candidates.

WIMPs are the most compelling explanation of the nature of Dark Matter for various reasons. If we assume that Dark Matter was created thermally shortly after the Big Bang, at the early hot stages of the Universe SM particles (X) and DM particles (χ) were in thermal equilibrium, therefore the creation of DM from SM particles and viceversa happened at equal rates:

$$\chi\chi \longleftrightarrow XX. \quad (3)$$

As the Universe cooled down, since the DM particles' mass is far larger than that of SM particles, the thermal energy available in the Universe became insufficient to allow the reaction to the left ($\chi\chi \longleftrightarrow XX$). Therefore, the only reaction that could continue was the one to the right, from DM to SM particles: $\chi\chi \longrightarrow XX$. However the annihilation of DM particles and the continuous expansion of the Universe, after a certain time caused a density drop of DM and therefore an almost complete interruption of the reaction that, in turn, made the DM density basically constant in time. This process follows the Boltzmann equation: from that it is possible to compute today's relic density of the DM particle χ . If χ is a WIMP, for example with a mass of $m \sim 100$ GeV and assuming an interaction cross section of the order of the weak scale, its density is $\Omega_\chi = 0.1 - 0.3$ (it depends on the model used for the calculations) in good agreement with density measured by the PLANCK experiment [9] of $\Omega_\chi = 0.1186 \pm 0.0020$.

1.3 Detection of Dark Matter

There are three possible detection strategies to look for Dark Matter: each one of them uses the interaction diagram in Figure 6 from different directions.

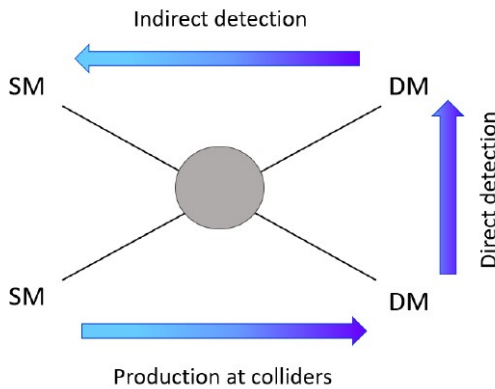


Figure 6: A scheme of how the three different detection strategies work.

Indirect detection methods consist in looking for the SM products of DM annihilation (Section 1.3.1). Direct searches try to detect DM particles coming from the outer space: when a WIMP scatters off a nucleus, direct methods try to measure the recoil energy of the target nucleus (Section 1.3.2). Searches at colliders try to detect DM particles produced by SM particles, in particular in pp collisions (Section 1.3.3).

1.3.1 Indirect methods

Indirect detection methods are based on the idea that WIMPs can be gravitationally attracted by massive objects like stars or galaxies: even if they interact weakly and have a

very small cross section, they are slow (~ 270 km/s) and massive and these characteristics increase their probability to be trapped in the gravitational field of a very massive object. In this way in the field region of space the WIMPs density raises and consequently the probability of annihilation increases. The flux of SM decay products is proportional to the annihilation rate of DM particles, which is in turn proportional to the square of the DM density. The most common decay products are photons, cosmic rays, high-energy neutrinos, positrons or anti-protons: they are all SM particles so they can be detected with conventional techniques. The main problem with indirect approach, however, is that the same particles are also produced in other "ordinary" astrophysical phenomena: these constitute the main background sources. Therefore, the indirect strategy focuses on finding an excess of the annihilation products with respect to theoretical expectations and on understanding if the source of this peak could be a region with a large density of DM.

1.3.2 Direct methods

Direct searches try to detect DM particles coming from the outer space: when a WIMP scatters off a nucleus, direct methods try to measure the recoil energy of the target nucleus. The WIMP interaction with the detector's nuclei can have different features: it could be either elastic or inelastic, either spin-dependent or spin-independent. If the scattering is elastic, the WIMP interacts with the whole nucleus causing it to recoil: measuring the recoil energy of the nucleus it would be possible to calculate the energy of the WIMP. If the scattering is inelastic, there are two possible interactions:

- if WIMPs interact with the electrons around the nucleus, they would ionize the atom. Therefore the signature of a WIMP passing through the detector would be a path of ionized atoms;
- if they interact directly with the nucleus, they could leave it in an excited state from which the nucleus would fall back into the ground state emitting a detectable photon.

Moreover, if the interaction is spin-independent, the WIMP would interact at the same way with the two nucleons in the nucleus, protons and neutrons. If it is spin-dependent, WIMPs would interact differently with protons and neutrons and thus the characteristics of the interaction with the whole nucleus would depend on the net nuclear spin. Nevertheless, there are some experimental problems that make very complex to detect directly WIMPs:

- The recoil kinetic energy of the nucleus caused by a WIMP of a mass between 10 GeV and 1 TeV would be only tens of keV and thus very difficult to be distinguished from the background. The main background sources are cosmic rays and natural radioactivity of the environment and of the detector. To reduce the cosmic rays background, the experiments are located underground, for example the DAMA/LIBRA experiment is located underground at the Laboratori Nazionali del Gran Sasso, under the mountain.

To reduce the radioactivity of the environment, the detector has a shielding shell, while to reduce the detector's radioactivity it is made of extremely radio-pure materials.

- The WIMPs's cross section is not exactly known but it is very small: it is somewhere between $10^{-48} - 10^{-41}\text{cm}^2$; due to the smallness of the cross section, the rate of expected events in a day is very low, between $10^{-5} - 1 \frac{\text{events}}{\text{kg} \cdot \text{day}}$. To face this problem the detectors need to be very big, but the bigger the detector is, the harder it becomes to build it with radio-pure materials.

Fortunately there is another method that make possible to overcome these problems: the Earth moves through the DM halo that surrounds our galaxy, yielding a "WIMPs wind". This fact should lead to a small annual modulation in the detected WIMPs rate, while the background should not have a specific annual modulation. The DAMA experiment [10] uses 9 NaI(Ti doped) crystals, each one with a mass of 9.7 kg; it observed an annual modulation (Figure 7) of the event rate consistent with the detection of a WIMP with a mass of ~ 40 GeV and a scattering cross section of $\sim 10^{-41} \text{ cm}^2$.

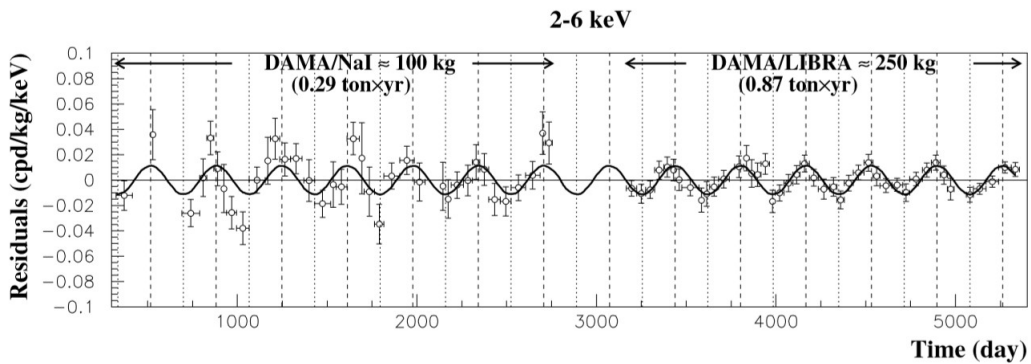


Figure 7: The annual modulation detected by the DAMA/LIBRA experiment in the (2 – 6) keV energy interval as a function of the time. The superimposed curve is $A \cos \omega(t - t_0)$ with period $T = 2\pi\omega = 1\text{yr}$, phase $t_0 = 152.5$ day and a modulation amplitude, A , equal to the central value obtained by best fit over the whole data.

1.3.3 Search at colliders

From Equation 3 derives that like SM particles can be produced from DM, Dark Matter particles can be produced in ordinary collisions, such as the pp collisions at hadron colliders. In any case, the produced WIMP would escape the detector without leaving a trace. However, the presence of a WIMP could be detected because it would leave a particular signature inside the detector. The total momentum in the transverse plane, that is the vectorial sum of the transverse momenta p_T of the particles produced in a pp collision, is expected to amount to

zero; if the detector finds a missing transverse momentum E_T^{miss} this means that it was not able to see the trace of a particle. For this reason, a Dark Matter particle would manifest itself as a missing transverse momentum but only if it is produced in pair with a detectable SM object: the two decay products would recoil against each other, leaving in the detector an event with a large missing transverse momentum and a SM particle. The presence of a SM particle is necessary to tag the event: as Figure 1.8 shows, if a SM particle is not present, the event would not be even observed. The SM object, which could be a jet, a photon, a vector boson (W^\pm or Z) or a Higgs boson, gives the name to these signatures, called mono-X signatures, where X is the SM object used to tag the event. Mono-X signatures at colliders are interpreted in the light of Simplified DM models; these searches look for an excess of events with the mono-X signature with respect to SM processes expecting the same signature.

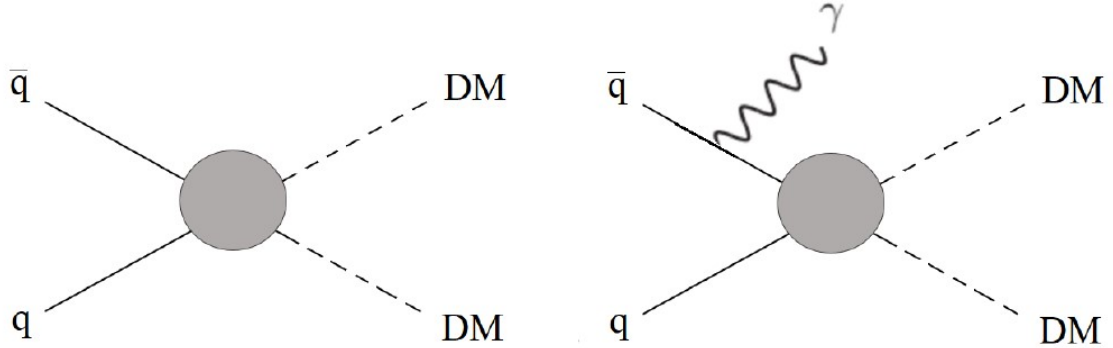


Figure 8: The event on the left cannot be detected by ATLAS: an E_T^{miss} value cannot be measured if there is no other detectable SM particle produced in the event. On the contrary, the presence of the photon (playing the role of the detectable SM physics object X), makes it possible to measure a E_T^{miss} value.

2 LHC and ATLAS

This section describes the main characteristics of the Large Hadron Collider (better known simply as LHC) and in particular of the ATLAS experiment and its detectors.

2.1 The Large Hadron Collider

The Large Hadron Collider (LHC) [1] at CERN near Geneva, Switzerland, is the world's most powerful tool for Particle Physics research. It is a two-ring-superconducting-hadron accelerator and collider installed in the existing 27 km tunnel that was constructed for the CERN LEP (Large Electron-Positron collider) machine. It was completed in 2008 and in 2009 started Run 1, the first operational run of LHC at a center of mass energy of 7 and 8 TeV, which came to an end in 2013, after the observation of the Higgs boson in 2012 [6] [7]. The data used for the work presented in this thesis were collected by the ATLAS detector in Run 2, between 2015 and 2018, when the LHC operated at a centre-of-mass energy of $\sqrt{s} = 13$ TeV in proton-proton collisions with an instantaneous luminosity up to $2 \cdot 10^{34}$ cm $^{-2}$ s $^{-1}$. The total integrated luminosity of Run 2 amounts to more than $L = 140$ fb $^{-1}$. The LHC can also collide heavy ions as Pb with an energy of 2.8 TeV per nucleon and a peak luminosity of 10^{27} cm $^{-2}$ s $^{-1}$.

2.1.1 CERN accelerator complex and LHC structure

The protons travel inside two separate beamlines in opposite directions along the LHC ring; they are bent along the circular orbit thanks to a strong magnetic field of 8.33 T created by superconducting dipole magnets while superconducting quadrupole magnets keep the beams focused. The superconducting magnets are mandatory to achieve high currents but they operate at very low temperatures, around 1.9 K. It is possible to obtain this extreme temperature by a sophisticated cryogenics system that uses liquid helium to cool the magnets.

Before being injected into the LHC ring with the desired energy (450 GeV), protons and ions are accelerated in four steps by a set of linear and circular accelerators:

- firstly, protons are extracted from hydrogen gas and speeded up to 50 MeV by LINAC 2 (LINear ACcelerator);
- then they are accelerated up to 1.4 GeV by the Proton Synchrotron Booster (PSB);
- afterwards, the Proton Synchrotron (PS) accelerates them up to 25 GeV;
- eventually, in the Super Proton Synchrotron (SPS) protons reach 450 GeV and are injected into the LHC.

Along the LHC tunnel there are four pp collision points corresponding to the position of the four main experiments: LHCb, ALICE, ATLAS and CMS.

CERN's Accelerator Complex

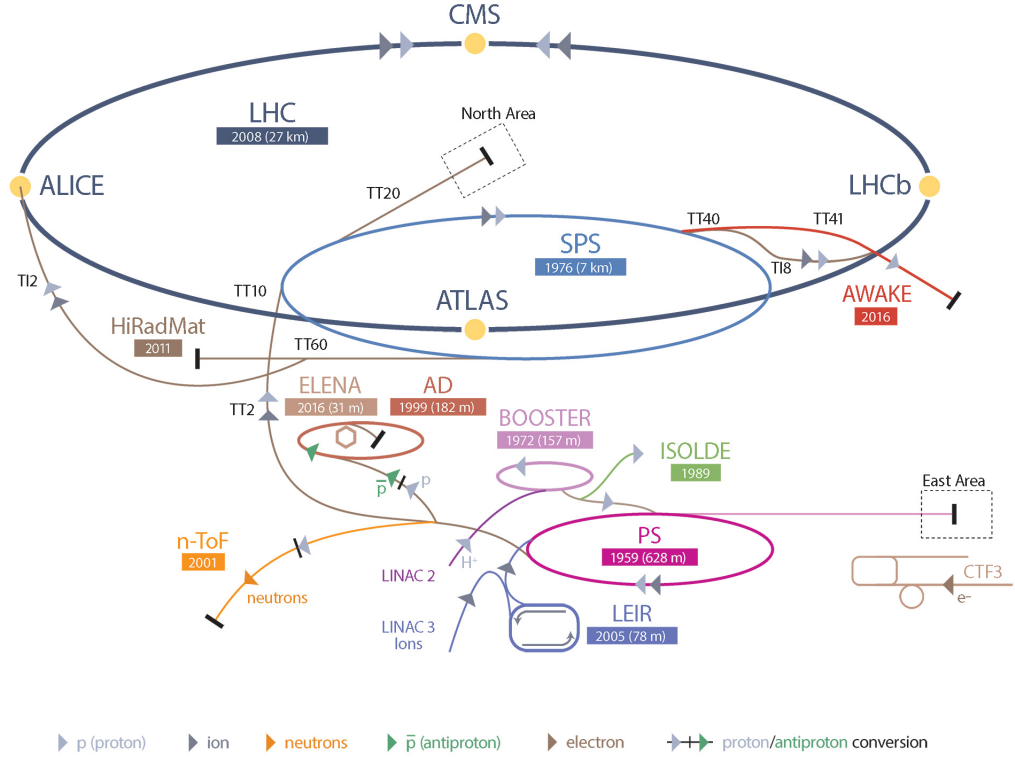


Figure 9: CERN's accelerator complex and LHC structure.

- LHCb (Large Hadron Collider beauty experiment) [12] studies B-hadrons' decays looking for CP violation sources beyond the Standard Model.
- ALICE (A Large Ion Collider Experiment) [13] observes heavy-ion collisions and studies strong interactions in quark-gluon plasma.
- ATLAS (A Toroidal LHC ApparatuS) [3] and CMS (Compact Muon Solenoid) [11] are general purpose detectors, designed to cover a broad range of physics measurements in proton-proton and heavy-ion collisions to investigate the Standard Model of particle physics (SM) and search for new physics not described by the SM.

In addition, there are three smaller experiments dedicated to specialised researches: the MoEDAL (Monopole and Exotics Detector at the LHC) [14], the TOTEM (TOTal cross section, Elastic scattering and diffraction dissociation Measurement at the LHC) [15] and the LHCf (Large Hadron Collider forward) [16].

The entire CERN acceleration complex and LHC structure is showed in Figure 9.

2.1.2 Proton-proton interactions and luminosity

Proton-proton collisions at high energies in the four points of LHC are studied to validate the Standard Model's predictions and to explore physics beyond it (BSM). Two different classes of events can occur:

- **Soft collisions:** they are large distance collisions between protons with low momentum transfer. The protons behave as elementary particles and, for that reason, their internal structure does not come to light. In this case the momentum transferred during the interaction is small and particles scatter at small angles. The particles produced by such interactions have small transverse momentum relative to the beam line.
- **Hard collisions:** these events are short distance collisions, so they can be viewed as interactions between partons (quarks and gluons), the inner constituents of protons. They are characterized by large momentum transfer; in this case it is possible to produce high mass particles at large angles with respect to the beam line.

The latter are the most interesting from an experimental point of view but they are also the rarest. This fact complicates the study of the collisions: the detectors at LHC have to distinguish interesting hard processes from the more common and simultaneous soft collisions which normally disturb the measurements of the hard collisions.

The exploration of rare events requires both high beam energies and high beam intensities, the former in order to produce massive particles and to profit from the typical increase of the cross section with the energy (Figure 10), the latter in order to have a sufficiently large number of events to perform a significant measurement of search.

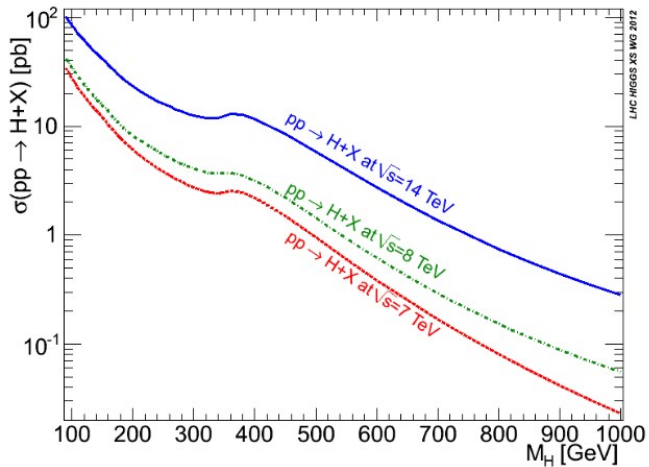


Figure 10: Standard Model Higgs boson production total cross sections at center of mass energy $\sqrt{s} = 7, 8$ and 14 TeV: the cross section increases with the energy.

The number of events for a given process per second generated in the LHC collisions is given by:

$$\frac{dN_{event}}{dt} = \mathcal{L}\sigma_{event}, \quad (4)$$

where σ_{event} is the cross section of a given process and \mathcal{L} is the machine *instantaneous luminosity*. In particular, the integral with respect to time of the instantaneous luminosity, i.e. the *integrated luminosity* L , is an important indicator of the performance of an accelerator: it is proportional to the number of collisions that occur in a given amount of time. Since the cross section is an area, the instantaneous luminosity has the dimension of $[\text{length}]^{-2} \times [\text{time}]^{-1}$ and then the integrated luminosity is usually expressed in terms of fractions of inverse barns, where $1 \text{ barn} = 10^{24} \text{ cm}^2$. Assuming the hypothesis of ideal collisions of bunches and Gaussian particles densities, the instantaneous luminosity depends only on the beam characteristics and can be written as:

$$\mathcal{L} = \frac{n_{beam} N_{bunch}^2 f_{rev} \gamma}{4\pi \epsilon_n \beta^*}, \quad (5)$$

where n_{beam} is the number of bunches per beam, N_{bunch} is the number of protons per bunch, f_{rev} is the revolution frequency around the LHC ring, γ is the relativistic factor, ϵ_n is related to the protons' momentum and position distribution and β^* is the transverse size of the particle beam at the collision point.

Machine Parameter	Designed	2015	2016
Center of mass energy	7.0	6.5	6.5
$N_{bunch} [10^{11} \text{ p}]$	1.15	1.0	1.1
n_{beam}	2808	2244	2200
$f_{rev} [\text{Hz}]$	11245	11245	11245
$\epsilon_n [\mu\text{m}]$	3.75	3.5	2.2
$\beta^* [\text{m}]$	0.55	0.8	0.4
Max. peak luminosity $[10^{34} \text{ cm}^{-2} \text{s}^{-1}]$	1.0	0.47	1.45

Table 1: Typical parameters values at the LHC for the years 2015 and 2016, shown together with the designed parameters [17].

In Figure 11 and 12 the integrated and instantaneous luminosity trend as a function of time during 2015-2018 data collection in Run 2 are reported:

- the instantaneous luminosity has a peak value of $5 \times 10^{33} \text{ cm}^{-2} \text{s}^{-1}$ in 2015, $13.8 \times 10^{33} \text{ cm}^{-2} \text{s}^{-1}$ in 2016 and $21 \times 10^{33} \text{ cm}^{-2} \text{s}^{-1}$ in 2017 and 2018.
- the recorded integrated luminosity was 3.9 fb^{-1} in 2015, 35.6 fb^{-1} in 2016, 46.9 fb^{-1} in 2017 and 60.6 fb^{-1} in 2018, so that the cumulative luminosity is 147 fb^{-1} as shown in Figure 13.

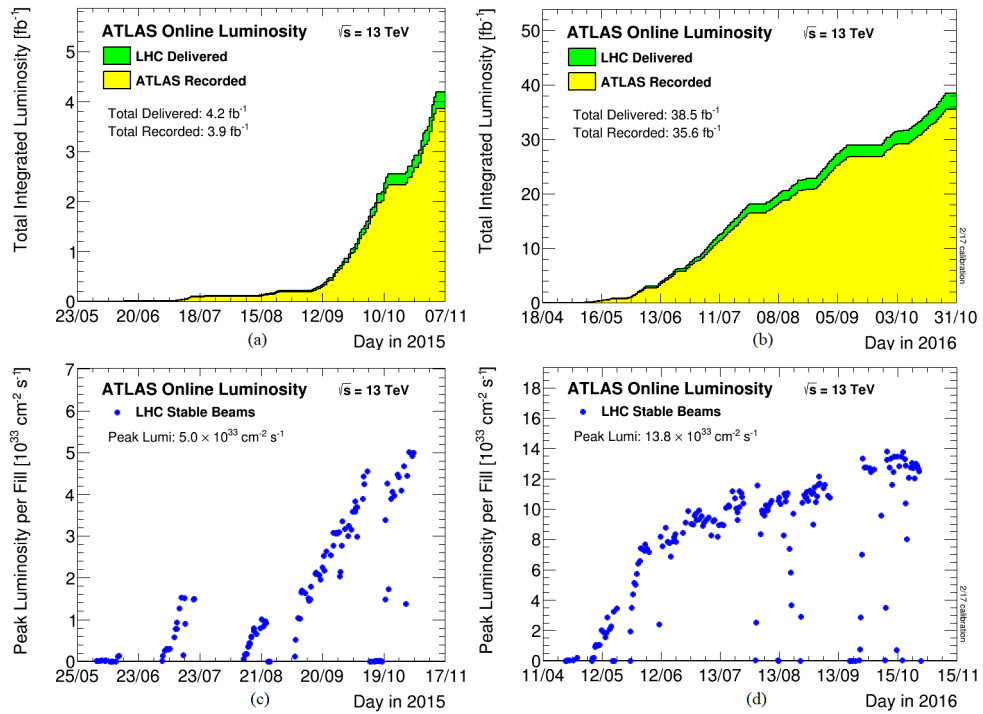


Figure 11: Top: integrated luminosity delivered by the LHC (green) and recorded by ATLAS (yellow) in pp collisions at 13 TeV center-of-mass-energy in 2015 (a) and 2016 (b). Bottom: peak instantaneous luminosity recorded in the same conditions in 2015 (c) and 2016 (d) [2].

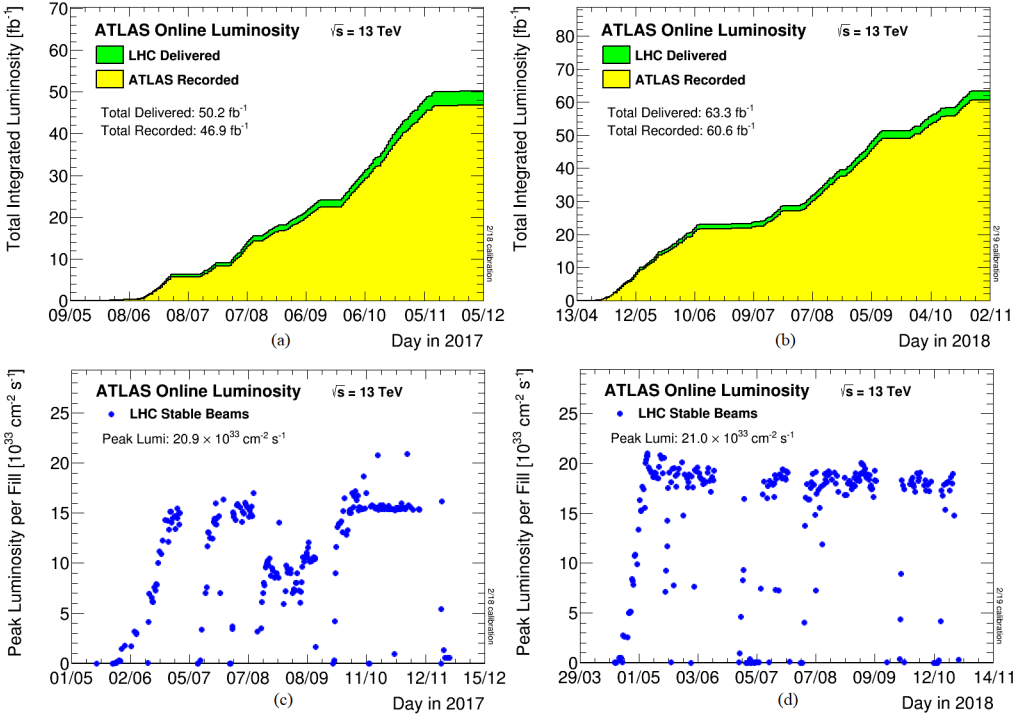


Figure 12: Top: integrated luminosity delivered by the LHC (green) and recorded by ATLAS (yellow) in pp collisions at 13 TeV center-of-mass-energy in 2017 (a) and 2018 (b). Bottom: peak instantaneous luminosity recorded in the same conditions in 2017 (c) and 2018 (d) [2].

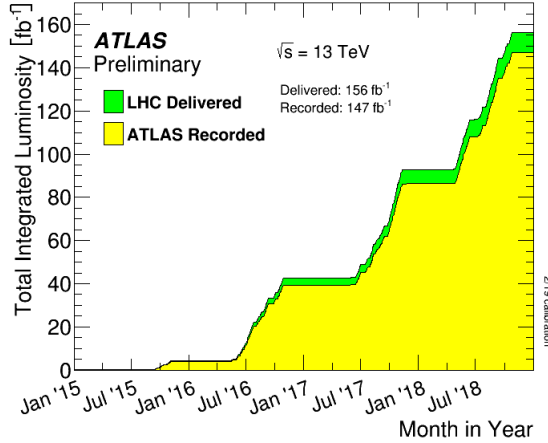


Figure 13: Total integrated luminosity versus time delivered to ATLAS (green) and recorded by ATLAS (yellow) during stable beams for pp collisions at 13 TeV centre-of-mass energy in LHC Run 2 [2].

2.2 The ATLAS experiment

The ATLAS (A Toroidal LHC ApparatuS) experiment [3], together with CMS, is one of the two general purpose detectors of LHC and it is also the largest one: it weights nearly 7000 tons, it has a cylindrical 44 m long shape with a diameter of 25 m. The detector, as shown in Figure 23, is composed by various subdetectors that can be divided in three main sections (which will be described in Sections 2.2.1-2.2.3):

- **The Inner Detector** (ID) tracks charged particles and reconstructs primary and secondary vertices;
- **The Calorimeters** measure the energy and direction of electrons, photons and jets of hadrons;
- **The Muon Spectrometer** (MS) measures direction and momentum of muons.

Before describing each section, it is useful to describe a common coordinate system (x,y,z) in which the origin is defined as the nominal interaction point. The z -axis is set along the beam axis while the $x-y$ plane lies orthogonal to it, defining the transverse plane, with the x -axis pointing towards the center of the ring and the y -axis pointing upwards. To define the direction of particles emerging from the interaction point, two quantities are used η and ϕ :

- The azimuthal angle ϕ is measured in the transverse plane around the beam direction;
- η is a dimensionless quantity called *pseudorapidity*, defined as a function of the polar angle θ with respect to the z -axis:

$$\eta = -\ln \tan\left(\frac{\theta}{2}\right). \quad (6)$$

The variable η can be used in place of θ since its definition implies a one-to-one correspondence between the two quantities, ranging respectively from 0 to π and from $+\infty$ to $-\infty$.

Most of the quantities measured at ATLAS are referred to the transverse plane. Once pseudorapidity has been defined, it is possible to express the four momentum components $p = (E, p_x, p_y, p_z)$ as

$$p = (p_T \cosh \eta, p_T \cos \phi, p_T \sin \phi, p_T \sinh \eta), \quad (7)$$

where $p_T = \sqrt{p_x^2 + p_y^2}$ is the module of the momentum component in the transverse plane. Furthermore, pseudorapidity is used to define the distance:

$$\Delta R = \sqrt{\Delta\eta^2 + \Delta\phi^2}, \quad (8)$$

which is Lorentz invariant under a boost along the beam direction.

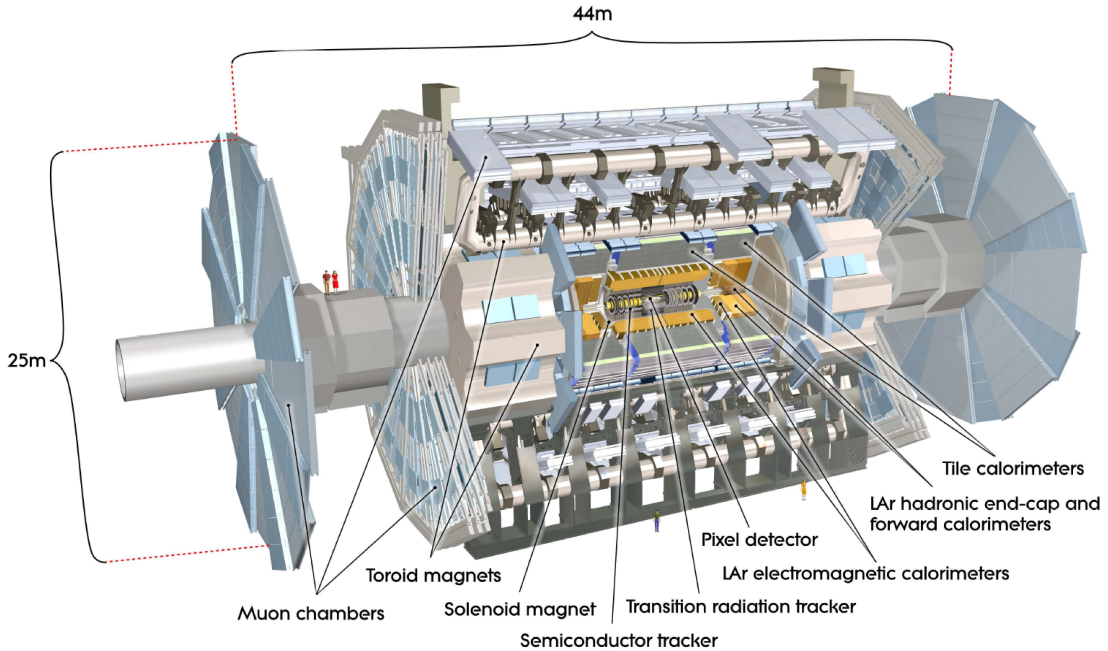


Figure 14: The ATLAS detectors and subdetectors.

2.2.1 The Inner Detector

The Inner Detector (ID) is the innermost detector of ATLAS thus the closest one to the interaction point. The ID has a cylindrical 6.2 m long shape with a diameter of 2.1 m. The ID measures charged particle tracks with their direction, impact parameters and momentum. The latter is realised through the measurement of the curvature of charged particle tracks in a 2 T magnetic field produced by a **solenoid magnet**. In the barrel region layers are arranged in concentric cylinders centred around the beam pipe; in the end-cap region layers consist of disks arranged perpendicularly to the z-axis. Consequently, the ID covers a pseudorapidity region of $|\eta| < 2.5$. Furthermore, the ID must be resistant to the radiation caused by the huge amount of highly energetic particles from primary and secondary collisions. The total amount of material of the ID has to be small to minimize the probability for an electron or a photon to initiate an electromagnetic shower before reaching the calorimeter. The ID has three components:

- **Pixel Detector:** the Pixel Detector is the closest to the beam pipe and it is the detector with the best spatial resolution. In the barrel region, silicon pixels are arranged in three cylindrical layers at a radius of 50.5 mm, 88.5 mm and 122.5 mm from the beam line. An additional layer at a distance of 31 mm is called Insertable B-Layer (IBL); it was inserted between Run 1 and Run 2 to improve the tracking resolution. The Pixel Detector contains 1744 modules; each module is 62.4 mm long and 21.4 mm wide and consists of 46080 pixels for a total of more than 80 million pixels. Each pixel

has a size of $(R - \phi) \times z$ of $50 \times 400 \mu\text{m}^2$ and the detector resolution is $10 \mu\text{m}$ on $R - \phi$ and $115 \mu\text{m}$ on z . The typical number of points generally provided by the Pixel Detector is four.

- **Semi-Conductor Tracker (SCT):** the SCT is made of silicon strips and completes the high-resolution tracking. It is placed at a radius between 299 mm and 514 mm and it is composed of 4 cylinders made of two layers of sensors glued with a 40 mrad stereo-angle, leading to a total of eight layers (thus eight space points for each track) in the barrel region whereas there are nine layers in the end-caps area. The SCT achieves a resolution of $17 \mu\text{m}$ in the $R - \phi$ plane and $580 \mu\text{m}$ along z -axis.
- **Transition Radiation Tracker (TRT):** the TRT is the outermost layer of the Inner Detector and it is placed between 554 mm and 1082 mm. TRT has poorer single point spatial resolution than the other detectors ($130 \mu\text{m}$ in $R - \phi$ and $|\eta| < 2$) but it can provide a larger number of hits. The TRT was designed to provide informations about both tracking and particle identification. It is composed of straw tubes with a diameter of 4 mm and 144 cm long positioned parallel to the beam line in the barrel region and radially in the end-cap regions. They are filled with gas mixture (Xe and Ar) which becomes ionized when a charged particle passes through the tube. The straw tubes are interleaved with polymer fibres. A highly relativistic particles (typically electrons) can emit transition radiation as they traverse the material boundary. The transition radiation can be measured in the tubes providing a powerful discriminating handle between hadrons and electrons.

Figure 15 shows the structure of the ID and of its components.

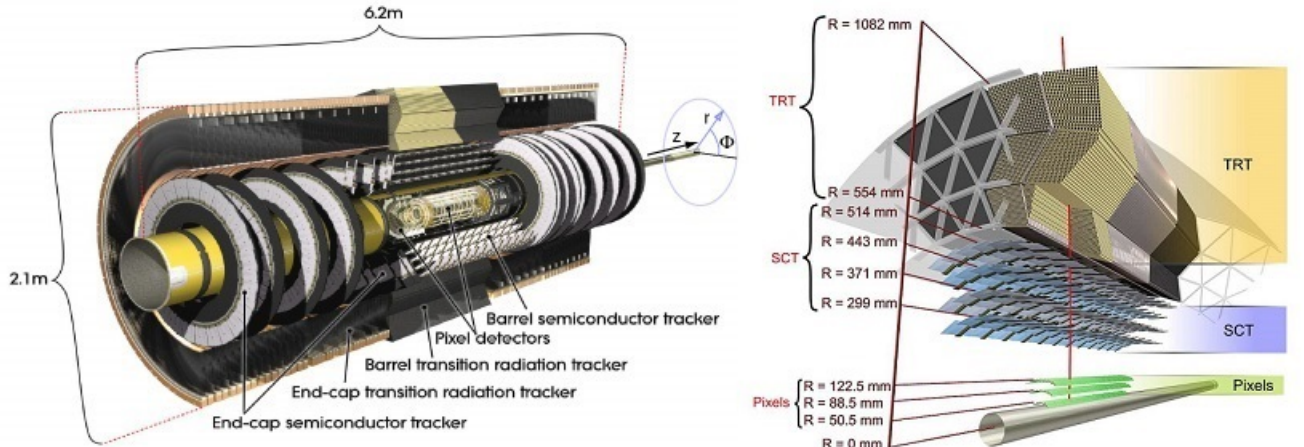


Figure 15: The structure of the Inner Detector.

2.2.2 The Calorimeters

As the ID measures the presence of charged particles, neutral ones are invisible to the inner part of the ATLAS detector. For this reason, there is the calorimetric system: its purpose is to measure the energy and the direction of charged and neutral particles (except for the highly penetrating muons) [4]. It is composed of three different parts, as illustrated in Figure 16: the **Electromagnetic Calorimeter (EM)**, the **Hadronic Calorimeter (HCal)** and the **Forward Calorimeter (FCal)**. The first measures the energy of electrons and photons, the second is optimised for the reconstruction of jets of hadrons and the last one provides energy measurements for both electromagnetic and hadronic showers in the forward region. They are made of alternated active and passive (absorbing) materials and their working principle is the same: when a particle interacts with the calorimeter material it creates a shower of secondary particles; as their energy is progressively absorbed, it is measured by the calorimeter's active material. The calorimeter system used in ATLAS was designed to cover different pseudorapidity ranges and longitudinal depths.

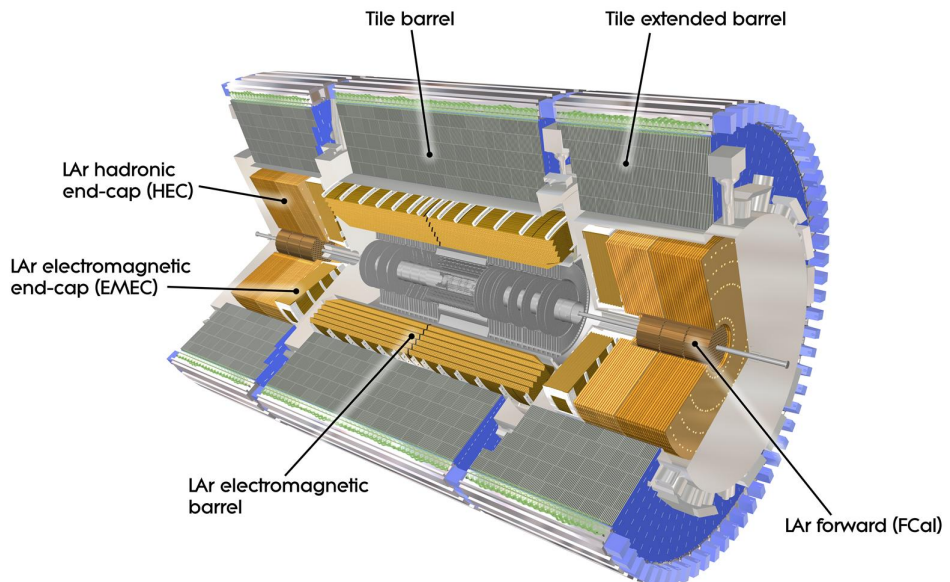


Figure 16: The ATLAS calorimetric system.

- **Electromagnetic Calorimeter (EM):** the EM is the first calorimeter system encountered by particles. It is a cylinder 6.65 m long with an outer radius of 2.25 m. It detects electromagnetic showers produced by electrons and photons through the use of lead as passive material and of Liquid Argon (LAr) as active material. LAr works at a temperature of - 183 °C. The EM is composed of a barrel region located in the central

area and of a end-cap region (EMEC). The former covers a pseudorapidity range of $|\eta| < 1.4$ whereas the latter lies in the range $1.4 < |\eta| < 3.2$. However, in the region where the barrel meets the end-cap region in the range $1.37 < |\eta| < 1.52$, there is a transition region with poorer performance. The EM is composed of four parts in the radial direction (from the innermost to the outermost): the PreSampler (PS, a thin layer of Liquid Argon placed before the calorimeter which covers the $|\eta| < 1.8$ region), Layer 1 (L1, it has the finest granularity in η), Layer 2 (L2, it absorbs most of the energy of the electrons and photons) and Layer 3 (L3, used to estimate the amount of energy leaning outside the calorimeter in the longitudinal direction). A summary of thickness and granularity of the calorimeter is illustrated in Table 2 and in Figure 17.

Layer	Thickness	Granularity ($\Delta\eta \times \Delta\phi$)
PS	from 1.7 to 2.2 radiation lengths	0.025×0.1
L1	from 3 to 6 radiation lengths	0.03×0.1
L2	up to 17 radiation lengths	0.025×0.025
L3	2 radiation lengths	0.050×0.025

Table 2: Thickness and granularity of EM calorimeter layers.

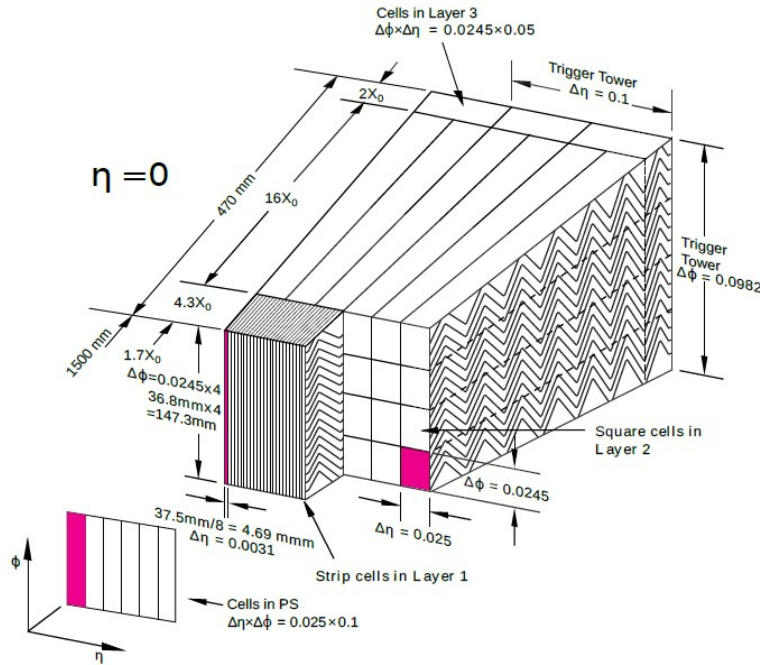


Figure 17: Electromagnetic Calorimeter structure and barrel granularity.

- **Hadronic Calorimeter (HCal)**: the EM is surrounded by the HCal, a 6.10 m long cylinder with an outer radius of 4.25 m. Its purpose is to contain particle showers generated by jets of hadrons in order to measure their energy and direction. It is divided in two sections: the Tile Calorimeter (TCal) is a steel-scintillator sampling calorimeter that covers a region of $|\eta| < 1.7$, the LAr Hadronic End-Cap calorimeter (HEC) is outside the EMEC and it covers a pseudorapidity range $1.5 < |\eta| < 3.2$.
- **Forward Calorimeter (FCal)** the Forward Calorimeter covers the high-pseudorapidity range $3.1 < |\eta| < 4.9$. It is divided in three regions in the z-direction that uses argon as active material: the first (made of copper) is optimised for electromagnetic showers containment, the other two (made of tungsten) are used for hadronic jets measurements.

2.2.3 The Muon Spectrometer

The calorimeters are surrounded by the Muon Spectrometer (MS), which is meant to detect muons which are not stopped in the detectors described previously. It covers the $|\eta| < 2.7$ range. Through the use of a toroidal magnetic field of 0.3 T, the MS deflects charged particles and measures the muon's momentum with high precision. Since calorimeters provide excellent containment for electromagnetic and hadronic showers, only muons (and neutrinos which are not detected) can reach MS. Tracking is carried out by Monitored Drift Tubes (MDTs) in the barrel area and Cathode Strip Chambers (CSCs) in the end-cap region. The trigger system is composed by two parts: the Resistive Plate Chambers (RPCs) in the barrel and the Thin Gap Chamber (TGC) in the end-cap region. The different sections of the Muon Spectrometer are shown in Figure 18.

2.2.4 The trigger system

Since the LHC produces a huge amount of collisions (at a rate of 40 MHz), the trigger system [5] aim is to select only the physical interesting events (at a rate of 1 kHz). Consequently, the trigger must establish whether the measured collision products have the required characteristics in a extremely short time. It is divided in two levels where each trigger level optimises the selections of the previous level:

- **Level 1 trigger (L1)** is the first level trigger and it is hardware based. It has a decision time of $2.5 \mu\text{s}$ and it reduces the event rate from 40 MHz to 100 kHz. It searches for photons, electrons, muons, jets, taus and missing transverse energy E_T^{miss} defining Regions of Interest (RoIs).
- **High Level Trigger (HLT)**: since 2015, the Level 2 trigger (L2) and the Event Filter (EF) have been united under the High Level Trigger. L2 is the second level trigger and it refines the analysis of L1 using more detailed informations; the EF reduces the event rate from 100 kHz to 1 kHz.

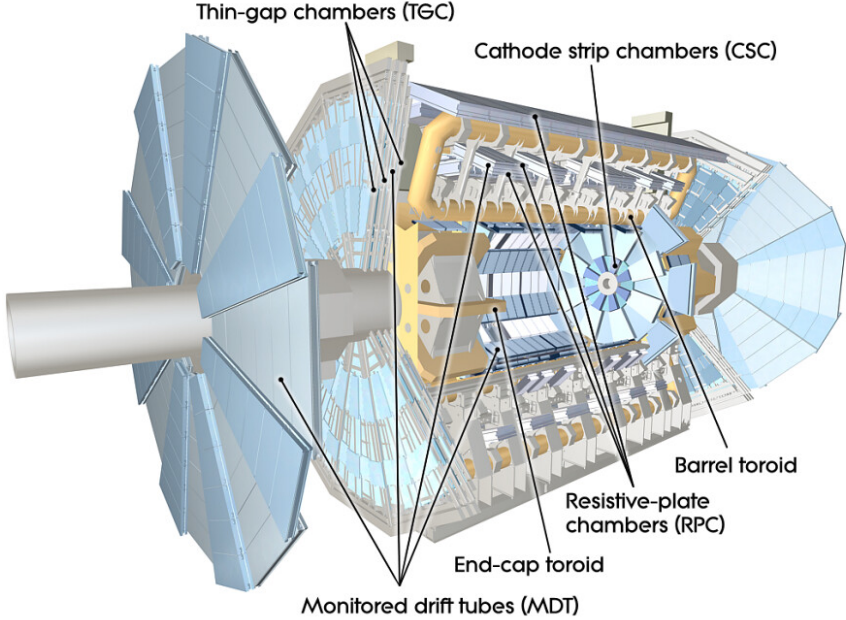


Figure 18: The structure of the Muon Spectrometer.

Typical trigger rates for L1 and HLT are shown in Figure 19.

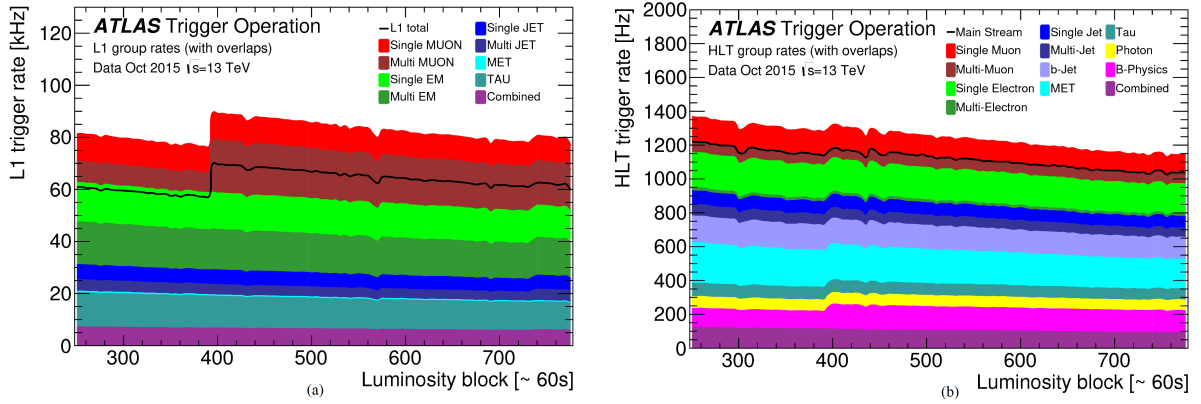


Figure 19: (a) L1 and (b) HLT trigger rates grouped by trigger as a function of the number of luminosity blocks which correspond to on average 60 s per luminosity block. Black lines show the (a) L1 total rate and (b) HLT main physics stream rate.

3 Electrons and photons reconstruction with the ATLAS detector

The reconstruction, the identification and the isolation of electrons and photons with the ATLAS detector [19] [20] is based on the reconstruction of tracks in the Inner Detector and of clusters of energy deposits in the Electromagnetic Calorimeter. The calorimetric information alone is not sufficient to discriminate between electrons and photons because their electromagnetic showers are essentially indistinguishable: therefore if their energy deposit can (or cannot) be linked to a track in the ID it is possible to discriminate among the three possible cases:

- *converted photon* candidate when a photon decays into a e^-e^+ pair before reaching the EM calorimeter, e.g. in the Inner Detector if the cluster of energy in the EM calorimeter matches a secondary vertex reconstructed from one or two tracks;
- *unconverted photon* candidate if the cluster has no track or a conversion vertex in the ID pointing to it;
- electron candidate if a track matching the cluster barycenter is found (but no conversion vertex).

3.1 Energy clusters and track reconstruction

3.1.1 Energy clusters in the Electromagnetic Calorimeter

The reconstruction of electrons and photons starts with searching clusters of energy in the EM calorimeter cells: the creation of a preliminary set of these clusters is performed by a *sliding-window algorithm* [22] in three steps:

- **Tower building:** the EM calorimeter is divided in the $\eta\text{-}\phi$ plane in $N_\eta \times N_\phi = 200 \times 256$ towers each one of size $\Delta\eta \times \Delta\phi = 0.025 \times 0.025$. Each tower contains several cells of the three layers of the EM calorimeter and the tower energy is computed as the sum of the energies of all cells contained in the tower.
- **Seed cluster finding:** a window of size $N_\eta^{window} \times N_\phi^{window} = 3 \times 5$ towers is moved across the calorimeter $\eta\text{-}\phi$ plane in steps of $\Delta\eta = 0.025$ and $\Delta\phi = 0.025$: if the energy of the window, i.e. the sum of the transverse energies of the 15 towers in the window exceeds a threshold energy of 2.5 GeV, these towers are selected as seed clusters.
- **Cluster filling:** a cluster is built around the seed position in every layer, in the barrel region as a 3×7 cells cluster and a 5×5 rectangle in the end-caps region. At first a cluster in Layer 2 is built around the seed cluster position defined as the energy weighted $\eta\text{-}\phi$ barycenter of the pre-cluster cells. The seed position for the corresponding

clusters in L1 and L3 is computed as the energy weighted $\eta\text{-}\phi$ barycenter of the cluster cells.

The cluster reconstruction efficiency with the sliding-window algorithm varies from 95% at $E_T = 7$ GeV to more than 99% for $E_T > 15$ GeV.

From 2017 data-taking a new algorithm [23] has been implemented to reconstruct electrons and photons in the ATLAS EM calorimeter. This new approach, known as *topological clustering*, allows for improved measurements of electron and photon energies, particularly when an electron radiates a bremsstrahlung photon or when a photon converts to an e^-e^+ pair. This algorithm scans the EM calorimeter in order to find cells which are characterized by a cell significance, i.e. the ratio between the absolute energy deposit E_{cell}^{EM} in the cell and the expected noise σ_{noise}^{EM} in the cell, above a threshold:

$$\zeta_{cell}^{EM} = \frac{|E_{cell}^{EM}|}{|\sigma_{noise}^{EM}|}. \quad (9)$$

At first the algorithm identifies cells with $\zeta_{cell}^{EM} \geq 4$, then it adds the neighboring cells with $\zeta_{cell}^{EM} \geq 2$ and successively the ones with $\zeta_{cell}^{EM} \geq 0$ around them. Since clusters could include more regions of the detector, a selection (based on the collected energy of the cluster cells in each Layer) is applied to discriminate energy deposit created by electromagnetic or hadronic showers. A candidate electron seed topo-cluster is required to have a $E_T > 1$ GeV; a candidate photon seed topo-cluster must have a transverse energy $E_T > 1.5$ GeV. Starting from the highest energy seed cluster, the algorithm searches for lower E_T satellite clusters in a window (3×5 cells in the middle layer) around the topocluster barycentre. Then, for converted photons, it searches a topocluster matched to the same conversion vertex of the seed cluster or for one matched to one of the tracks associated to the conversion vertex of the seed cluster. Instead, for electrons, it searches clusters in a 5×12 window matched to the same track as the seed topocluster. The union of seed clusters and clusters found in this way is called supercluster.

3.1.2 Track reconstruction and matching

After the selection of an energy clusters in the EM calorimeter, the reconstruction of electrons, converted photons and unconverted photons proceeds to the second step: searching for a track (or the lack of a track in the case of unconverted photons) in the Inner Detector to match the energy clusters. Once a track is reconstructed, a region of interest around the position of seed clusters is defined: every point in this region has an angular distance from the seed cluster barycentre in L2 of 0.05 in the η direction, and of either 0.2 (0.1 for tracks reconstructed from hits only in the TRT) along ϕ in the direction of the bending of the track or 0.05 in the opposite direction. The considered track is then extrapolated to find its intersection point with the L2 layer: the track is loosely matched to an energy cluster in the EM calorimeter if its intersection point with L2 falls within the region of interest built around

that seed cluster. If a track has a significant number of hits (≥ 4) and it is loosely matched to an energy cluster, it is refitted using the Gaussian Sum Filter (GSF) algorithm, which allows an optimized track reconstruction, especially for low- p_T electrons, which may have suffered from significant energy losses from bremsstrahlung. A second matching process is then applied to the refitted tracks: the criteria are similar, except for a stricter condition on the distance of the track from the seed cluster along ϕ , which is required to be smaller than 0.1 in the direction of the bending of the track. If more than one track meets the matching criteria, the track with the smallest angular distance between the extrapolated intersection point on L2 and the seed cluster is selected, unless the angular distances ΔR associated with the candidate tracks differ of less than 0.01. In this case, an algorithm chooses the best track, preferring those with more hits and those with hits in the first silicon layer of the Inner Detector.

3.2 Electrons

3.2.1 Reconstruction

An electron candidate is defined by the existence of one or more reconstructed tracks matched to a seed energy cluster in the EM calorimeter as explained in Section 3.1.2. After finding an electron candidate, its four-momentum is computed: the energy of the electron candidate is the energy in the final cluster; the η and ϕ directions are taken from the corresponding track if the track has hits in the inner layers of the Inner Detector, i.e. the Pixel Detector (at least two hits) and the SCT (at least four hits). If the electron track is reconstructed only from hits in the TRT, η and ϕ of the electron candidate are inferred from the position of the barycentre of the cluster.

In order to discriminate electrons from converted photons and other particles originating from secondary vertices, the track of the candidate electron has to fulfill other selection requirements:

- To be reconstructed as an electron, the candidate particle needs to pass the requirements $\frac{d_0}{\sigma_{d_0}} < 5$. The *transverse impact parameter* d_0 is the distance of closest approach of the track to the z -axis (i.e. the beamline).
- To be reconstructed as an electron, Δz_0 , which is the absolute difference between z_0 of the track of the candidate particle and z_0 of the primary vertex, is requested to be $\Delta z_0 \sin \theta < 0.5$ mm, where θ is the polar angle. z_0 is the *longitudinal impact parameter*, the z coordinate of the closest point of approach of the track to the z -axis.

3.2.2 Identification

In order to determine if the reconstructed electron is a *prompt electron* originated from the hard interaction or it is a jets misidentified as electrons or electrons originated from hadrons

decays, for Run 2 a likelihood-based identification algorithm is applied, with three different operating points: *Loose*, *Medium*, and *Tight*. These working points are defined in such a way that a sample of electrons of tight quality is a subset of a sample of medium electron, which, in turn, is a subset of a sample of loose electrons. These three identification working points have an increasing power - from *Loose* to *Tight* - of rejecting the background electrons or the wrongly reconstructed converted photons from signal prompt electrons from the primary vertex. The discriminating variables used to define these working points, listed in Table 3, are the same for *Loose*, *Medium*, and *Tight*.

3.2.3 Isolation

To further discriminate background electrons from prompt electrons, an isolation requirement is needed. Two types of isolation are implemented:

- The **calorimetric isolation energy** is quantified through the variable $E_T^{cone0.2}$, defined as the sum of the positive transverse energies topological clusters within a cone of radius $\Delta R = 0.2$ around the candidate electron energy cluster, minus the transverse energy of the electron E_T (calculated in a rectangular cell of size 5×7 in $\Delta\eta \times \Delta\phi$ in L2). The idea is to consider the energy deposits in the EM calorimeter which are close to the energy cluster of the candidate electron: if $E_T^{cone0.2}$ is below a certain threshold (that depends on the electron's transverse momentum) the considered electron is calorimetrically isolated. The variables $E_T^{cone0.3}$ and $E_T^{cone0.4}$ are defined at the same way but with a different radius ΔR .
- The **track isolation** is measured through the variable $p_T^{varcone0.2}$, defined as the sum of the transverse momenta of all tracks falling within a cone of radius $\Delta R = 0.2$ (if the transverse energy of the electron is $E_T < 50$ GeV) or $\Delta R = 10 \text{ GeV}/E_T$ (if $E_T > 50$ GeV) around the candidate electron track in the ID. If $p_T^{varcone0.2}$ is below a certain threshold (that depends on the electron's transverse momentum) the considered electron is isolated. As for the calorimetric isolation, the tracks associated to the electron are excluded from the sum.

Changing the cuts that $E_T^{cone0.2}/p_T$ and $p_T^{varcone0.2}/p_T$ have to fulfill, many different standardized isolation working points are defined. For example the FixedCutTight isolation working point for electrons is:

$$E_T^{cone0.2} < 0.060 \cdot p_T, \quad p_T^{varcone0.2} < 0.060 \cdot p_T, \quad (10)$$

3.3 Photons

3.3.1 Reconstruction

The reconstruction of photons is done in a similar way as for the electrons, but with some additional steps to discriminate between electrons and converted photons: an energy cluster

Type	Description	Name
Hadronic leakage	- Ratio of E_T in the first layer of the hadronic calorimeter to E_T of the EM calorimeter (in the pseudorapidity range $ \eta < 0.8$ or $ \eta > 1.37$)	R_{had1}
	- Ratio of E_T in the first layer of the hadronic calorimeter to E_T of the EM calorimeter (in the pseudorapidity range $0.8 < \eta < 1.37$)	R_{had}
Layer 3 of the EM calorimeter	Ratio of the energy in the back layer to the total energy in the EM calorimeter. This variable is only used below 100 GeV because it is known to be inefficient at high energies.	f_3
Layer 2 of the EM calorimeter	- Lateral shower width $\sqrt{(\sum E_i \eta_i^2)/(E_i) - ((\sum E_i \eta_i)/(\sum E_i))^2}$, where E_i is the EM calorimeter energy and η_i is the pseudorapidity of cell i and the sum is calculated within a window of 3×5 cells	w_n^2
	- Ratio of the energy in 3×3 cells over the energy in 3×7 cells centered at the electron cluster position	R_ϕ
	- Ratio of the energy in 3×7 cells over the energy in 7×7 cells centered at the electron cluster position	R_η
Layer 1 of the EM calorimeter	- Shower width, $\sqrt{(\sum E_i(i - i_{max})^2)/(\sum E_i)}$ where i runs over all strips in a window of $\Delta\eta \times \Delta\phi \approx 0.0625 \times 0.2$, corresponding typically to 20 strips in η , and i_{max} is the index of the highest-energy strip	w_{stot}
	- Ratio of the energy difference between the largest and second largest energy E ratio deposits in the cluster over the sum of these energies	E_{ratio}
	- Ratio of the energy in the strip layer to the total energy in the EM accordion calorimeter	f_1
Track conditions	- Number of hits in the innermost pixel layer; discriminates against photon conversions	n_{Blayer}
	- Number of hits in the Pixel Detector	n_{Pixel}
	- Number of total hits in the pixel and SCT detectors	n_{Si}
	- Transverse impact parameter with respect to the beam-line	d_0
	- Significance of transverse impact parameter defined as the ratio of d_0 and its uncertainty	d_0/σ_{d_0}
	- Momentum lost by the track between the perigee and the last measurement point divided by the original momentum	$\Delta p/p$
TRT	Likelihood probability based on transition radiation in the TR	eProbabilityHT
Track-cluster matching	- $\Delta\eta$ between the cluster position in Layer 1 and the extrapolated track	$\Delta\eta_1$
	- $\Delta\Phi$ between the cluster position in the Layer 2 and the track extrapolated from the perigee	$\Delta\Phi_2$
	- Defined as $\Delta\Phi_2$, but the track momentum is rescaled to the cluster energy before extrapolating the track from the perigee to the Layer 2 of the calorimeter.	$\Delta\phi_{res}$
	- Ratio of the cluster energy to the track momentum.	E/p

Table 3: Discriminating variables used for electron identification: in the first column the type of the variable is reported, in the second a brief description of the variables is provided and in the last there is the name usually referred to the variable [19].

in the EM calorimeter can be reconstructed as a photon or as an electron or as both of them, depending on the requirements on track reconstruction and matching. Once seed clusters are reconstructed, a search for two types of conversion vertices is done:

- **double-track conversion vertices** are reconstructed from pairs of opposite charged tracks in the Inner Detector, in this case an e^-e^+ pair. Track pairs compatible with originating from a secondary vertex need to fulfill a series of geometric requirements in order to be identified: these geometric characteristics are primarily angular conditions between the two tracks at the point of the tracks' closest approach to the candidate conversion vertex. The geometric requirements are based on where the hits on the Inner Detector are: they are classified as Si-Si if both of them leave hits in the silicon detector, Si-TRT if only one of them fulfils this condition and TRT-TRT track if none of them does. After these selections, the two retained tracks are studied and fitted to find the final double-tracks vertex candidate. The efficiency of reconstruction of double-track vertex candidates decreases rapidly for conversions taking place in the external layers of the Inner Detector: since the TRT has a poorer resolution compared to the silicon detector, softer tracks with a non sufficient angular separation between the two tracks could be reconstructed as a single track.
- **single-track conversion vertices** are therefore reconstructed from tracks without hits in the first layer of the pixel detector and are considered tracks of converted photons, where the second track was missed or unresolved. Since the vertices associated with this type of track cannot be reconstructed from a fit, their position is defined as the first measurements of their track.

After studying the conversion vertices, they are extrapolated to the EM calorimeter to be matched to the energy clusters: for double track conversion both tracks are extrapolated to L2 in the calorimeter if their momenta differ by less than a factor of two, otherwise a straight line is drawn. For single track conversions the extrapolation is done from the last measurement of the associated track:

- if the conversion vertex is built from track(s) with hits on the silicon detector, it is considered to be matched to an energy cluster if their distance in both the η and ϕ directions is smaller than 0.05. If the conversion vertex is a single-track vertex, the accepted distance in the ϕ direction increases to 0.1 in the direction of the bending of the track.
- if the conversion vertex is built from track(s) without hits in the silicon detector (but with hits only in the TRT), the matching requirements are $\Delta\phi < 0.02(0.03)$ in the direction of (opposite to) the bending of the track(s) and $\Delta\eta < 0.35(0.2)$ in the barrel (end-caps) region of the TRT. $\Delta\phi$ and $\Delta\eta$ are the angular distances between the extrapolated position of the reconstructed track(s) on L2 and the position of the energy cluster measured in the calorimeter.

After matching the conversion vertices to the energy clusters, the final discrimination between photons and electrons is done with the following requests, summarized in the scheme of Figure 20:

- **Electron:** a cluster matched to a track with at least two hits in the pixel detector and four hits in the SCT and no conversion vertices is reconstructed as an electron. If the track is part of a conversion vertex the condition for the particle to be reconstructed as an electron is that the vertex must not be a double-silicon track vertex or one of the tracks must have hits in the innermost pixel layer.
- **Unconverted photon:** an energy cluster in the EM calorimeter is reconstructed as an unconverted photon if the cluster does not have matching tracks or conversion vertices associated.
- **Converted photon:** a cluster matched to a track with less than four hits in the silicon detector is reconstructed as a photon. If a track associated with a cluster has no hits in the pixel detector and is part of a double-silicon track vertex, it is reconstructed as a photon.

If a particle does not fulfill any of these requirements and if the ratio between the energy of the cluster and the momentum of the matching track is above 10 or if p_T from the track is smaller than 2 GeV, it is reconstructed both as an electron and as a photon.

3.3.2 Mis-reconstruction of electrons as photons

As said before, electrons ad photons have some identical characteristics: firstly, the electromagnetic showers left in the EM calorimeter by electrons and photons are identical; secondly, while electrons are always identified by a single track originating from the primary vertex of interaction pointing to an energy cluster in the calorimeter, the same signature can be left by photons converting early in the inner detector with a single-track conversion vertex. Although the reconstruction algorithm for electrons and photon is designed to minimize the mis-reconstruction of electrons as photons (and vice-versa), a small fraction of electrons faking photons can result from the reconstruction procedure: this is mainly due to detector imperfections as broken modules in the Inner Detector, fact that can result in bad track reconstruction or bad matching of tracks with their energy clusters in the calorimeter. If, for example, an electron goes through a dead module in the pixel detector, this would result, after the reconstruction procedures, in a candidate electron with no hits in the pixel detector and this could lead to a mis-reconstruction of the candidate single-track vertex of the electron track as a converted photons with a single-track vertex. Bad reconstruction of energy cluster caused directly by the EM calorimeter is rarer because its reconstruction efficiency is near 100 % [22].

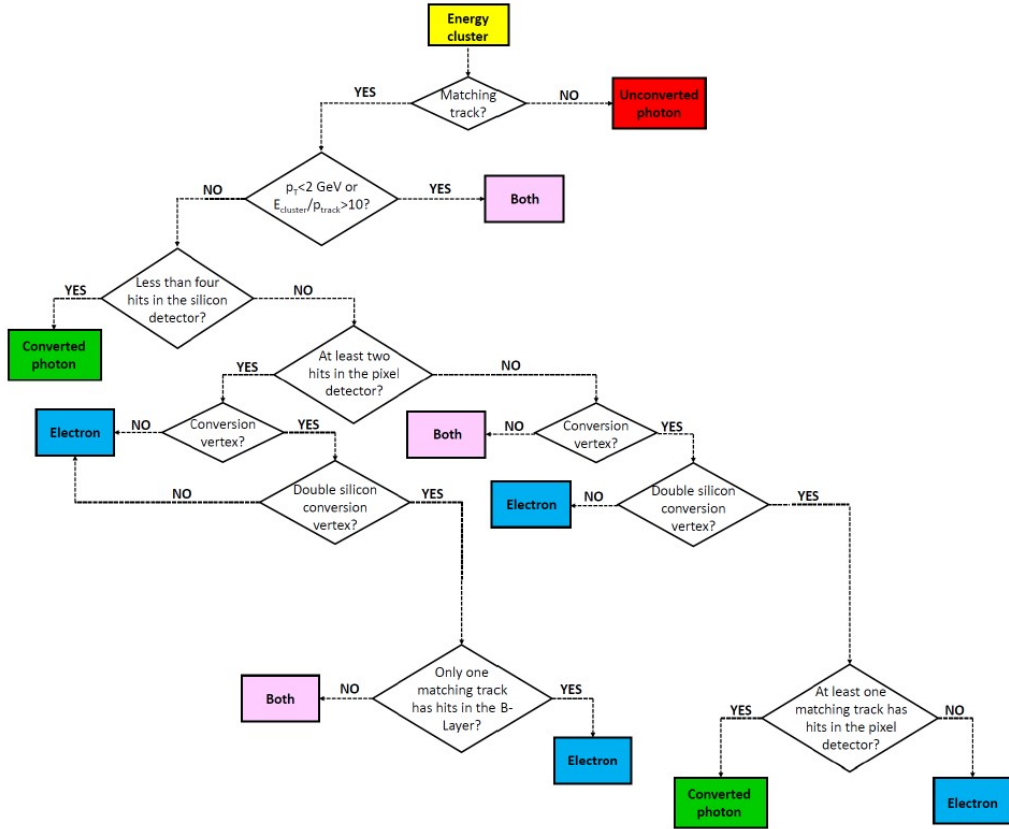


Figure 20: A scheme of the reconstruction steps of a candidate particle as an electron or as a photon.

3.3.3 Identification

As for electrons, identification allows to discriminate between *prompt photons* and *background photons* originating from QCD jets: prompt photons are the ones that are created in processes that could involve DM in colliders as LHC (DM + γ in the Mono-Photon analysis, Chapter 4). Compared to hadronic jets, prompt photons produce a smaller leakage in the hadronic calorimeter and a narrower energy deposit in the EM calorimeter. An important source of background consists of high energy π^0 from jets decaying in a pair of photons $\pi^0 \rightarrow \gamma\gamma$. This decay can be identified by looking for two separate local energy maxima in the first layer of the calorimeter, whose fine segmentation permits to distinguish between these collimated photon pairs and prompt photons. The variables that characterize the two identification working points for photons, *Loose* and *Tight*, are shown in Table 4:

- the Loose identification working point maximizes the prompt photon efficiency with respect to photon reconstruction. The variables used for this working point are shower shapes in L2 and energy clusters in the hadronic calorimeter.

- the Tight identification working point completes the Loose working point adding selections on variables that describe shower shapes in the L1 and in the EM calorimeter.

The efficiency of the tight photon identification varies from 50–60% at $E_T = 10$ GeV, to 95–99% (unconverted) and 88–96% (converted) for photons with E_T above 250 GeV.

Type	Description	Name	Loose	Tight
Acceptance	$\eta < 2.37$, with $1.37 < \eta < 1.52$ excluded - Ratio of E_T in the first layer of the hadronic calorimeter to E_T of the EM calorimeter (in the pseudorapidity range $ \eta < 0.8$ or $ \eta > 1.37$)	R_{had1}	•	•
Hadronic leakage	- Ratio of E_T in the first layer of the hadronic calorimeter to E_T of the EM calorimeter (in the pseudorapidity range $0.8 < \eta < 1.37$)		•	•
Layer 2 of the EM calorimeter	- Lateral shower width $\sqrt{(\sum E_i \eta_i^2)/(E_i) - ((\sum E_i \eta_i)/(\sum E_i))^2}$, where E_i is the EM calorimeter energy and η_i is the pseudorapidity of cell i and the sum is calculated within a window of 3×5 cells - Ratio of the energy in 3×3 cells over the energy in 3×7 cells centered at the electron cluster position - Ratio of the energy in 3×7 cells over the energy in 7×7 cells centered at the electron cluster position	w_n^2	•	•
Layer 1 of the EM calorimeter	- Shower width, $\sqrt{(\sum E_i(i - i_{max})^2)/(\sum E_i)}$ where i runs over all strips in a window of $\Delta\eta \times \Delta\phi \approx 0.0625 \times 0.2$, corresponding typically to 20 strips in η , and i_{max} is the index of the highest-energy strip - Energy outside the core of the three central strips but within seven strips divide by energy within the three central strips. - Difference between the energy associated with the second maximum in L1 and the energy reconstructed in the strip with the minimum value found between the first and second maxima - Ratio of the energy difference between the largest and second largest energy E ratio deposits in the cluster over the sum of these energies - Ratio of the energy in the strip layer to the total energy in the EM accordion calorimeter	R_ϕ	•	•
		R_η	•	•
		w_{stot}	•	•
		f_{side}	•	•
		ΔE_s	•	•
		E_{ratio}	•	•
		f_1	•	•

Table 4: Discriminating variables used for photon loose and tight identification.

3.3.4 Isolation

Photon isolation criteria allow a further rejection of background photons. These criteria are based on the two variables E_T^{iso} and p_T^{iso} referring to calorimeter isolation and track isolation respectively, defined similarly to the isolation variables used for the isolation of electrons [19] [20] [21]:

- E_T^{iso} is computed as the sum of transverse energies of all positive energy topological clusters, in both the hadronic and electromagnetic calorimeters, within a cone of a given radius (0.2, 0.3 or 0.4) around the photon candidate direction. The energy of the photon is excluded from the sum subtracting a rectangle of 5×7 cells from the center

of the cone. Various corrections for the photon energy leakage outside the rectangle and underlying event subtraction are applied.

- p_T^{iso} is defined as the sum of transverse momenta of the tracks found in cones of a given radius centered on the photon direction. A minimum requirement of $p_T = 1$ GeV is applied. Tracks associated to the photon conversion are excluded.

Isolation working points for photons are defined by requirements on these variables. The most commonly adopted are the *Loose* and *Tight* isolation requirements. The first is based on both the calorimeter isolation and the track isolation with $\Delta R = 0.2$:

$$E_T^{iso} < 0.065 \cdot p_T, \quad p_T^{iso} < 0.050 \cdot p_T, \quad (11)$$

where p_T is the transverse momentum of the photon.

4 The Mono-Photon analysis

4.1 Overview

The work presented in this thesis fits into the context of the Mono-Photon analysis, providing a new evaluation of the electrons faking photons background searching for Dark Matter in the Mono-Photon channel. The Mono-Photon analysis looks for an excess of events (with respect to the Standard Model prediction) with a final state composed of a single high transverse momentum photon (γ) and a large missing transverse momentum (E_T^{miss}): this excess may constitute a signature of production of $DM + \gamma$ events in pp collisions at the LHC.

As discussed in Section 1.2.1, many theories of physics beyond the Standard Model (BSM), involve DM particles production in association with γ : since the complexity of BSM theories as Supersymmetry or extra dimensions, due to the large number of their parameters, makes them practically unusable as a guideline for DM search at colliders, the Mono-Photon analysis focuses on **Simplified Dark Matter models**. The Simplified DM models describe the full DM particles' low-energy kinematic at colliders and their coupling with SM particles with only five free parameters: the mass m_{med} of the DM particle m_χ , the mass of the mediator through which χ interacts with quarks and its width Γ_{med} , the couplings of the mediator to quarks (g_q) and to the DM particle (g_χ).

The Mono-Photon analysis is characterized by a relative clean final state, since only few processes give such a final state in the Standard Model:

- The dominant background consists in processes with a Z or W boson produced in association with a photon. Z ($\rightarrow \nu\nu$) + γ is an irreducible background and it constitutes approximately 60% of the total background for the $E_T^{miss} + \gamma$ final state; Z($\rightarrow \mu\mu|ee$) + γ and W($\rightarrow l\nu$) + γ are reducible backgrounds: they are part of the background when a lepton is not detected or when happens a misreconstruction, for example an electron is misreconstructed as a photon.
- The multijet background is strongly reduced by the large E_T^{miss} selection;
- Other important backgrounds, such as top quark and W/Z bosons produced in association with a jet, are reduced by asking a high transverse energy photon.

This chapter presents the results obtained by the Mono-Photon analysis in 2016 [24]: the analysis was performed with Run 2 events, collected with the ATLAS detector in pp collisions at a center-of-mass energy $\sqrt{s} = 13$ TeV, corresponding to an integrated luminosity of 36.1 fb^{-1} , in 2015 and 2016 data-taking.

4.2 Event selection

The requirements to pass the event selection are driven by the effort of achieving a high significance of the expected signal over the predicted SM background and are introduced in

the following Sections.

4.2.1 Pre-selection of events

The pre-selection criteria are common to many ATLAS analyses: they are applied before the specific selection criteria of each analysis in order to discriminate events with instrumental problems such as noise bursts or non-collision background. To pass the pre-selection requirements, the event must have some characteristics:

- The considered event must be included in the *Good Run List* (GRL), a list of all the events that were collected when the LHC and all relevant ATLAS sub-detectors worked at their best functionality;
- The event must pass the *HLT g140 loose* requirement at the HLT level: the trigger selects events with at least one photon candidate with $p_T > 140$ GeV and satisfying the loose identification criteria;
- The reconstructed primary vertex must be associated to at least two good quality tracks with $p_T > 400$ MeV and $|\eta| < 2.5$;
- Events containing jets with $p_T > 20$ GeV, flagged as *Loose Bad* and overlapping with photons or electrons are rejected. A Loose Bad jet is likely to be a fake jet, for example reconstructed from a deposit of energy caused by cosmic rays or noise bursts in the calorimeters.

4.2.2 Object definition

After the considered event passes the pre-selection criteria, all the physics objects (as electrons, photons, muons, jets) in the event are reconstructed and identified, following for example the steps of Chapter 3 for electrons and photons. For each event a list of *preselected* and *selected* objects is built in the following way:

- **Photon:** All the reconstructed photons (Section 3.3.1) of *Loose* quality (Section 3.3.3) with $E_T > 10$ GeV and $|\eta| < 2.37$ are considered preselected photons. A selected photon is a tight isolated (Section 3.3.4) preselected photon and the required isolation working point is the *FixedCutTight*:

$$topoE_T^{cone40} < 0.022 \cdot p_T + 2.45 \text{ GeV}, \quad p_T^{cone20} < 0.05 \cdot p_T, \quad (12)$$

respectively for the calorimetric and the track isolation.

- **Electron:** A preselected electron is a reconstructed electron (Section 3.2.1) with *Medium* identification working point (called *MediumLLH*, Section 3.2.2), $E_T > 7$ GeV and $|\eta| < 2.47$. In addition to these kinematic requirements, a preselected electron

needs to satisfy the two conditions on the longitudinal impact parameter z_0 and on the transverse impact parameters d_0 of the track with respect to the primary vertex described in Section 3.2.1: $\frac{d_0}{\sigma_{d_0}} < 5$ and $\Delta z_0 \sin \theta < 0.5$ mm. Selected electrons are isolated preselected electrons and the required isolation working point is the *Loose* (FCLoose) one:

$$topoE_T^{cone20} < 0.2 \cdot p_T, \quad p_T^{varcone20} TightTTVA1000 < 0.15 \cdot p_T, \quad (13)$$

respectively for the calorimetric and the track isolation.

- **Muon:** Muons are identified either as a combined track in the Muon Spectrometer (MS) and ID systems, or as an ID track matching with a MS segment. Preselected muons have *Medium* quality, $p_T > 6$ GeV, $|\eta| < 2.7$, $\frac{d_0}{\sigma_{d_0}} < 3$ and $\Delta z_0 \sin \theta < 0.5$ mm. Selected muons are defined as the preselected ones, but in addition are required to satisfy the *Loose* isolation working point.
- **Jet:** Preselected jets are reconstructed jets with $p_T > 20$ GeV. Selected jets must have $p_T > 30$ GeV, $|\eta| < 4.5$, and the Jet Vertex Tagger variable must be $JVT < 0.59$ for jets with $30 \text{ GeV} < p_T < 60 \text{ GeV}$ and $|\eta| < 2.4$. The cut on the Jet Vertex Tagger variable JVT is necessary to remove jets originating from pile-up.
- **Missing transverse momentum:** The E_T^{miss} calculation used in the Mono-Photon analysis is based on "preselected" leptons, photons and jets. The E_T^{miss} is calculated as the sum of the following terms:

$$E_{x,y}^{miss} = E_{x,y}^{miss,e} + E_{x,y}^{miss,\gamma} + E_{x,y}^{miss,jets} + E_{x,y}^{miss,\mu} + E_{x,y}^{miss,SoftTerm} \quad (14)$$

where each term is calculated as the negative sum of the calibrated objects momenta, projected onto the x and y directions. The contribution of the Soft Term is calculated from energy deposits or tracks that are not matched to reconstructed physics objects.

Since the reconstruction of objects in the ATLAS detector is not always a simple process, a single candidate particle can be reconstructed as two different objects. To partially resolve these ambiguities, an algorithm of overlap removal is applied to the preselected objects.

4.2.3 Event selection in the Signal Region

An event that passes the pre-selection criteria needs to comply with other requirements to be in the **Signal Region (SR)**, where events with $E_T^{miss} + \gamma$ final state, the DM + γ signature, are expected. The inclusive Signal Regions employed by the Mono-Photon analysis are three, depending on the three different thresholds for the missing transverse momentum E_T^{miss} . The two exclusive Signal Regions lie between a minimum and a maximum value of E_T^{miss} . The inclusive and exclusive SRs are defined in Table 5. Candidates in the SRs are selected by requiring:

Inclusive SRs	$E_T^{miss} > 150 \text{ GeV (ISR1)}$	$E_T^{miss} > 225 \text{ GeV (ISR2)}$	$E_T^{miss} > 300 \text{ GeV (ISR3)}$
Exclusive SRs	$150 \text{ GeV} < E_T^{miss} < 225 \text{ GeV}$	$225 \text{ GeV} < E_T^{miss} < 300 \text{ GeV}$	

Table 5: Definitions of inclusive and exclusive Signal Regions for different E_T^{miss} bins.

- E_T^{miss} needs to be at least greater than 150 GeV; in general it has to be greater than the threshold in the considered SR.
- The considered event must contain at least one preselected loose photon with $p_T > 150 \text{ GeV}$, $|\eta| < 2.37$ excluding the crack region $1.37 < |\eta| < 1.52$.
- The significance of E_T^{miss} , as defined by Equation 9 in Section 3.1.1, must be $\zeta_{cell}^{EM} \geq 8.5 \text{ GeV}^{1/2}$. This requirement significantly reduces the $\gamma + \text{jet}$ background.
- The leading photon must be Tight (identification working point) and isolated (*Fixed-CutTight*).
- The leading photon must be separated from with E_T^{miss} : $\Delta\phi(E_T^{miss}, \gamma) > 0.4$.
- The z coordinate pointed by the leading photon with respect to the identified primary vertex must be lower than 250 mm (*photon pointing*).
- *Jet veto*: events with more than one selected jet are removed and, if there is a jet, this jet must not overlap with E_T^{miss} : $\Delta\phi(E_T^{miss}, \text{jet}) > 0.4$.
- *Lepton veto*: events with any preselected electron or muon are eliminated.

4.3 Background estimation

The SM background to the $E_T^{miss} + \gamma$ final state is due to events containing either a true photon or an object misreconstructed as a photon.

4.3.1 Background sources

The main background sources for the Mono-Photon analysis are:

- $Z(\rightarrow \nu\nu) + \gamma$: this is the main background source and it is also the only irreducible one;
- $W(\rightarrow l\nu) + \gamma$: this is part of the background if the lepton l is not reconstructed or, if l is an electron, it is misidentified as a photon;
- $Z(\rightarrow ll) + \gamma$ is part of the background if both of the leptons are missed by the detectors;

- $Z(\rightarrow \nu\nu) + \text{jet}$: the jet is reconstructed as a photon;
- $Z(\rightarrow ll) + \text{jet}$: the leptons are not detected and the jet is misreconstructed as a photon;
- $W(\rightarrow l\nu) + \text{jet}$: the lepton is not detected and the jet is misreconstructed as a photon;
- $\text{jet} + \gamma$: it contributes to the background if the jet mimics a large E_T^{miss} as a result of a jet reconstruction problem.
- $t\bar{t}$ or single t, or diboson;

4.3.2 Control Regions

To evaluate the main real- γ background contributions, four **Control Regions (CRs)** are defined to constrain the normalization of $W + \gamma$, $Z + \gamma$ and $\gamma + \text{jet}$ Monte-Carlo backgrounds. The idea behind the definition of these CRs is to build signal-free regions, kinematically close to the SRs but orthogonal to them: this is done by inverting one or more selection criteria of the Signal Region (Section 4.2.3) and in this way the considered region is dominated by a single background process. The four CRs are:

- **One-Muon Control Region (1μ CR)**. The definition of this CR is the same as for the SR, except for the muon (lepton) veto: it is required that exactly one selected muon has to be present in the event, therefore the 1μ CR is enriched in $W(\rightarrow \mu\nu) + \gamma$ events. For this CR the E_T^{miss} is defined as described in Section 4.2.2, but the muonic term is subtracted from the computation, so the muons are treated as invisible particles. This control region is therefore used to extract the normalization factor k_W of the $W(\rightarrow \mu\nu) + \gamma$ Monte-Carlo background in the Signal Region.
- **Two-Muon Control Region (2μ CR) and Two-Electron Control Region ($2e$ CR)**. In this case the same selections of the SR are applied, except for the lepton veto: it is required that exactly two selected muons (2μ CR) or two selected electrons ($2e$ CR) are present in the event and no preselected electron (for 2μ CR) or no preselected muon (for $2e$ CR): this CRs are thus enriched with $Z(\rightarrow \mu\mu) + \gamma$ and $Z(\rightarrow ee) + \gamma$ events respectively. In the 2μ CR (or $2e$ CR) the muonic term (or electronic term) is subtracted from the E_T^{miss} computation, such that muons (electrons) are treated as invisible particles. The two-muon (two-electrons) invariant mass is required to be greater than 10 GeV to be coherent with the generator level cut of the $Z + \gamma$ background samples. This second kind of Control Regions is used to constrain the normalization factor k_Z of the $Z + \gamma$ Monte-Carlo events in the SRs; both two-muon and two-electron CRs are considered, in order to improve the statistical power of the constraint on k_Z .

- **Photon-Jet Control Region (PhJet CR).** This Control Region is defined by the same selection criteria of the SR except for a lower E_T^{miss} threshold : $85 \text{ GeV} < E_T^{miss} < 100 \text{ GeV}$ to enrich this region of jet + γ background events. The request $\Delta\phi(\gamma, E_T^{miss}) < 3$ is applied to reduce possible signal contamination (the Control Regions are built to be signal-free), i.e. a true DM + γ signature. This specific photon-jet CR has been defined in Run 2 to constrain the normalization factor k_{jet} of the $\gamma + \text{jet}$ Monte-Carlo background.

4.3.3 Monte-Carlo simulations and the simultaneous fit technique

After defining the different SRs and CRs, the use of Monte-Carlo (MC) simulations is the key to calculate the real- γ background contribution for the Mono-Photon analysis. The MC simulations provide a predicted number of background events; the simulations are then fitted simultaneously to the SR and CRs. The fitted background yields in each region are given by the expected number of background events (retrieved from the MC simulations) in each region multiplied by a factor k , depending exclusively from the considered background process (k_W for the $W + \gamma$ background, k_Z for the $Z + \gamma$ background and k_{jet} for the jet + γ background). While the background yields are fixed parameters in every region (estimated from the nominal MC predictions), the normalization factors for each background source are free parameters of the fit. Each of these factors is not extracted from fitting exclusively the region where the corresponding background source is dominant, but they are evaluated simultaneously: the data from all the regions of the analysis contribute to constrain the fit parameters (and in particular the normalization factors) at the same time. Therefore using a simultaneous fit technique allows a straightforward combination of multiple CRs and permits a coherent treatment of the correlation of the systematic uncertainties across the different regions. The predicted event yield N_R^{obs} in each region R (either the Signal Region or a Control Region) is described as a random variable which follows a Poisson distribution whose expectation value is given by the sum:

$$\begin{aligned}
N_R^{obs} \propto & Pois(N_R^{obs} | \mu N_R^{sig} + N_R^{bkg}) = \\
& = Pois(N_R^{obs} | \mu N_R^{sig} + \\
& + k_Z \times N_R^{Z(\nu\nu)+\gamma} + \\
& + k_W \times N_R^{W(l\nu)+\gamma} + \\
& + k_Z \times N_R^{Z(l\bar{l})+\gamma} + \\
& + k_{jet} \times N_R^{jet+\gamma} + \\
& + N_R^{e-to-\gamma} + N_R^{jet-to-\gamma}),
\end{aligned} \tag{15}$$

where:

- μN_R^{sig} is the signal yield in the region R, μ is the *signal strength* and N_R^{sig} is the number of signal events (from MC simulations);

- $N_R^{Z(\nu\nu)+\gamma}, N_R^{W(l\nu)+\gamma}, N_R^{Z(l)+\gamma}, N_R^{jet+\gamma}$ are the expected real- γ background yields in the region R provided by the MC simulations and they are multiplied by the different normalization factors k ;
- $N_R^{e-to-\gamma}$ and $N_R^{jet-to-\gamma}$ are the two background sources due to events containing an object misreconstructed as a photon, respectively an electron and a jet.

Systematic uncertainties on the predicted number of events are introduced in the fits as *nuisance parameters* θ^i . The presence of the nuisance parameters allows the expected background yields to fluctuate from the nominal MC predictions. The free parameters of the fit are then μ, k_Z, k_W and k_{jet} , while the nuisance parameters θ^i are fitted but constrained parameters. The model of the likelihood built for the Mono-Photon analysis is then

$$\mathcal{L}(\mu, \vec{k}, \vec{\theta}) = \prod_R Pois(N_R^{obs} | \mu N_R^{sig}(\vec{\theta}) + N_R^{bkg}(\vec{\theta}, \vec{k})) f_{constraints}(\vec{\theta}) \quad (16)$$

where \vec{k} is the vector of the normalization factors k_Z, k_W, k_{jet} and $f_{constraints}(\vec{\theta})$ is the product of the Gaussian constraints on the nuisance parameters. A first background-only fit is performed on the CRs to obtain the normalization factors \vec{k} ; after that a second signal fit on the CRs plus the SR is carried out using the full likelihood in Equation 16. It is also possible to perform three separate fits on the three inclusive SRs or perform only one multiple fit on the three inclusive regions (called *multiple bin fit*).

4.3.4 Fake- γ background estimation

The use of MC simulations and the simultaneous fit technique are only applicable for real- γ background sources, with a true photon in the final state. The estimation of event yields from fake- γ background sources, where one physics object is misreconstructed as a photon because of detector imperfections or malfunctions, has to be established with data-driven techniques. As mentioned before, the two fake- γ background sources for the Mono-Photon analysis are from electrons faking photons and jets faking photons. The most interesting one for the purpose of this thesis is the background from electrons faking photons.

Electrons faking photons As explained in Chapter 3, electrons and photons have very similar signatures in the EM calorimeter and they can be distinguished only by looking for tracks from the ID. However the distinction between electrons and photons is rather difficult and a fraction of electrons can be mistakenly identified as photons. In order to derive the contribution of such electron fakes to the event yield, a two-step approach is followed:

- First of all, the probability for electrons to fake photons, called electron-to-photon fake rate, is measured. This **e-to- γ fake rate** is calculated as the ratio of the number of e γ pairs over the number of ee pairs selected from a pure sample of $Z \rightarrow ee$ events, where the electrons in the final state can be reconstructed as electrons or fake photons. The e-to- γ fake rate is derived as a function of p_T and η of the electron faking a photon.

- In the second step, the background contribution coming from electrons faking photons is derived by using the calculated fake rate to scale the number of electrons measured in dedicated Control Regions, called probe-electron Control Regions, selected in a similar way as the Mono-Photon Signal Region, except that the requirement of having one signal photon is replaced by the requirement to have a probe electron. The measured fake rate is used to scale the event yield of every probe-e CR; the obtained number is used as the expected number of fake photons in the corresponding region of the analysis.

The measurement of the electrons faking photons background is described in detail in the dedicated Chapter 5. Tables 6 and 7 show the measured electron-to-photon fake rate in four bins in $(|\eta|, p_T)$ and the number of electrons faking photons in the Signal Regions and in their respective Control Regions for the 2016 analysis as reported in [24].

$ \eta $	p_T [GeV]	Fake rate \pm stat \pm syst
< 1.37	< 200	$1.07 \pm 0.07 \pm 0.21$
	> 200	$0.59 \pm 0.08 \pm 0.14$
> 1.52	< 200	$2.5 \pm 0.2 \pm 0.3$
	> 200	$2.4 \pm 0.3 \pm 0.5$

Table 6: Electron-to-photon fake rate in % with statistical and systematic uncertainties measured for the Mono-Photon analysis in 2016.

E_T^{miss} bins	SR	$1\mu CR$	$2\mu CR$	2e CR	PhJet CR
> 150 GeV	$198.5 \pm 1.8 \pm 18.0 \pm 35.5$	$16.7 \pm 0.5 \pm 1.5 \pm 3.1$	$0.50 \pm 0.09 \pm 0.04 \pm 0.09$	$0.09 \pm 0.04 \pm 0.01 \pm 0.01$	$71.6 \pm 1.1 \pm 6.1 \pm 12.4$
> 225 GeV	$46.7 \pm 0.9 \pm 5.7 \pm 10.0$	$4.2 \pm 0.2 \pm 0.4 \pm 0.9$	$0.17 \pm 0.05 \pm 0.02 \pm 0.04$	$0.052 \pm 0.030 \pm 0.004 \pm 0.009$	$71.6 \pm 1.1 \pm 6.1 \pm 12.4$
> 300 GeV	$13.1 \pm 0.4 \pm 1.7 \pm 2.9$	$1.1 \pm 0.1 \pm 0.1 \pm 0.2$	$0.028 \pm 0.015 \pm 0.003 \pm 0.006$	$0.052 \pm 0.030 \pm 0.004 \pm 0.009$	$71.6 \pm 1.1 \pm 6.1 \pm 12.4$
150 – 225 GeV	$151.8 \pm 1.6 \pm 12.3 \pm 25.5$	$12.4 \pm 0.4 \pm 1.0 \pm 2.2$	$0.32 \pm 0.07 \pm 0.02 \pm 0.06$	$0.036 \pm 0.027 \pm 0.003 \pm 0.005$	$71.6 \pm 1.1 \pm 6.1 \pm 12.4$
225 – 300 GeV	$33.6 \pm 0.7 \pm 4.0 \pm 7.1$	$3.1 \pm 0.2 \pm 0.3 \pm 0.6$	$0.14 \pm 0.05 \pm 0.02 \pm 0.03$	0	$71.6 \pm 1.1 \pm 6.1 \pm 12.4$

Table 7: Electron-to-photon fakes estimated in the SRs and their respective CRs for an integrated luminosity of 36.1 fb^{-1} measured in the Mono-Photon analysis in 2016. The uncertainty is expressed in three terms: the first term is the statistical uncertainty related to the number of events found in the probe-e CR; the second and third terms are the statistical and systematic uncertainties related to the electron fake, respectively. The PhJet CR being defined at low E_T^{miss} values, there is no splitting in various E_T^{miss} bins for this region.

4.4 Results

The table in Figure 21 (from [24]) presents the observed number of events and the SM background predictions in the SRI1, the most inclusive Signal Region with the lowest E_T^{miss} threshold, $E_T^{miss} > 150 \text{ GeV}$. The SM background predictions are obtained from the simultaneous inclusive-SR fit to its CRs for the real- γ backgrounds and from data-driven methods for the fake- γ backgrounds.

	SRI1	1muCR	2muCR	2eleCR	PhJetCR
Observed events	2400	1083	254	181	5064
Fitted background	2600 ± 160	1083 ± 33	243 ± 13	193 ± 10	5064 ± 80
$Z(\rightarrow \nu\nu)\gamma$	1600 ± 110	1.7 ± 0.2	–	–	81 ± 6
$W(\rightarrow \ell\nu)\gamma$	390 ± 24	866 ± 40	1.1 ± 0.3	0.7 ± 0.1	163 ± 9
$Z(\rightarrow \ell\ell)\gamma$	35 ± 3	77 ± 5	233 ± 13	180 ± 10	13 ± 1
$\gamma + \text{jets}$	248 ± 80	33 ± 8	–	–	4451 ± 80
Fake photons from electrons	199 ± 40	17 ± 3	0.50 ± 0.13	0.09 ± 0.04	72 ± 14
Fake photons from jets	152 ± 22	88 ± 19	7.9 ± 3.8	12 ± 5	284 ± 28
Pre-fit background	2400 ± 200	1025 ± 72	218 ± 15	181 ± 13	4800 ± 1000

Figure 21: Observed event yields in 36.1 fb^{-1} of data compared to expected yields from SM backgrounds in the signal region SRI1 and in its four control regions (CRs), as predicted from the simultaneous fit to CRs of SRI1. The MC yields before the fit are also shown. The uncertainty includes both the statistical and systematic uncertainties. The uncertainty on the pre-fit background is the pre-fit uncertainty, while the uncertainties on the fitted background are post-fit uncertainties. The individual uncertainties can be correlated and do not necessarily add in quadrature to equal the total background uncertainty.

As it can be seen from the previous table and from Figure 22, the observed number of events is compatible with the SM background-only hypothesis. The results from the SRs are therefore interpreted in terms of exclusion limits in models that would produce an excess of $E_T^{\text{miss}} + \gamma$ events.

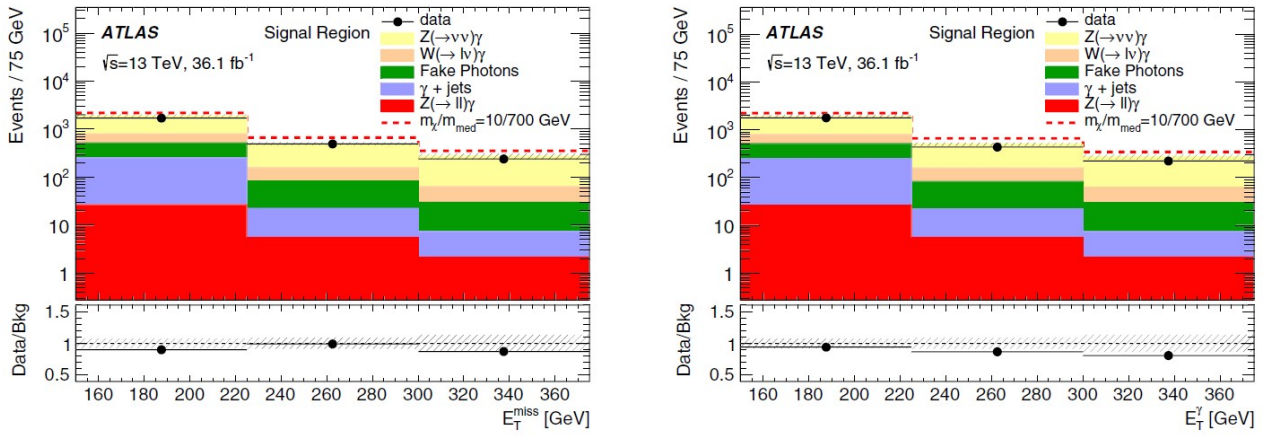


Figure 22: Distribution of E_T^{miss} (left) and of E_T^γ , the transverse momentum of the leading photon, (right) in the three inclusive Signal Regions for data and for the expected total background; the total background expectation is normalised using the scale factors k derived from the multiple-bin fit. The error bars are statistical, and the dashed band includes statistical and systematic uncertainties determined by the fit. The lower panel shows the ratio of data to expected background event yields

5 Measurement of the electrons faking photons background for the Mono-Photon analysis

As mentioned in Section 4.3.4, the background from electrons faking photons is one of the two fake- γ background sources for the Mono-Photon analysis. This fake- γ background derives from the fact that a fraction of prompt electrons can be mistakenly reconstructed and identified as photons. The misreconstruction results from two main reasons:

- firstly, electrons and photons have very similar signatures in the EM calorimeter, as described in more detail in Chapter 3. The discrimination algorithm combines calorimeter and tracking information to classify the candidates. The final choice necessarily introduces a loss of efficiency of true candidates of a given type and a contamination of the other type in the selected sample;
- secondly, the different detectors could have some imperfections, such as broken modules in the Inner Detector.

To evaluate this background source it is not recommended to use MC simulations as for the real- γ background sources because they cannot exactly model the two causes of misreconstruction. Therefore, to estimate the number of electron fakes, a two-step method is used:

- The first step consists in evaluating the *electron-to-photon fake rate* that can be seen as the probability of electrons to be mistakenly reconstructed and identified as photons.
- In the second step, the measured e-to- γ fake rate is used to determine the number of electrons faking photons in each region of the Mono-Photon analysis (in every Signal Region and in its corresponding Control Regions).

The work presented in this thesis consists in implementing the method to measure the e-to- γ fake rate, as described in Section 5.1, and obtain a new measurement of the fake rate using the full Run 2 dataset collected by the ATLAS detector between 2015 and 2018 using the most up to date event reconstruction. The results are then used to provide a new estimation of the contribution from electrons faking photons to the SM background for every region defined in the Mono-Photon analysis (Section 5.2).

5.1 The electron-to-photon fake rate

5.1.1 Definition of the e-to- γ fake rate

The most intuitive definition of the electron-to-photon fake rate is the ratio between the number of electrons wrongly reconstructed and identified as photons $N_{e^{true} \rightarrow \gamma^{reco}}$ over the total number of true electrons $N_{e^{true}}$:

$$\rho = \frac{N_{e^{true} \rightarrow \gamma^{reco}}}{N_{e^{true}}}. \quad (17)$$

However, when using data, the information about the total number of true electrons is not directly accessible; the e-to- γ fake rate is therefore defined as the ratio between the probability to wrongly reconstruct and identify a true electron as a fake photon over the probability to correctly reconstruct a true electron as an electron:

$$F_{e \rightarrow \gamma} \equiv \frac{\epsilon(e^{true} \rightarrow \gamma^{reco})\epsilon_\gamma}{\epsilon(e^{true} \rightarrow e^{reco})\epsilon_e}, \quad (18)$$

where:

- $\epsilon(e^{true} \rightarrow \gamma^{reco}) = \frac{N_{e^{true} \rightarrow \gamma^{reco}}}{N_{e^{true}}}$ is the reconstruction efficiency of electrons as photons, defined as the number of true electrons mistakenly reconstructed as photons over the total number of electrons;
- $\epsilon(e^{true} \rightarrow e^{reco}) = \frac{N_{e^{true} \rightarrow e^{reco}}}{N_{e^{true}}}$ is the reconstruction efficiency of electrons as electrons, defined as the number of true electrons correctly reconstructed as electrons over the total number of electrons;
- ϵ_γ and ϵ_e are the identification efficiencies of photons and electrons respectively, used to correct the reconstruction efficiencies.

Detailing the terms in Equation 18, we obtain a definition of fake rate independent from this non-measurable quantity $N_{e^{true}}$:

$$F_{e \rightarrow \gamma} \equiv \frac{N_{e^{true} \rightarrow \gamma^{reco}}\epsilon_\gamma}{N_{e^{true} \rightarrow e^{reco}}\epsilon_e}. \quad (19)$$

This definition is related to the first intuitive defition of Equation 17 as:

$$F_{e \rightarrow \gamma} = \frac{\rho}{1 - \rho} \frac{\epsilon_\gamma}{\epsilon_e}. \quad (20)$$

This definition of the fake rate as $F_{e \rightarrow \gamma}$ in Equation 19 is also more suitable for the Mono-Photon analysis where the fake rate is applied to dedicated Control Regions [24]. To measure the e-to- γ fake rate as in Equation 19, a physics process where it is possible to discriminate a fake photon, reconstructed from a true electron, from a true electron reconstructed as such, is needed. The process used in this measurement of the fake rate is the $Z \rightarrow ee$ decay, where the two true electrons in the final state can be reconstructed either as a ee couple (actually, one of the two electrons is a positron e^+ , but in all the discussion below e^+ and e^- will be treated as identical particles) or as a $e\gamma$ couple.

In the next paragraphs, the method used to obtain the fake rate is illustrated: for every event in the $Z \rightarrow ee$ sample, it consists in selecting the ee or $e\gamma$ couple whose invariant mass m_{ee} or $m_{e\gamma}$ is the closest to the nominal mass of the Z boson $m_Z = 91.19$ GeV. After this selection, the invariant mass spectra of both the ee and $e\gamma$ couples are reconstructed;

from these spectra the numbers of ee and e γ couples are estimated inside a small mass range around the nominal value (about from 81 GeV to 101 GeV) subtracting the yields of background candidates obtained from the side-bands. The fake rate is measured as a function of η in the range (-2.37, 2.37) and as a function of p_T in different $|\eta|$ intervals (0-0.8-1.15-1.37, 1.52-1.81-2.01-2.37) where the transverse momentum values lie between 25 GeV and 250 GeV. The results are presented for the overlap removal procedure favouring electrons over photons (Overlap Removal retaining electrons or ORel) and for the overlap removal procedure favouring photons over electrons (ORph); the overlap removal algorithm is a technique used in ATLAS to avoid ambiguities between objects reconstructed as two different particles (explained in Section 5.1.2).

5.1.2 Event selection, Overlap Removal and selection of the *best couple*

The events from the $Z \rightarrow ee$ sample must meet some requirements:

- The events are required to contain at least two electrons or an electron and a photon satisfying the preselection criteria of the Mono-Photon analysis (Sections 4.2.1 and 4.2.2);
- Kinematic selection: the transverse momentum (both of electrons and of photons) is required to be greater than 25 GeV and the allowed values of $|\eta|$ are $|\eta| < 2.37$ excluding the crack region of the EM calorimeter $1.37 < |\eta| < 1.52$;
- Electrons are required to satisfy the *Medium* identification working point (called MediumLLH); photons needs to satisfy the *Tight* identification working point;
- The *overlap removal* procedure is then applied on the objects that have passed these first selections: if an electron and a photon in the same event fall within a cone of radius $\Delta R < 0.4$ from each other, the photon is removed when applying the overlap removal algorithm favouring electrons while the electron is removed in the overlap removal algorithm retaining photons;
- The objects in the events that pass the overlap removal algorithm need to be isolated: electrons are required to be selected by the *Loose* isolation working point (FCLoose, described in Section 4.2.2), an efficiency-based operating point optimized to obtain an efficiency of $\sim 99\%$ on a sample of electrons of tight quality. Photons need to be selected by the *FixedCutTight* isolation working point (Section 4.2.2).
- If more than an ee pair or an e γ pair in the same event pass all the previous requirements, the couple (called *best couple*) whose invariant mass is the closest to the Z boson nominal mass, is retained.

5.1.3 Invariant mass distributions for the fake rate estimation

The fake rate is measured as a function of η ($F_{e \rightarrow \gamma}(\eta)$) in the (-2.37, 2.37) range using bins of fixed width equal to 0.1, excluding the crack region (-1.5, -1.4) and (1.4, 1.5): the η range is therefore divided in 46 bins.

The fake rate is also measured as a function of $|\eta|$ and p_T ($F_{e \rightarrow \gamma}(|\eta|, p_T)$); the $|\eta|$ range is divided in 6 bins and in every $|\eta|$ bin the p_T range is divided in 8 bins for a total of 48 bins:

- 6 bins in $|\eta|$: 0-0.8, 0.8-1.15, 1.15-1.37, 1.52-1.81, 1.81-2.01, 2.01-2.37;
- 8 bins in p_T (in GeV): 25-35, 35-45, 45-55, 55-65, 65-75, 75-100, 100-150, 150-250.

The best couple for each event, retained after all the selection criteria of the previous Section, is used to fill the corresponding invariant mass distributions in the following way:

- If the selected best couple of an event is a ee couple, the pseudorapidities η and $\tilde{\eta}$ of the two electrons are matched to their corresponding η^e bins for the measurement of the fake rate as a function of η . Every η^e bin is in turn matched to an invariant mass distribution m_{ee} which is filled with the invariant mass of the ee best couple. If, by chance, the pseudorapidities of both the electrons belong to the same η^e bin, the corresponding invariant mass distribution is filled twice with the same invariant mass. The same procedure is applied to fill the invariant mass distributions associated to the $(|\eta|^e, p_T^e)$ bins for the measurement of the fake rate as a function of both $|\eta|$ and p_T : the absolute value of the pseudorapidity and the transverse momentum of each electron is matched to the relative $(|\eta|^e, p_T^e)$ bin, which is then linked to an invariant mass distribution filled with the m_{ee} of the couple.
- If the selected best couple of an event is an $e\gamma$ couple, only the characteristics of the photon are used to fill the invariant mass distributions. The pseudorapidity of the photon is matched to the right η^γ bin and the corresponding distribution is filled with the mass $m_{e\gamma}$ of the $e\gamma$ couple; $|\eta|$ and p_T of the photon are then linked to the relative $(|\eta|^\gamma, p_T^\gamma)$ bin and the $m_{e\gamma}$ distribution is filled. Therefore, if the best couple is an $e\gamma$ pair, only one $m_{e\gamma}$ distribution is filled per event.

A graphical illustration of this procedure is shown in Figure 23. This procedure is done for both the overlap removal algorithms. In Figure 24 the two inclusive (with no binning in η or p_T) invariant mass distributions m_{ee} for ee couples for the two overlap removal procedures are shown for the OR retaining electrons and OR retaining photons.

As a further example, in Figure 25 the invariant mass distributions m_{ee} and $m_{e\gamma}$ associated to the (-2.4,-2.3) η bin are reported for the OR retaining electrons.

The fake rate as a function of η and the fake rate as a function of $|\eta|$ and p_T are then computed as:

$$F_{e \rightarrow \gamma}(\eta) = \frac{S_{e\gamma}(\eta^\gamma)}{S_{ee}(\eta^e)} \quad F_{e \rightarrow \gamma}(|\eta|, p_T) = \frac{S_{e\gamma}(|\eta|^\gamma, p_T^\gamma)}{S_{ee}(|\eta|^e, p_T^e)} \quad (21)$$

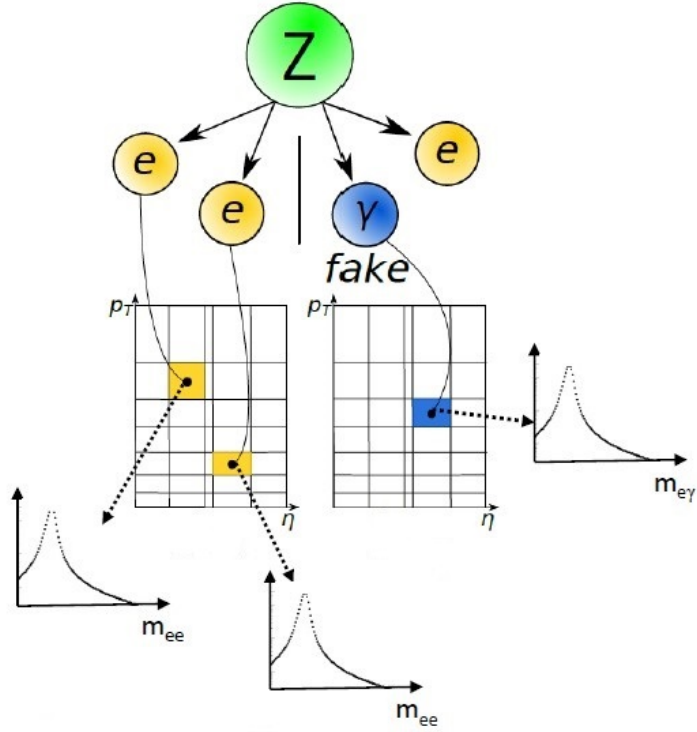


Figure 23: Graphical illustration of the method used to fill the invariant mass distributions. Each $(|\eta|^e, p_T^e)$ bin corresponds to a m_{ee} or to a $m_{e\gamma}$ invariant mass distribution.

where S_{ee} and $S_{e\gamma}$ are the number of signal events extracted from the m_{ee} and $m_{e\gamma}$ distributions respectively. The motivations of the method of filling the invariant mass distributions and of the computation of the fake rate as in Equation 21 are explained below.

As a first approximation, if the background contribution is neglected (as described in the next Section), assuming that the number of signal events S_{ee} and $S_{e\gamma}$ in Equation 21 coincides with the total number of events N_{ee} and $N_{e\gamma}$ from the invariant mass distributions m_{ee} and $m_{e\gamma}$: $S_{ee} = N_{ee}$ and $S_{e\gamma} = N_{e\gamma}$. Then, the motivations can be more easily understood considering only the inclusive case, with no binning in η or p_T , as in Figure 24 for the ee couples. Given the $Z \rightarrow ee$ event sample, being ϵ_γ and ϵ_e the identification efficiencies of photons and electrons respectively and being ρ the intuitive fake rate defined in Equation 17, the probability to have a certain number of selected events for each possible final state ($ee, e\gamma, \gamma\gamma$) is described by the equations:

$$N_{ee} = \epsilon_e^2 (1 - \rho)^2 N_Z \quad (22)$$

$$N_{e\gamma} = 2\epsilon_e\epsilon_\gamma\rho(1 - \rho)N_Z \quad (23)$$

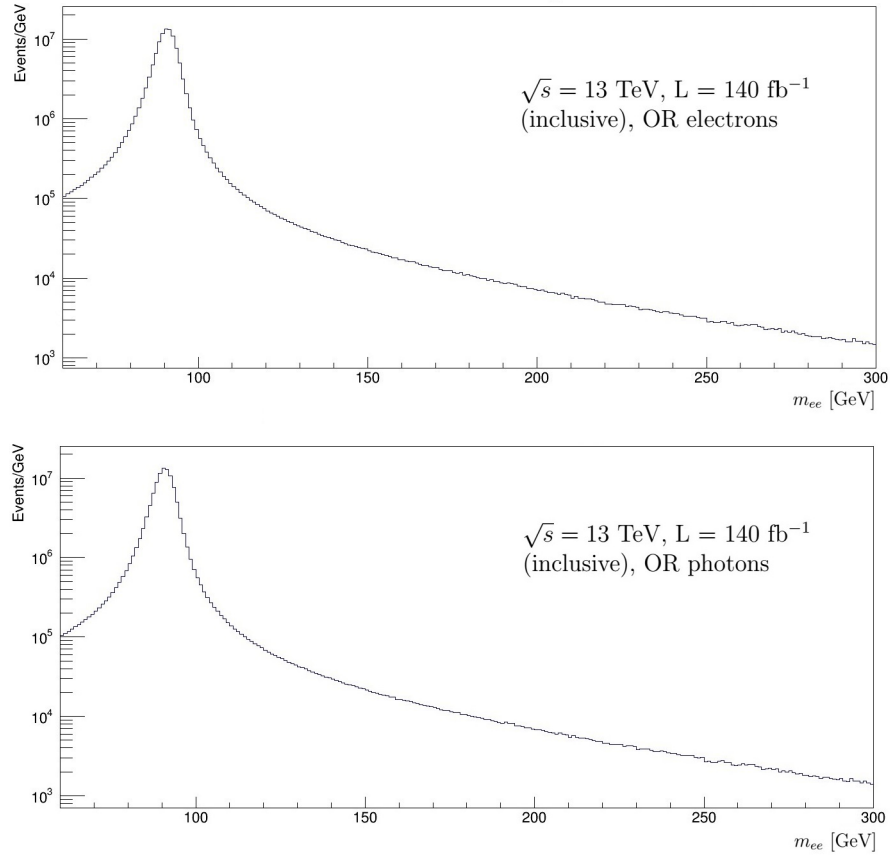


Figure 24: The two inclusive invariant mass distributions m_{ee} for ee couples obtained following the procedure described above for the two overlap removals: OR retaining electrons (top) and OR retaining photons (bottom).

$$N_{\gamma\gamma} = \epsilon_\gamma^2 \rho^2 N_Z \quad (24)$$

where N_Z is the number of true $Z \rightarrow ee$ events and N_{ee} , $N_{e\gamma}$, $N_{\gamma\gamma}$ are the number of reconstructed events for each possible final state. The factor 2 in Equation 23 takes into account both cases in which either the leading electron is wrongly reconstructed as a photon ($ee \rightarrow \gamma^{fake} e$) or the subleading electron is misreconstructed ($ee \rightarrow e\gamma^{fake}$). The definition of the fake rate of Equation 19 can be expressed as

$$F_{e \rightarrow \gamma} = \frac{N_{e^{true} \rightarrow \gamma^{reco}} \epsilon_\gamma}{N_{e^{true} \rightarrow e^{reco}} \epsilon_e} = \frac{N_{e\gamma} + 2N_{\gamma\gamma}}{2N_{ee} + N_{e\gamma}} \quad (25)$$

The second equation is valid because:

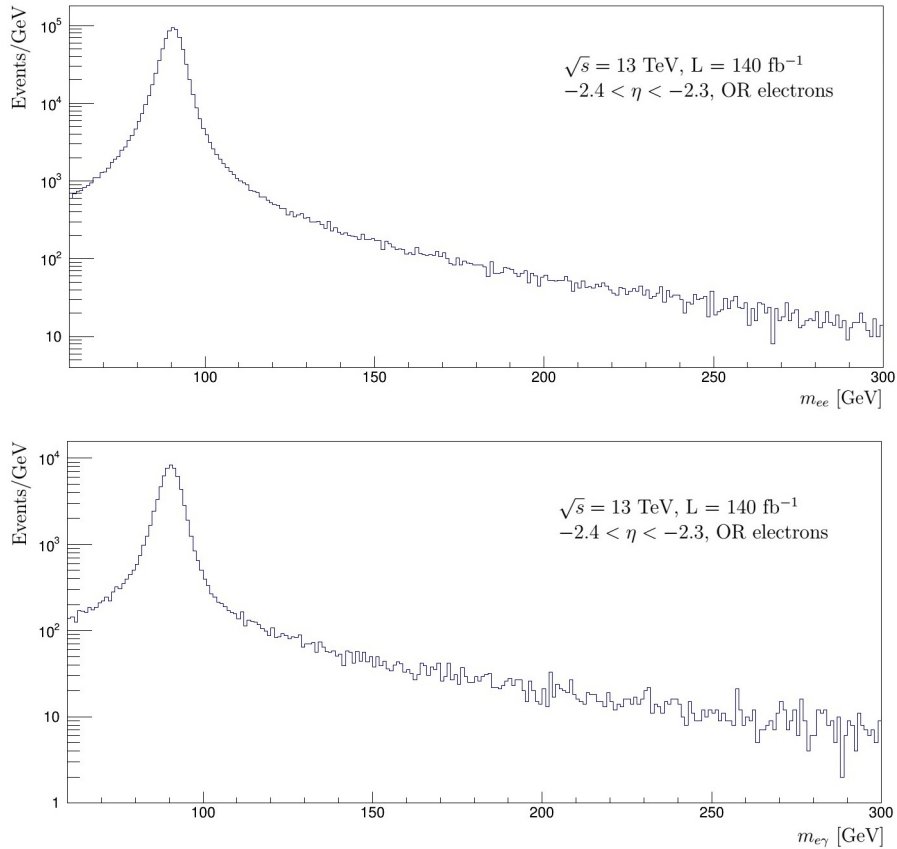


Figure 25: The two invariant mass distributions m_{ee} (top) and $m_{e\gamma}$ (bottom) associated to the (-2.4,-2.3) η bin obtained following the procedure described above for the OR retaining electrons.

- the number of true electrons misreconstructed as photons is given by the number of reconstructed $e\gamma$ couples (where a single electron is misreconstructed) plus two times the number of $N_{\gamma\gamma}$ final states in which both electrons are misreconstructed;
- the number of true electrons correctly reconstructed as electrons is given by the number of reconstructed $e\gamma$ couples (where only one electron is correctly reconstructed) plus two times the number of N_{ee} final states in which both electrons are correctly reconstructed;

Replacing and simplifying the various terms in Equation 25 with Equations 22, 23 and 24, we obtain again Equation 20:

$$F_{e \rightarrow \gamma} = \frac{N_{e^{true} \rightarrow \gamma^{reco}} \epsilon_\gamma}{N_{e^{true} \rightarrow e^{reco}} \epsilon_e} = \frac{N_{e\gamma} + 2N_{\gamma\gamma}}{2N_{ee} + N_{e\gamma}} = \frac{\rho}{1 - \rho} \frac{\epsilon_\gamma}{\epsilon_e}. \quad (26)$$

The same value can be obtained also from the quantity $\frac{N_{e\gamma}}{2N_{ee}}$:

$$\frac{N_{e\gamma}}{2N_{ee}} = \frac{2\epsilon_e \epsilon_\gamma \rho (1 - \rho) N_Z}{2\epsilon_e^2 (1 - \rho)^2 N_Z} = \frac{\rho}{1 - \rho} \frac{\epsilon_\gamma}{\epsilon_e}. \quad (27)$$

Therefore, the fake rate can be computed as

$$F_{e \rightarrow \gamma} = \frac{N_{e\gamma}}{2N_{ee}} \quad (28)$$

which is exactly what happens if the invariant mass distributions are filled as described above and in Figure 23.

5.1.4 Background subtraction

If in Equation 28 we replace $N_{e\gamma}$ and N_{ee} with $S_{e\gamma}$ and S_{ee} we obtain the equation that allows us to compute the fake rate:

$$F_{e \rightarrow \gamma} = \frac{S_{e\gamma}}{2S_{ee}}. \quad (29)$$

The fake rate in a certain bin is therefore measured as the ratio of $S_{e\gamma}$ to S_{ee} , where $S_{e\gamma}$ and S_{ee} are the signal events extracted from the $m_{e\gamma}$ and m_{ee} distributions matched to the selected bin. The discrimination of signal events from jet background events is provided by fitting the invariant mass distributions with a *signal + background* model. The main characteristics of the model are defined in the same way for the two measurements of the fake rate, as a function of η and as a function of $|\eta|$ and p_T . In both cases the invariant mass distributions show a narrow signal peak centered on the mass $m_Z = 91.19$ GeV of the Z boson that stands out from a non-resonant background. Therefore the model consists of:

- a double-sided Crystal Ball (DSCB), a distribution with a gaussian core and two power-law tails, for the modeling of the signal distribution (*PDFs*).
- an exponential of a second-degree polynomial e^{-ax-bx^2} for the background modeling.

The free parameters of the fit are:

- the parameters describing the shape of the double-Sided Crystal Ball distribution: μ_0 and σ_0 are respectively the mean and the standard deviation of the gaussian core of the DSCB, n_{Low} and n_{High} are the powers of the power-law tails on the left and on the right of the peak and finally α_{Low} and α_{High} are the parameters describing the connection between the gaussian core and the tails on the left and on the right of the peak;
- the parameters describing the shape of the background distribution a and b ;

- the normalization factors N_S and N_B for the signal and background distributions respectively.

As examples of this *signal + background* fit, in Figure 26 the fits on the inclusive m_{ee} distributions of Figure 24 are reported, while in Figure 27 the fits on the m_{ee} and $m_{e\gamma}$ distributions associated to the (-2.4,-2.3) η bin of Figure 25 are shown.

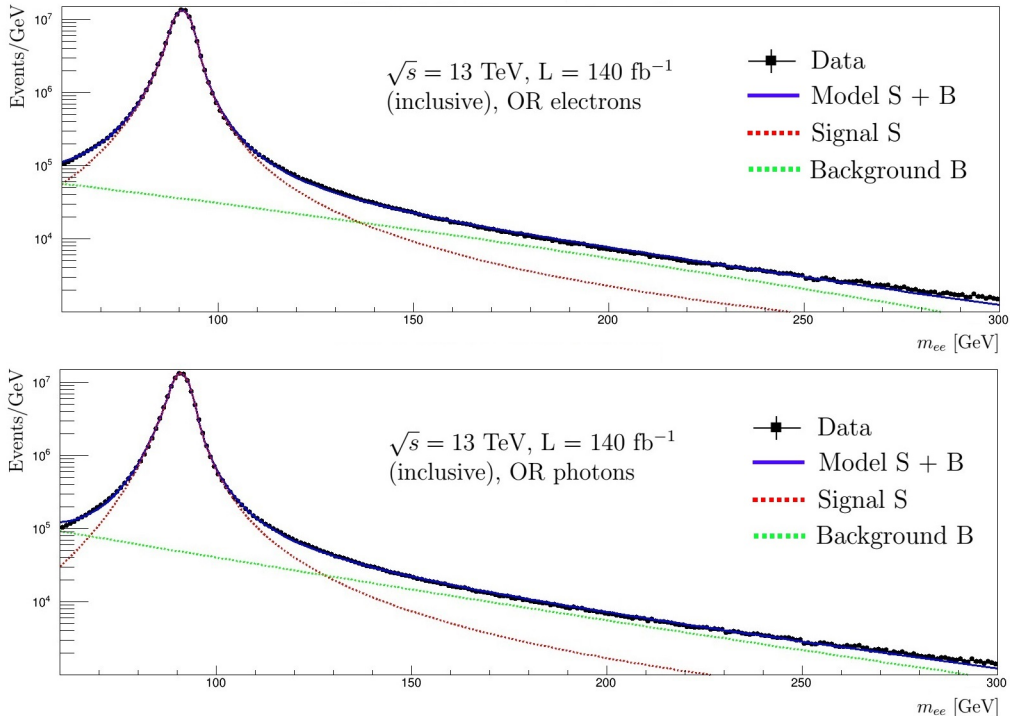


Figure 26: The two signal + background model fits on the inclusive invariant mass distributions m_{ee} for ee couples obtained for the two overlap removals: OR retaining electrons (top) and OR retaining photons (bottom). The signal and background models are shown by the red and green dotted line respectively, while the blue line shows the global model fit.

In the case of the mass distributions labelled by $(|\eta|, p_T)$ bins, a secondary broad peak shows up, centered on the lower value of the transverse momentum in the considered bin multiplied by 2, whose presence is due to kinematic cuts on p_T . Therefore, in this case, the signal distribution is not only modeled by the DSCB for the narrow Z-peak, but also by a gaussian distribution for the secondary broad peak; so the free parameters describing the shape of the gaussian distribution are added to the parameters mentioned before: the mean μ and the standard deviation σ . An example of this model is shown in Figure 28.

Performing a fit on the mass distributions allows to select pure $Z \rightarrow ee$ final states by considering only the signal distribution to extract $S_{e\gamma}$ and S_{ee} . $S_{e\gamma}$ and S_{ee} are ultimately

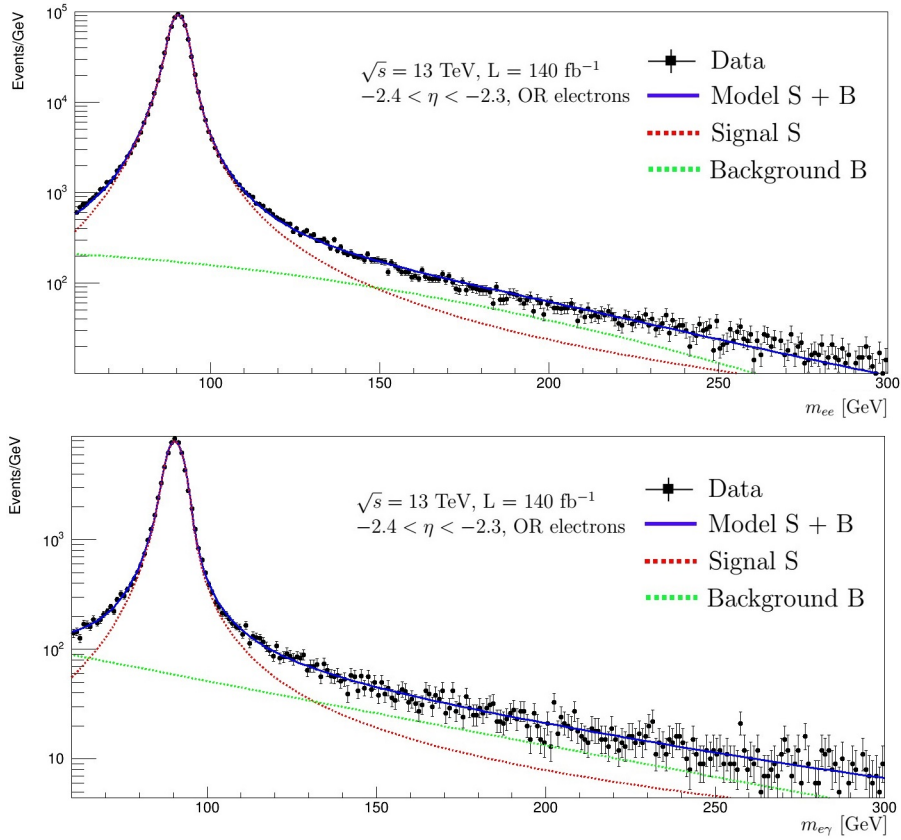


Figure 27: The two signal + background model fits on the invariant mass distributions m_{ee} (top) and $m_{e\gamma}$ (bottom) associated to the $0-0.8$ $|\eta|$ bin and the $150-250$ GeV p_T bin obtained for the OR retaining electrons. The signal and background models are shown by the red and green dotted line respectively, while the blue line shows the global model fit.

obtained by integrating the corresponding signal distributions multiplied for their normalization factors N_S , obtained from the fits, in a determined invariant mass window centered around the Z-peak to exclude the distributions' tails, mainly filled with background events. For both m_{ee} and $m_{e\gamma}$ distributions the window corresponds to $w_3 = [\mu_0 - 3\sigma_{ee}, \mu_0 + 3\sigma_{ee}]$, with μ_0 the peak position of the considered fit and σ_{ee} the standard deviation of the DSCB retrieved from fitting the inclusive m_{ee} distributions shown in Figure 26 for the two overlap removal procedures:

$$\text{ORel : } \sigma_{ee} = 2.7533 \pm 0.0004 \quad \text{ORph : } \sigma_{ee} = 2.7698 \pm 0.0004 \quad (30)$$

$$S_{e\gamma} = \int_{w_3} N_S \text{PDF}_S^{e\gamma} dm_{e\gamma} \quad S_{ee} = \int_{w_3} N_S \text{PDF}_S^{ee} dm_{ee}. \quad (31)$$

The choice of an invariant mass window which is symmetric around the peak position was made to take into account the slight shift between m_{ee} and $m_{e\gamma}$ distributions. The calibration of the energy of the fake photon in the reconstructed $e\gamma$ final state is performed assuming that the reconstructed photon is, indeed, a photon. Therefore, the energy measured by the calibration algorithm is slightly different from the calibrated energy which would be attributed to the particle if the latter were correctly reconstructed as an electron. The observed slight shift between m_{ee} and $m_{e\gamma}$ distributions is a result of the effect on energy calibration caused by misreconstruction of electrons.

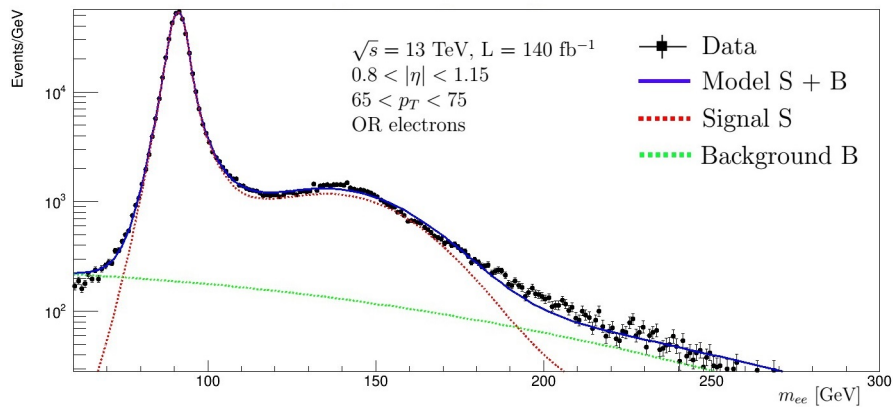


Figure 28: An example of the signal + background model fit where the signal distribution is described by the DSCB + gaussian for the invariant mass distributions m_{ee} associated to the $0.8\text{-}1.15$ $|\eta|$ bin and the $65\text{-}75$ GeV p_T bin for the OR retaining electrons. The signal and background models are shown by the red and green dotted line respectively, while the blue line shows the global model fit.

5.1.5 Systematic uncertainties

Three main sources of systematic uncertainties related to the methodology used to perform the measurement have been identified. They are the invariant mass range w_3 used to calculate the integrals of the signal distributions S_{ee} and $S_{e\gamma}$, the effect of the background subtraction and the bias in the reconstructed photons energy due to the fact that the energy calibration is performed as for true photons. These systematic uncertainties on the measured fake rates have been estimated in the following way:

- *mass range*: the numbers of signal events S_{ee} and $S_{e\gamma}$ are estimated by integrating the corresponding signal distributions in invariant mass windows of smaller and larger widths than the nominal window w_3 . These windows are respectively $w_2 = [\mu_0 - 2\sigma_{ee}, \mu_0 + 2\sigma_{ee}]$ and $w_4 = [\mu_0 - 4\sigma_{ee}, \mu_0 + 4\sigma_{ee}]$. The two variations of the fake rate

are therefore obtained from more and less pure samples of Z boson decays. The contribution to the systematic uncertainty from this source is evaluated as the maximum of the absolute values of the differences between the nominal value of the fake rate, obtained with the w_3 window, and the fake rates obtained with the modified ranges w_2 and w_4 . The impact of this systematic uncertainty is $\sim (1 - 3)\%$ for the $F_{e \rightarrow \gamma}(\eta)$ and $\sim (1 - 4)\%$ for the $F_{e \rightarrow \gamma}(|\eta|, p_T)$;

- *background subtraction:* to evaluate the contribution to the systematic uncertainty of the background subtraction, a measure of the fake rate is performed integrating directly the whole m_{ee} and $m_{e\gamma}$ distributions in the mass range w_3 without performing the signal + background fit. The contribution to the systematic uncertainty from this source is evaluated as the absolute value of the difference between the fake rate obtained in this way and the nominal value of the fake rate. The impact of this systematic uncertainty is about $\sim (3 - 6)\%$ for the $F_{e \rightarrow \gamma}(\eta)$ and $\sim (3 - 8)\%$ for the $F_{e \rightarrow \gamma}(|\eta|, p_T)$;
- *bias in the reconstructed energy of the photon:* the energy of the fake photons was increased and decreased by 1.5% before applying the selection criteria of Section 5.1.2. The value of 1.5% was chosen after comparing the positions of the peak of m_{ee} and $m_{e\gamma}$ distributions. Let's consider a true final state $e_1 e_2$, where the second electron is mistakenly reconstructed as a photon. If the electron was correctly reconstructed as an electron, its calibrated energy would be E_{e_2} . Instead, the calibrated energy of the fake photon is E_γ . A scale factor α_{fake} , depending of course from η and p_T of the fake photon, is assumed between E_γ and E_{e_2} . The invariant mass of an ee couple and an e γ couple would then be:

$$m_{ee} = \sqrt{2 E_{e_1} E_{e_2} (1 - \cos \theta)} \quad (32)$$

$$m_{e\gamma} = \sqrt{2 E_{e_1} E_{e_\gamma} (1 - \cos \theta)} = \sqrt{2 E_{e_1} \alpha_{fake} E_{e_2} (1 - \cos \theta)}. \quad (33)$$

The scale factor α_{fake} is therefore estimated to coincide with $(\frac{m_{e\gamma}}{m_{ee}})^2$. The contribution to the systematic uncertainty from this source is evaluated as the maximum of the absolute values of the differences between the nominal value of the fake rate, obtained with the window w_3 , and the fake rates obtained with the modified energy at the beginning of the selections. The impact of this systematic uncertainty is $\sim (1 - 4)\%$ for the $F_{e \rightarrow \gamma}(\eta)$ and $\sim (8 - 10)\%$ for the $F_{e \rightarrow \gamma}(|\eta|, p_T)$.

5.1.6 Results

Fake rate as a function of η

The electron-to-photon fake rate as a function of η is reported in Figure 29 for the two overlap removal procedures, OR retaining electrons and OR retaining photons. Both the systematic (yellow bands) and total (error bars) uncertainties are highlighted: the total uncertainty, corresponding to the combination in quadrature of statistic and systematic uncertainties, is always dominated by the systematic component. The corresponding measured values are reported in Tables 8 and 9:

- for the OR retaining electrons, the e-to- γ fake rate is approximately 1.7% for η close to 0 reaching about 9% for $\eta \sim \pm 2.4$. The total uncertainty is approximately 9% of the fake rate in the central region ($\eta \sim 0$) and about 1-2% in the external region ($\eta \sim \pm 2.4$);
- for the OR retaining photons, the e-to- γ fake rate is approximately 2.1% for η close to 0 reaching about 10.5% for $\eta \sim \pm 2.4$. The total uncertainty is approximately 6% of the fake rate in the central region ($\eta \sim 0$) and about 2% in the external region ($\eta \sim \pm 2.4$);

In Figure 30, the electron-to-photon fake rate as a function of η is reported separately for converted and unconverted photons for the overlap removal retaining electrons. The corresponding measured values are reported in Tables 10 and 11. The fake rate increases with the absolute value of η :

- for unconverted photon, the e-to- γ fake rate is approximately 0.8% for η close to 0 reaching about 1.7% for $\eta \sim \pm 2.4$. The total uncertainty is approximately 9% of the fake rate in the central region ($\eta \sim 0$) and about 1-2% in the external region ($\eta \sim \pm 2.4$);
- for converted photons, the e-to- γ fake rate is approximately 1% for η close to 0 reaching about 7% for $\eta \sim \pm 2.4$. The total uncertainty is approximately 12% of the fake rate in the central region ($\eta \sim 0$) and about 6-7% in the external region ($\eta \sim \pm 2.4$).

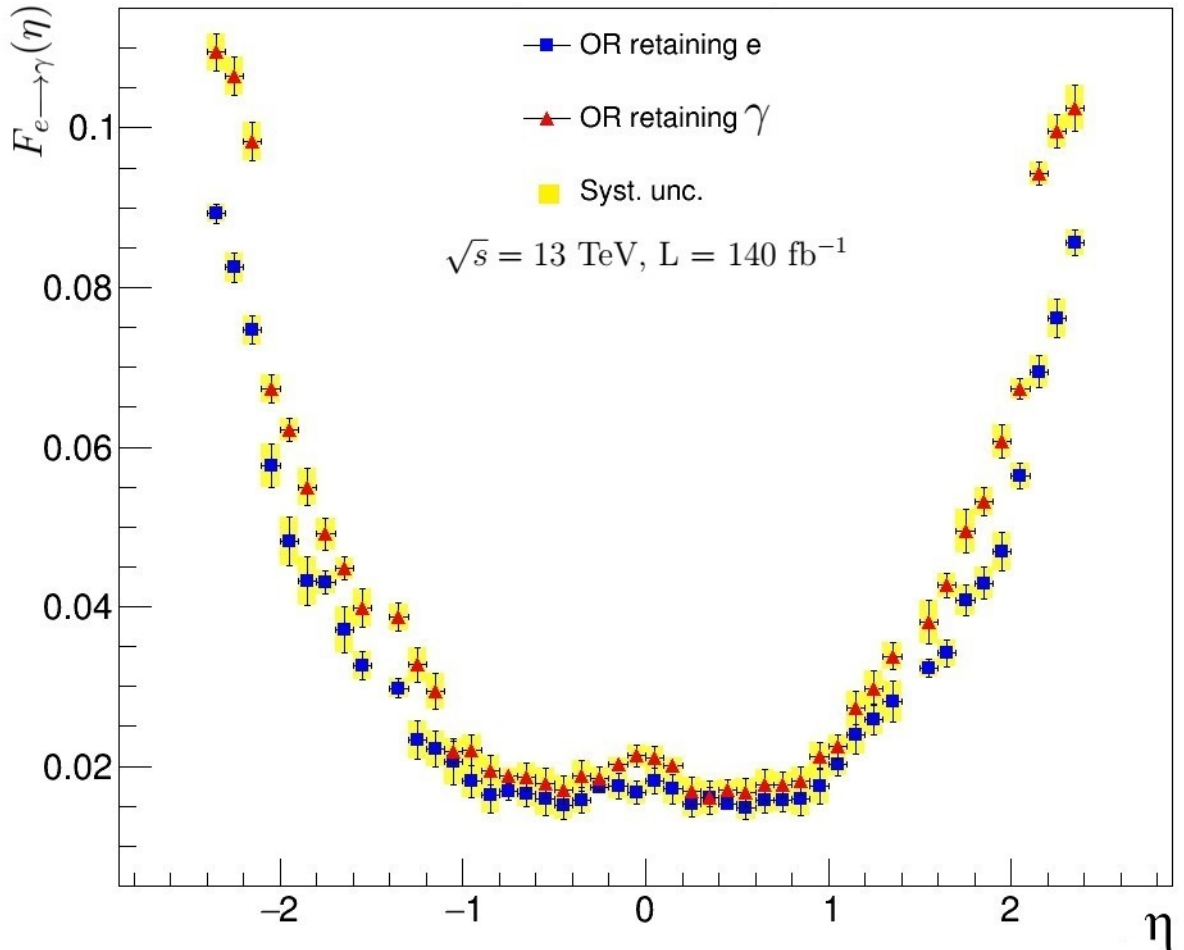


Figure 29: Fake rate as a function of η integrated over p_T for the overlap removal procedure retaining electrons (blue squares) and the overlap removal procedure retaining photons (red triangles). The error bars represent the total uncertainty, while the yellow bands represent the systematic uncertainty.

Table 8: Fake rates for each η bin evaluated from the events selected using the *overlap algorithm favouring electrons*. The table reports the central value, the statistical, the systematic and the total uncertainty. The three components of the systematic uncertainty are shown separately.

η	$F_{e \rightarrow \gamma}$	Stat.	Syst.				Total unc.
			Window	Bkg subtraction	Energy	Total	
[-2.4, -2.3]	0.0893	0.0004	0.0001	0.0010	0.0005	0.0011	0.0012
[-2.3, -2.2]	0.0825	0.0003	0.0003	0.0017	0.0003	0.0018	0.0018
[-2.2, -2.1]	0.0746	0.0002	0.0016	0.0006	0.0007	0.0018	0.0018
[-2.1, -2.0]	0.0577	0.0002	0.0006	0.0016	0.0021	0.0027	0.0028
[-2.0, -1.9]	0.0482	0.0002	0.0014	0.0022	0.0016	0.0031	0.0031
[-1.9, -1.8]	0.0433	0.0002	0.0016	0.0017	0.0020	0.0031	0.0031
[-1.8, -1.7]	0.0431	0.0002	0.0001	0.0014	0.0000	0.0014	0.0014
[-1.7, -1.6]	0.0371	0.0001	0.0002	0.0017	0.0022	0.0028	0.0028
[-1.6, -1.5]	0.0326	0.0002	0.0015	0.0006	0.0007	0.0018	0.0018
[-1.4, -1.3]	0.0298	0.0002	0.0006	0.0007	0.0008	0.0013	0.0013
[-1.3, -1.2]	0.0233	0.0001	0.0012	0.0012	0.0017	0.0024	0.0024
[-1.2, -1.1]	0.0221	0.0001	0.0008	0.0014	0.0016	0.0023	0.0023
[-1.1, -1.0]	0.0206	0.0001	0.0011	0.0017	0.0022	0.0029	0.0029
[-1.0, -0.9]	0.0181	0.0001	0.0008	0.0018	0.0006	0.0020	0.0020
[-0.9, -0.8]	0.0164	0.0001	0.0007	0.0016	0.0015	0.0023	0.0023
[-0.8, -0.7]	0.0168	0.0001	0.0009	0.0002	0.0003	0.0010	0.0010
[-0.7, -0.6]	0.0166	0.0001	0.0008	0.0014	0.0002	0.0016	0.0016
[-0.6, -0.5]	0.0159	0.0001	0.0007	0.0014	0.0012	0.0020	0.0020
[-0.5, -0.4]	0.0150	0.0001	0.0006	0.0014	0.0007	0.0017	0.0017
[-0.4, -0.3]	0.0157	0.0001	0.0007	0.0013	0.0007	0.0017	0.0017
[-0.3, -0.2]	0.0174	0.0001	0.0004	0.0006	0.0002	0.0007	0.0007
[-0.2, -0.1]	0.0175	0.0001	0.0007	0.0013	0.0007	0.0016	0.0016
[-0.1, 0.0]	0.0167	0.0001	0.0005	0.0013	0.0003	0.0014	0.0014
[0.0, 0.1]	0.0182	0.0001	0.0007	0.0014	0.0002	0.0016	0.0016
[0.1, 0.2]	0.0171	0.0001	0.0008	0.0016	0.0000	0.0018	0.0018
[0.2, 0.3]	0.0153	0.0001	0.0006	0.0013	0.0007	0.0016	0.0016
[0.3, 0.4]	0.0161	0.0001	0.0002	0.0012	0.0001	0.0013	0.0013
[0.4, 0.5]	0.0153	0.0001	0.0001	0.0003	0.0004	0.0005	0.0005
[0.5, 0.6]	0.0148	0.0001	0.0007	0.0014	0.0002	0.0016	0.0016
[0.6, 0.7]	0.0157	0.0001	0.0008	0.0013	0.0002	0.0015	0.0015
[0.7, 0.8]	0.0158	0.0001	0.0007	0.0011	0.0007	0.0014	0.0014
[0.8, 0.9]	0.0159	0.0001	0.0007	0.0014	0.0013	0.0020	0.0020
[0.9, 1.0]	0.0176	0.0001	0.0008	0.0016	0.0014	0.0022	0.0022
[1.0, 1.1]	0.0202	0.0001	0.0014	0.0004	0.0002	0.0014	0.0014
[1.1, 1.2]	0.0240	0.0001	0.0016	0.0007	0.0018	0.0025	0.0025
[1.2, 1.3]	0.0258	0.0001	0.0017	0.0010	0.0000	0.0019	0.0020
[1.3, 1.4]	0.0281	0.0002	0.0013	0.0018	0.0014	0.0026	0.0026
[1.5, 1.6]	0.0323	0.0002	0.0009	0.0005	0.0004	0.0011	0.0011
[1.6, 1.7]	0.0342	0.0001	0.0004	0.0016	0.0001	0.0017	0.0017
[1.7, 1.8]	0.0408	0.0002	0.0002	0.0016	0.0010	0.0019	0.0019
[1.8, 1.9]	0.0429	0.0002	0.0001	0.0019	0.0006	0.0020	0.0020
[1.9, 2.0]	0.0469	0.0002	0.0014	0.0017	0.0011	0.0024	0.0024
[2.0, 2.1]	0.0563	0.0002	0.0014	0.0008	0.0002	0.0016	0.0016
[2.1, 2.2]	0.0695	0.0002	0.0002	0.0014	0.0014	0.0020	0.0020
[2.2, 2.3]	0.0761	0.0003	0.0001	0.0019	0.0014	0.0024	0.0024
[2.3, 2.4]	0.0856	0.0004	0.0004	0.0015	0.0002	0.0016	0.0016

Table 9: Fake rates for each η bin evaluated from the events selected using the *overlap algorithm favouring photons*. The table reports the central value, the statistical, the systematic and the total uncertainty. The three components of the systematic uncertainty are shown separately.

η	$F_{e \rightarrow \gamma}$	Stat.	Syst.				Total unc.
			Window	Bkg subtraction	Energy	Total	
[-2.4, -2.3]	0.1095	0.0004	0.0005	0.0017	0.0014	0.0023	0.0023
[-2.3, -2.2]	0.1066	0.0003	0.0004	0.0014	0.0019	0.0024	0.0024
[-2.2, -2.1]	0.0983	0.0003	0.0004	0.0013	0.0019	0.0024	0.0024
[-2.1, -2.0]	0.0673	0.0002	0.0003	0.0012	0.0013	0.0018	0.0018
[-2.0, -1.9]	0.0622	0.0002	0.0003	0.0009	0.0010	0.0014	0.0014
[-1.9, -1.8]	0.0550	0.0002	0.0002	0.0013	0.0019	0.0023	0.0023
[-1.8, -1.7]	0.0491	0.0002	0.0004	0.0011	0.0017	0.0020	0.0020
[-1.7, -1.6]	0.0448	0.0002	0.0007	0.0007	0.0009	0.0014	0.0014
[-1.6, -1.5]	0.0398	0.0002	0.0001	0.0017	0.0018	0.0025	0.0025
[-1.4, -1.3]	0.0387	0.0002	0.0010	0.0009	0.0010	0.0017	0.0017
[-1.3, -1.2]	0.0327	0.0001	0.0006	0.0011	0.0017	0.0022	0.0022
[-1.2, -1.1]	0.0294	0.0001	0.0019	0.0003	0.0012	0.0023	0.0023
[-1.1, -1.0]	0.0218	0.0001	0.0002	0.0012	0.0007	0.0014	0.0014
[-1.0, -0.9]	0.0220	0.0001	0.0010	0.0016	0.0004	0.0019	0.0019
[-0.9, -0.8]	0.0195	0.0001	0.0003	0.0014	0.0011	0.0019	0.0019
[-0.8, -0.7]	0.0188	0.0001	0.0004	0.0001	0.0008	0.0009	0.0009
[-0.7, -0.6]	0.0187	0.0001	0.0008	0.0014	0.0005	0.0017	0.0017
[-0.6, -0.5]	0.0179	0.0001	0.0008	0.0014	0.0009	0.0018	0.0018
[-0.5, -0.4]	0.0170	0.0001	0.0007	0.0013	0.0009	0.0018	0.0018
[-0.4, -0.3]	0.0187	0.0001	0.0012	0.0003	0.0015	0.0019	0.0019
[-0.3, -0.2]	0.0185	0.0001	0.0008	0.0012	0.0003	0.0015	0.0015
[-0.2, -0.1]	0.0203	0.0001	0.0004	0.0007	0.0001	0.0008	0.0008
[-0.1, 0.0]	0.0213	0.0001	0.0008	0.0007	0.0009	0.0014	0.0014
[0.0, 0.1]	0.0211	0.0001	0.0004	0.0008	0.0010	0.0013	0.0013
[0.1, 0.2]	0.0200	0.0001	0.0003	0.0008	0.0004	0.0010	0.0010
[0.2, 0.3]	0.0169	0.0001	0.0011	0.0014	0.0004	0.0018	0.0018
[0.3, 0.4]	0.0160	0.0001	0.0007	0.0013	0.0016	0.0021	0.0021
[0.4, 0.5]	0.0170	0.0001	0.0004	0.0007	0.0010	0.0013	0.0013
[0.5, 0.6]	0.0167	0.0001	0.0007	0.0014	0.0007	0.0017	0.0017
[0.6, 0.7]	0.0176	0.0001	0.0008	0.0014	0.0011	0.0019	0.0019
[0.7, 0.8]	0.0177	0.0001	0.0004	0.0012	0.0010	0.0016	0.0016
[0.8, 0.9]	0.0181	0.0001	0.0008	0.0014	0.0008	0.0018	0.0018
[0.9, 1.0]	0.0212	0.0001	0.0014	0.0005	0.0008	0.0017	0.0017
[1.0, 1.1]	0.0225	0.0001	0.0003	0.0010	0.0011	0.0015	0.0015
[1.1, 1.2]	0.0273	0.0001	0.0018	0.0007	0.0010	0.0021	0.0021
[1.2, 1.3]	0.0298	0.0001	0.0019	0.0010	0.0005	0.0022	0.0022
[1.3, 1.4]	0.0338	0.0002	0.0004	0.0008	0.0014	0.0017	0.0017
[1.5, 1.6]	0.0381	0.0002	0.0017	0.0012	0.0018	0.0027	0.0027
[1.6, 1.7]	0.0427	0.0002	0.0002	0.0015	0.0001	0.0015	0.0015
[1.7, 1.8]	0.0494	0.0002	0.0015	0.0013	0.0019	0.0027	0.0027
[1.8, 1.9]	0.0532	0.0002	0.0002	0.0014	0.0009	0.0017	0.0017
[1.9, 2.0]	0.0608	0.0002	0.0002	0.0016	0.0013	0.0021	0.0021
[2.0, 2.1]	0.0673	0.0002	0.0006	0.0006	0.0009	0.0013	0.0013
[2.1, 2.2]	0.0943	0.0003	0.0003	0.0014	0.0003	0.0014	0.0015
[2.2, 2.3]	0.0996	0.0003	0.0001	0.0018	0.0010	0.0021	0.0021
[2.3, 2.4]	0.1025	0.0004	0.0016	0.0014	0.0019	0.0028	0.0029

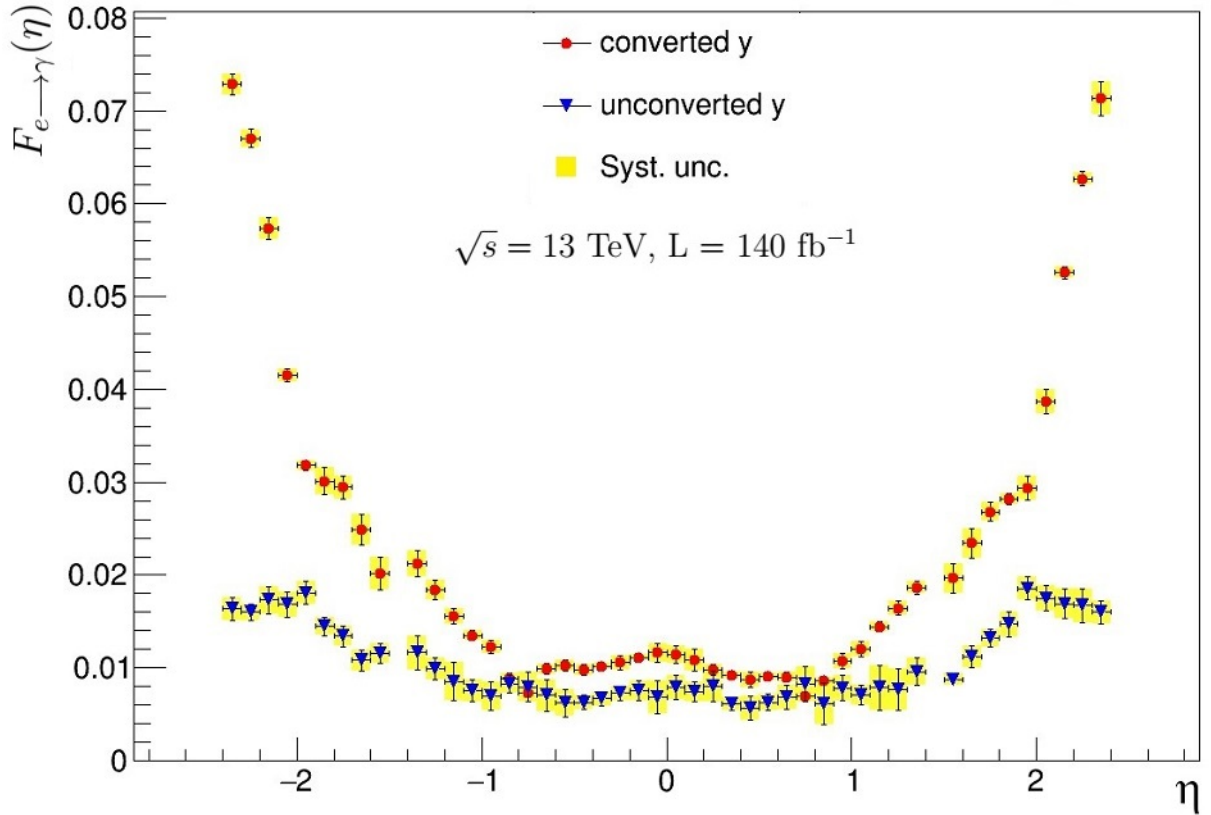


Figure 30: Fake rate as a function of η integrated over p_T for the overlap removal procedure retaining electrons for converted photons (red circles) and unconverted photons (blue triangles). The error bars represent the total uncertainty, while the yellow bands represent the systematic uncertainty.

Table 10: Fake rates for each η bin evaluated for *converted photons* from the events selected using the *overlap algorithm favouring electrons*. The table reports the central value, the statistical, the systematic and the total uncertainty. The three components of the systematic uncertainty are shown separately.

η	$F_{e \rightarrow \gamma}$	Stat.	Syst.				Total unc.
			Window	Bkg substr.	Energy	Total	
[-2.4, -2.3]	0.0729	0.0003	0.0001	0.0003	0.0010	0.0011	0.0011
[-2.3, -2.2]	0.0670	0.0002	0.0002	0.0006	0.0007	0.0009	0.0010
[-2.2, -2.1]	0.0573	0.0002	0.0011	0.0000	0.0004	0.0012	0.0012
[-2.1, -2.0]	0.0416	0.0002	0.0001	0.0005	0.0005	0.0007	0.0007
[-2.0, -1.9]	0.0318	0.0002	0.0001	0.0001	0.0005	0.0005	0.0005
[-1.9, -1.8]	0.0301	0.0001	0.0005	0.0002	0.0014	0.0015	0.0015
[-1.8, -1.7]	0.0294	0.0001	0.0001	0.0003	0.0012	0.0013	0.0013
[-1.7, -1.6]	0.0249	0.0001	0.0005	0.0011	0.0011	0.0016	0.0016
[-1.6, -1.5]	0.0202	0.0001	0.0004	0.0013	0.0012	0.0018	0.0018
[-1.4, -1.3]	0.0212	0.0001	0.0006	0.0012	0.0004	0.0014	0.0014
[-1.3, -1.2]	0.0184	0.0001	0.0004	0.0008	0.0005	0.0010	0.0011
[-1.2, -1.1]	0.0156	0.0001	0.0003	0.0007	0.0002	0.0008	0.0008
[-1.1, -1.0]	0.0135	0.0001	0.0003	0.0004	0.0002	0.0005	0.0005
[-1.0, -0.9]	0.0122	0.0001	0.0003	0.0005	0.0005	0.0007	0.0007
[-0.9, -0.8]	0.0089	0.0001	0.0003	0.0004	0.0003	0.0006	0.0006
[-0.8, -0.7]	0.0073	0.0001	0.0001	0.0001	0.0002	0.0003	0.0003
[-0.7, -0.6]	0.0099	0.0001	0.0005	0.0001	0.0001	0.0006	0.0006
[-0.6, -0.5]	0.0102	0.0001	0.0005	0.0002	0.0001	0.0006	0.0006
[-0.5, -0.4]	0.0098	0.0001	0.0001	0.0002	0.0005	0.0006	0.0006
[-0.4, -0.3]	0.0102	0.0001	0.0001	0.0003	0.0001	0.0003	0.0003
[-0.3, -0.2]	0.0106	0.0001	0.0002	0.0005	0.0006	0.0008	0.0008
[-0.2, -0.1]	0.0111	0.0001	0.0002	0.0003	0.0000	0.0003	0.0003
[-0.1, 0.0]	0.0116	0.0001	0.0001	0.0000	0.0010	0.0010	0.0010
[0.0, 0.1]	0.0114	0.0001	0.0001	0.0000	0.0009	0.0009	0.0009
[0.1, 0.2]	0.0109	0.0001	0.0002	0.0003	0.0011	0.0011	0.0011
[0.2, 0.3]	0.0098	0.0001	0.0001	0.0003	0.0005	0.0006	0.0006
[0.3, 0.4]	0.0092	0.0001	0.0001	0.0003	0.0001	0.0003	0.0003
[0.4, 0.5]	0.0087	0.0001	0.0002	0.0002	0.0007	0.0008	0.0008
[0.5, 0.6]	0.0091	0.0001	0.0002	0.0002	0.0003	0.0004	0.0004
[0.6, 0.7]	0.0090	0.0001	0.0003	0.0003	0.0004	0.0005	0.0005
[0.7, 0.8]	0.0069	0.0001	0.0002	0.0000	0.0002	0.0002	0.0003
[0.8, 0.9]	0.0086	0.0001	0.0001	0.0002	0.0003	0.0004	0.0004
[0.9, 1.0]	0.0107	0.0001	0.0003	0.0008	0.0002	0.0008	0.0008
[1.0, 1.1]	0.0120	0.0001	0.0002	0.0006	0.0005	0.0008	0.0008
[1.1, 1.2]	0.0144	0.0001	0.0003	0.0004	0.0002	0.0006	0.0006
[1.2, 1.3]	0.0164	0.0001	0.0003	0.0006	0.0003	0.0007	0.0008
[1.3, 1.4]	0.0187	0.0001	0.0004	0.0004	0.0004	0.0007	0.0007
[1.5, 1.6]	0.0197	0.0001	0.0001	0.0012	0.0011	0.0016	0.0016
[1.6, 1.7]	0.0234	0.0001	0.0002	0.0011	0.0012	0.0016	0.0016
[1.7, 1.8]	0.0268	0.0001	0.0001	0.0008	0.0006	0.0010	0.0010
[1.8, 1.9]	0.0282	0.0001	0.0001	0.0006	0.0001	0.0006	0.0006
[1.9, 2.0]	0.0294	0.0001	0.0001	0.0001	0.0013	0.0013	0.0013
[2.0, 2.1]	0.0387	0.0002	0.0000	0.0006	0.0012	0.0013	0.0013
[2.1, 2.2]	0.0526	0.0002	0.0001	0.0005	0.0003	0.0006	0.0006
[2.2, 2.3]	0.0627	0.0002	0.0002	0.0003	0.0006	0.0007	0.0007
[2.3, 2.4]	0.0713	0.0003	0.0002	0.0012	0.0013	0.0018	0.0018

Table 11: Fake rates for each η bin evaluated for *unconverted photons* from the events selected using the *overlap algorithm favouring electrons*. The table reports the central value, the statistical, the systematic and the total uncertainty. The three components of the systematic uncertainty are shown separately.

η	$F_{e \rightarrow \gamma}$	Stat.	Syst.				Total unc.
			Window	Bkg substr.	Energy	Total	
[-2.4, -2.3]	0.0163	0.0002	0.0011	0.0006	0.0001	0.0012	0.0012
[-2.3, -2.2]	0.0160	0.0001	0.0002	0.0009	0.0002	0.0009	0.0009
[-2.2, -2.1]	0.0173	0.0001	0.0013	0.0004	0.0005	0.0014	0.0014
[-2.1, -2.0]	0.0168	0.0001	0.0011	0.0008	0.0004	0.0014	0.0014
[-2.0, -1.9]	0.0181	0.0001	0.0010	0.0006	0.0003	0.0012	0.0012
[-1.9, -1.8]	0.0145	0.0001	0.0009	0.0005	0.0002	0.0010	0.0010
[-1.8, -1.7]	0.0134	0.0001	0.0007	0.0005	0.0007	0.0011	0.0011
[-1.7, -1.6]	0.0108	0.0001	0.0001	0.0010	0.0005	0.0011	0.0011
[-1.6, -1.5]	0.0115	0.0001	0.0001	0.0009	0.0005	0.0010	0.0010
[-1.4, -1.3]	0.0116	0.0001	0.0001	0.0011	0.0015	0.0018	0.0018
[-1.3, -1.2]	0.0099	0.0001	0.0002	0.0008	0.0008	0.0012	0.0012
[-1.2, -1.1]	0.0085	0.0001	0.0004	0.0018	0.0008	0.0021	0.0021
[-1.1, -1.0]	0.0076	0.0001	0.0006	0.0010	0.0003	0.0012	0.0012
[-1.0, -0.9]	0.0070	0.0001	0.0007	0.0013	0.0004	0.0015	0.0015
[-0.9, -0.8]	0.0083	0.0001	0.0002	0.0007	0.0006	0.0009	0.0009
[-0.8, -0.7]	0.0080	0.0000	0.0005	0.0014	0.0005	0.0015	0.0016
[-0.7, -0.6]	0.0071	0.0001	0.0005	0.0010	0.0013	0.0017	0.0017
[-0.6, -0.5]	0.0062	0.0000	0.0006	0.0009	0.0010	0.0014	0.0014
[-0.5, -0.4]	0.0063	0.0000	0.0004	0.0007	0.0003	0.0008	0.0008
[-0.4, -0.3]	0.0067	0.0000	0.0004	0.0006	0.0001	0.0008	0.0008
[-0.3, -0.2]	0.0073	0.0001	0.0004	0.0006	0.0001	0.0008	0.0008
[-0.2, -0.1]	0.0075	0.0001	0.0005	0.0006	0.0007	0.0010	0.0010
[-0.1, 0.0]	0.0068	0.0001	0.0008	0.0013	0.0009	0.0018	0.0018
[0.0, 0.1]	0.0079	0.0001	0.0003	0.0008	0.0010	0.0013	0.0013
[0.1, 0.2]	0.0075	0.0001	0.0004	0.0007	0.0007	0.0010	0.0010
[0.2, 0.3]	0.0080	0.0001	0.0006	0.0004	0.0015	0.0017	0.0017
[0.3, 0.4]	0.0061	0.0000	0.0004	0.0006	0.0001	0.0007	0.0007
[0.4, 0.5]	0.0057	0.0000	0.0005	0.0010	0.0006	0.0013	0.0013
[0.5, 0.6]	0.0063	0.0000	0.0004	0.0007	0.0003	0.0009	0.0009
[0.6, 0.7]	0.0068	0.0000	0.0005	0.0010	0.0007	0.0013	0.0013
[0.7, 0.8]	0.0082	0.0001	0.0006	0.0011	0.0014	0.0019	0.0019
[0.8, 0.9]	0.0061	0.0000	0.0004	0.0003	0.0022	0.0022	0.0022
[0.9, 1.0]	0.0078	0.0001	0.0007	0.0001	0.0012	0.0014	0.0014
[1.0, 1.1]	0.0071	0.0001	0.0005	0.0009	0.0003	0.0011	0.0011
[1.1, 1.2]	0.0079	0.0001	0.0010	0.0015	0.0016	0.0024	0.0024
[1.2, 1.3]	0.0077	0.0001	0.0009	0.0017	0.0012	0.0023	0.0023
[1.3, 1.4]	0.0096	0.0001	0.0008	0.0012	0.0004	0.0015	0.0015
[1.5, 1.6]	0.0088	0.0001	0.0005	0.0003	0.0002	0.0007	0.0007
[1.6, 1.7]	0.0112	0.0001	0.0004	0.0004	0.0010	0.0012	0.0012
[1.7, 1.8]	0.0132	0.0001	0.0007	0.0005	0.0005	0.0010	0.0010
[1.8, 1.9]	0.0147	0.0001	0.0008	0.0006	0.0008	0.0013	0.0013
[1.9, 2.0]	0.0186	0.0001	0.0011	0.0006	0.0003	0.0012	0.0013
[2.0, 2.1]	0.0175	0.0001	0.0011	0.0007	0.0004	0.0013	0.0014
[2.1, 2.2]	0.0169	0.0001	0.0011	0.0007	0.0009	0.0016	0.0016
[2.2, 2.3]	0.0167	0.0001	0.0006	0.0006	0.0016	0.0018	0.0018
[2.3, 2.4]	0.0160	0.0002	0.0007	0.0005	0.0009	0.0012	0.0013

Fake rate as a function of $|\eta|$ and p_T

The electron-to-photon fake rate as a function of $|\eta|$ and p_T is reported in Figure 31 for the overlap removal procedure retaining electrons and in Figure 32 for the overlap removal procedure retaining photons. Both the systematic (colored bands) and total (error bars) uncertainties are highlighted: the total uncertainty is always dominated by the systematic component. The corresponding measured values are reported in Tables from 12 to 24:

- for the OR retaining electrons, the e-to- γ fake rate is approximately 2% for the $0 < |\eta| < 0.8$, reaching about 8 – 9% for $2.01 < |\eta| < 2.37$. The total uncertainty is approximately 10% of the fake rate in the central region ($0 < |\eta| < 0.8$) and it decreases to about 5-6% in the external region ($2.01 < |\eta| < 2.37$);
- for the OR retaining photons, the e-to- γ fake rate is approximately 2.1% for η close to 0 reaching about 10.5% for $\eta \sim \pm 2.4$. The total uncertainty is approximately 6-10% of the fake rate in the central region ($0 < |\eta| < 0.8$) and it decreases to about 4-6% in the external region ($2.01 < |\eta| < 2.37$).

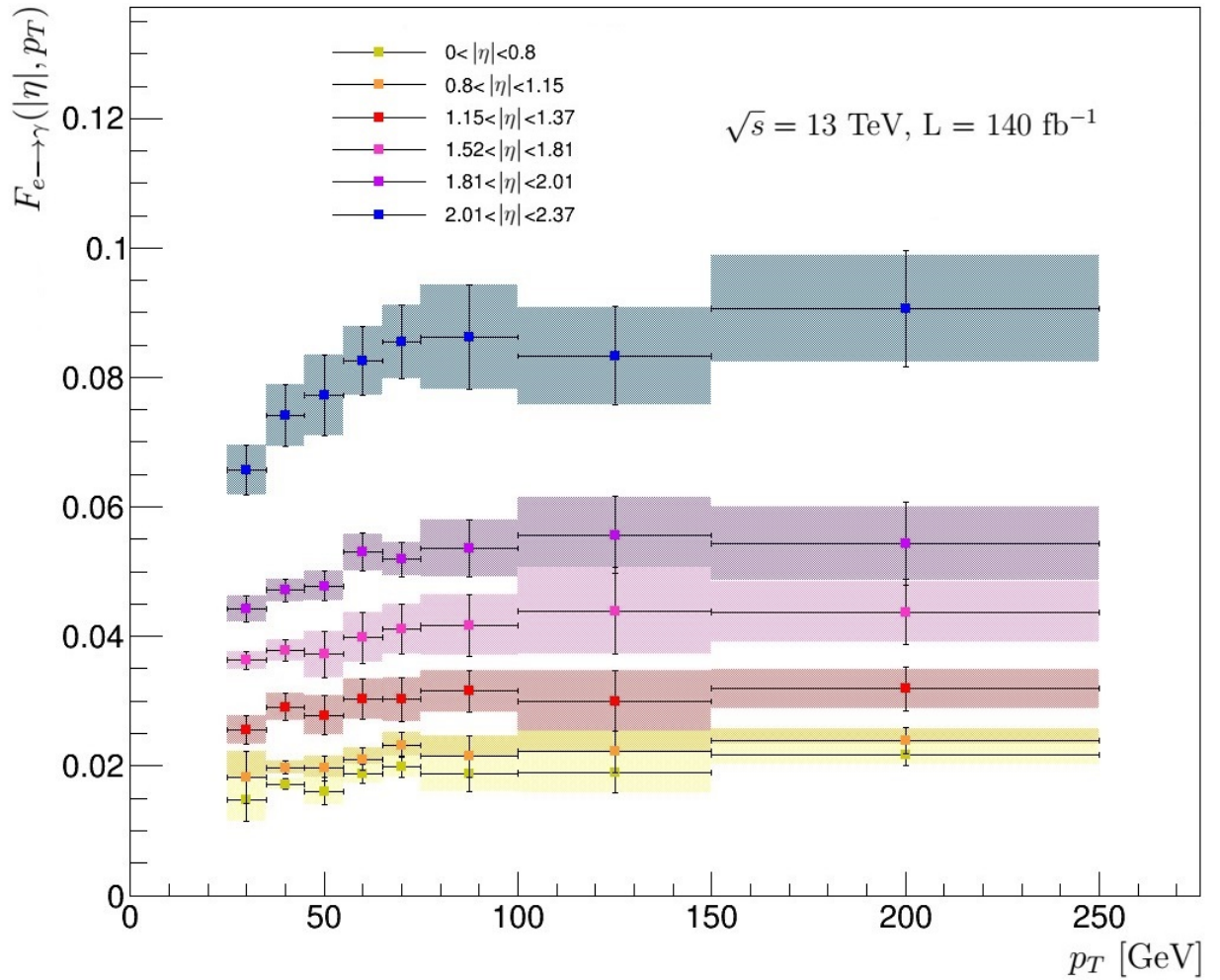


Figure 31: Fake rate as a function of p_T in different η bins for the *overlap removal procedure retaining electrons*. The error bars represent the total uncertainty, while the colored bands represent the systematic uncertainty for each bin.

Table 12: Fake rates for the $0 \leq \eta \leq 0.8$ bin for $25 \leq p_T \leq 250$ evaluated from the events selected using the *overlap algorithm favouring electrons*. The table reports the central value, the statistical, the systematic and the total uncertainty.

$0 \leq \eta \leq 0.8$

p_T [GeV]	$F_{e \rightarrow \gamma}$	Stat.	Syst.				Total unc.
			Window	Bkg subtraction	Energy	Total	
[25, 35]	0.0147	0.0000	0.0016	0.0025	0.0015	0.0033	0.0033
[35, 45]	0.0172	0.0000	0.0003	0.0003	0.0007	0.0008	0.0008
[45, 55]	0.0161	0.0000	0.0004	0.0014	0.0015	0.0021	0.0021
[55, 65]	0.0188	0.0001	0.0007	0.0007	0.0010	0.0014	0.0014
[65, 75]	0.0199	0.0001	0.0007	0.0008	0.0014	0.0017	0.0017
[75, 100]	0.0188	0.0002	0.0001	0.0022	0.0016	0.0027	0.0027
[100, 150]	0.0190	0.0003	0.0003	0.0029	0.0012	0.0031	0.0032
[150, 250]	0.0217	0.0006	0.0012	0.0002	0.0010	0.0016	0.0017

Table 13: Fake rates for the $0.8 \leq \eta \leq 1.15$ bin for $25 \leq p_T \leq 250$ evaluated from the events selected using the *overlap algorithm favouring electrons*. The table reports the central value, the statistical, the systematic and the total uncertainty.

$0.8 \leq \eta \leq 1.15$

p_T [GeV]	$F_{e \rightarrow \gamma}$	Stat.	Syst.				Total unc.
			Window	Bkg subtraction	Energy	Total	
[25, 35]	0.0183	0.0001	0.0016	0.0015	0.0033	0.0040	0.0040
[35, 45]	0.0198	0.0000	0.0004	0.0008	0.0005	0.0010	0.0010
[45, 55]	0.0196	0.0001	0.0005	0.0006	0.0018	0.0019	0.0019
[55, 65]	0.0211	0.0001	0.0000	0.0014	0.0010	0.0017	0.0017
[65, 75]	0.0233	0.0003	0.0005	0.0010	0.0015	0.0019	0.0019
[75, 100]	0.0215	0.0003	0.0001	0.0026	0.0019	0.0032	0.0032
[100, 150]	0.0223	0.0005	0.0003	0.0029	0.0013	0.0032	0.0032
[150, 250]	0.0240	0.0010	0.0012	0.0003	0.0013	0.0018	0.0020

Table 14: Fake rates for the $1.15 \leq \eta \leq 1.37$ bin for $25 \leq p_T \leq 250$ evaluated from the events selected using the *overlap algorithm favouring electrons*. The table reports the central value, the statistical, the systematic and the total uncertainty.

$1.15 \leq \eta \leq 1.37$

p_T [GeV]	$F_{e \rightarrow \gamma}$	Stat.	Syst.				Total unc.
			Window	Bkg subtraction	Energy	Total	
[25, 35]	0.0256	0.0001	0.0007	0.0008	0.0019	0.0022	0.0022
[35, 45]	0.0291	0.0001	0.0009	0.0008	0.0017	0.0021	0.0021
[45, 55]	0.0278	0.0001	0.0004	0.0009	0.0029	0.0031	0.0031
[55, 65]	0.0303	0.0002	0.0008	0.0010	0.0028	0.0031	0.0031
[65, 75]	0.0303	0.0004	0.0007	0.0016	0.0029	0.0034	0.0034
[75, 100]	0.0315	0.0005	0.0010	0.0020	0.0023	0.0032	0.0033
[100, 150]	0.0301	0.0002	0.0000	0.0034	0.0031	0.0046	0.0046
[150, 250]	0.0319	0.0015	0.0002	0.0023	0.0020	0.0030	0.0034

Table 15: Fake rates for the $1.52 \leq \eta \leq 1.81$ bin for $25 \leq p_T \leq 250$ evaluated from the events selected using the *overlap algorithm favouring electrons*. The table reports the central value, the statistical, the systematic and the total uncertainty.

$1.52 \leq \eta \leq 1.81$

p_T [GeV]	$F_{e \rightarrow \gamma}$	Stat.	Syst.				Total unc.
			Window	Bkg subtraction	Energy	Total	
[25, 35]	0.0363	0.0001	0.0005	0.0008	0.0009	0.0013	0.0013
[35, 45]	0.0379	0.0001	0.0001	0.0008	0.0014	0.0017	0.0017
[45, 55]	0.0372	0.0001	0.0005	0.0002	0.0035	0.0035	0.0035
[55, 65]	0.0398	0.0003	0.0003	0.0013	0.0036	0.0039	0.0039
[65, 75]	0.0411	0.0002	0.0000	0.0001	0.0038	0.0038	0.0038
[75, 100]	0.0418	0.0005	0.0007	0.0020	0.0042	0.0047	0.0047
[100, 150]	0.0439	0.0009	0.0002	0.0033	0.0058	0.0066	0.0067
[150, 250]	0.0437	0.0018	0.0005	0.0040	0.0025	0.0047	0.0050

Table 16: Fake rates for the $1.81 \leq \eta \leq 2.01$ bin for $25 \leq p_T \leq 250$ evaluated from the events selected using the *overlap algorithm favouring electrons*. The table reports the central value, the statistical, the systematic and the total uncertainty.

$1.81 \leq \eta \leq 2.01$

p_T [GeV]	$F_{e \rightarrow \gamma}$	Stat.	Syst.				Total unc.
			Window	Bkg subtraction	Energy	Total	
[25, 35]	0.0443	0.0002	0.0002	0.0003	0.0019	0.0020	0.0020
[35, 45]	0.0471	0.0001	0.0001	0.0004	0.0017	0.0017	0.0017
[45, 55]	0.0477	0.0002	0.0003	0.0002	0.0023	0.0023	0.0023
[55, 65]	0.0530	0.0004	0.0012	0.0012	0.0023	0.0029	0.0029
[65, 75]	0.0519	0.0007	0.0003	0.0003	0.0025	0.0026	0.0026
[75, 100]	0.0536	0.0008	0.0008	0.0016	0.0039	0.0043	0.0044
[100, 150]	0.0556	0.0015	0.0005	0.0028	0.0050	0.0057	0.0059
[150, 250]	0.0543	0.0029	0.0011	0.0022	0.0051	0.0057	0.0064

Table 17: Fake rates for the $2.01 \leq \eta \leq 2.37$ bin for $25 \leq p_T \leq 250$ evaluated from the events selected using the *overlap algorithm favouring electrons*. The table reports the central value, the statistical, the systematic and the total uncertainty.

$2.01 \leq \eta \leq 2.37$

p_T [GeV]	$F_{e \rightarrow \gamma}$	Stat.	Syst.				Total unc.
			Window	Bkg subtraction	Energy	Total	
[25, 35]	0.0657	0.0002	0.0026	0.0005	0.0028	0.0038	0.0039
[35, 45]	0.0741	0.0001	0.0033	0.0005	0.0035	0.0048	0.0048
[45, 55]	0.0772	0.0002	0.0048	0.0004	0.0039	0.0062	0.0062
[55, 65]	0.0826	0.0005	0.0026	0.0003	0.0046	0.0053	0.0053
[65, 75]	0.0855	0.0008	0.0027	0.0004	0.0050	0.0057	0.0057
[75, 100]	0.0862	0.0009	0.0059	0.0028	0.0047	0.0080	0.0081
[100, 150]	0.0833	0.0016	0.0050	72 0.0025	0.0050	0.0075	0.0077
[150, 250]	0.0906	0.0035	0.0051	0.0027	0.0060	0.0083	0.0090

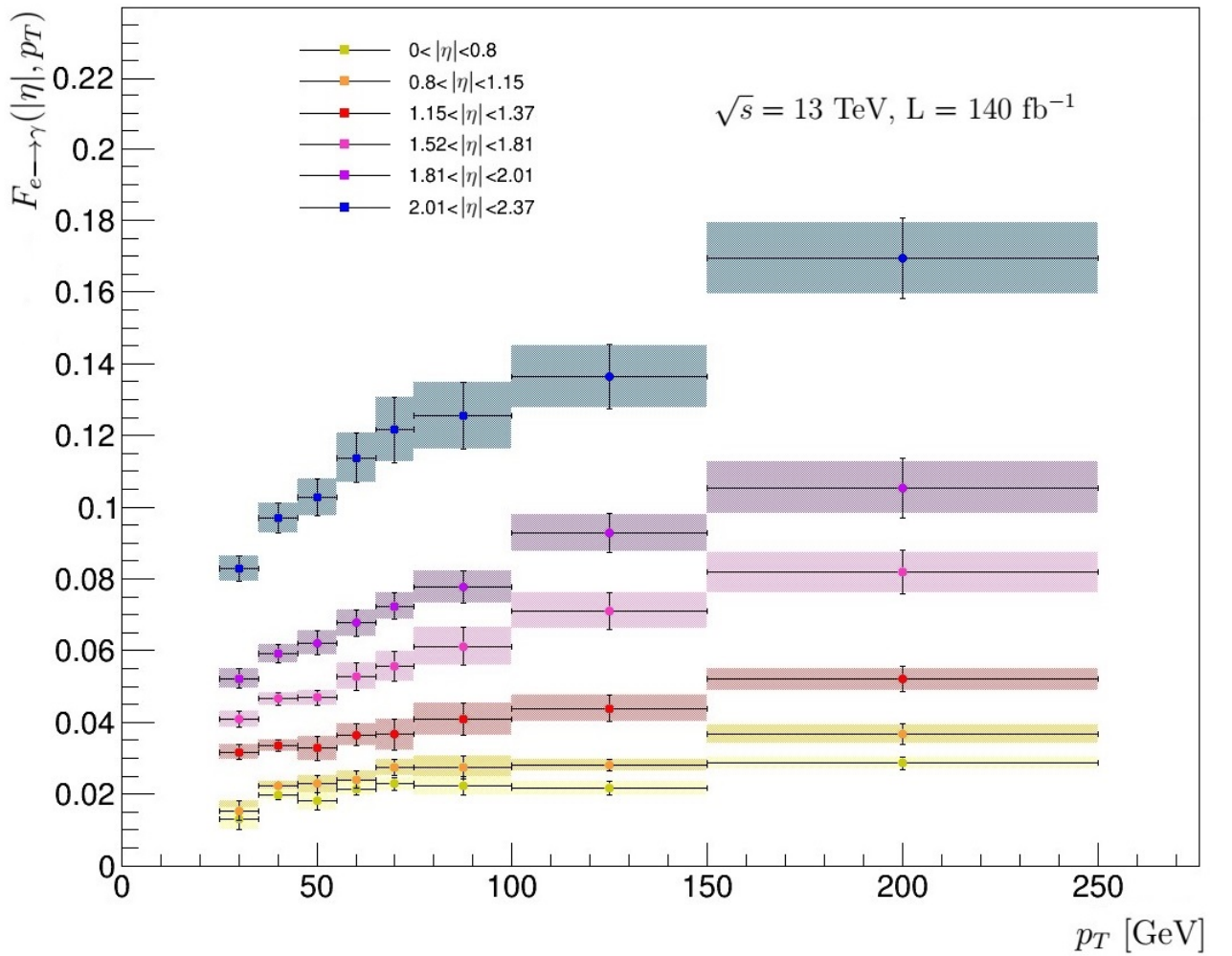


Figure 32: Fake rate as a function of p_T in different η bins for the *overlap removal procedure retaining photons*. The error bars represent the total uncertainty, while the colored bands represent the systematic uncertainty for each bin.

Table 18: Fake rates for the $0 \leq \eta \leq 0.8$ bin for $25 \leq p_T \leq 250$ evaluated from the events selected using the *overlap algorithm favouring photons*. The table reports the central value, the statistical, the systematic and the total uncertainty.

p_T [GeV]	$F_{e \rightarrow \gamma}$	Stat.	Syst.				Total unc.
			Window	Bkg subtraction	Energy	Total	
[25, 35]	0.0131	0.0000	0.0024	0.0012	0.0016	0.0031	0.0031
[35, 45]	0.0199	0.0000	0.0008	0.0007	0.0010	0.0015	0.0015
[45, 55]	0.0180	0.0000	0.0004	0.0017	0.0017	0.0024	0.0024
[55, 65]	0.0215	0.0001	0.0006	0.0006	0.0016	0.0018	0.0018
[65, 75]	0.0228	0.0002	0.0004	0.0007	0.0015	0.0017	0.0017
[75, 100]	0.0223	0.0002	0.0001	0.0015	0.0022	0.0026	0.0026
[100, 150]	0.0216	0.0003	0.0009	0.0014	0.0012	0.0020	0.0020
[150, 250]	0.0286	0.0007	0.0011	0.0004	0.0011	0.0016	0.0018

Table 19: Fake rates for the $0.8 \leq \eta \leq 1.15$ bin for $25 \leq p_T \leq 250$ evaluated from the events selected using the *overlap algorithm favouring photons*. The table reports the central value, the statistical, the systematic and the total uncertainty.

p_T [GeV]	$F_{e \rightarrow \gamma}$	Stat.	Syst.				Total unc.
			Window	Bkg subtraction	Energy	Total	
[25, 35]	0.0154	0.0001	0.0016	0.0018	0.0011	0.0027	0.0027
[35, 45]	0.0224	0.0001	0.0004	0.0008	0.0008	0.0012	0.0012
[45, 55]	0.0228	0.0001	0.0009	0.0006	0.0022	0.0024	0.0024
[55, 65]	0.0241	0.0001	0.0007	0.0011	0.0022	0.0025	0.0025
[65, 75]	0.0275	0.0003	0.0007	0.0012	0.0019	0.0023	0.0023
[75, 100]	0.0274	0.0003	0.0007	0.0020	0.0023	0.0031	0.0031
[100, 150]	0.0281	0.0006	0.0010	0.0006	0.0010	0.0015	0.0016
[150, 250]	0.0367	0.0012	0.0012	0.0002	0.0022	0.0025	0.0028

Table 20: Fake rates for the $1.15 \leq \eta \leq 1.37$ bin for $25 \leq p_T \leq 250$ evaluated from the events selected using the *overlap algorithm favouring photons*. The table reports the central value, the statistical, the systematic and the total uncertainty.

p_T [GeV]	$F_{e \rightarrow \gamma}$	Stat.	Syst.				Total unc.
			Window	Bkg subtraction	Energy	Total	
[25, 35]	0.0318	0.0001	0.0010	0.0012	0.0012	0.0020	0.0020
[35, 45]	0.0335	0.0001	0.0009	0.0007	0.0011	0.0016	0.0016
[45, 55]	0.0328	0.0001	0.0004	0.0007	0.0032	0.0033	0.0033
[55, 65]	0.0366	0.0003	0.0007	0.0010	0.0028	0.0031	0.0031
[65, 75]	0.0366	0.0004	0.0015	0.0027	0.0031	0.0043	0.0044
[75, 100]	0.0409	0.0006	0.0011	0.0021	0.0037	0.0044	0.0045
[100, 150]	0.0439	0.0010	0.0003	0.0025	0.0026	0.0037	0.0038
[150, 250]	0.0521	0.0020	0.0006	0.0018	0.0024	0.0031	0.0036

Table 21: Fake rates for the $1.52 \leq \eta \leq 1.81$ bin for $25 \leq p_T \leq 250$ evaluated from the events selected using the *overlap algorithm favouring photons*. The table reports the central value, the statistical, the systematic and the total uncertainty.

$1.52 \leq \eta \leq 1.81$

p_T [GeV]	$F_{e \rightarrow \gamma}$	Stat.	Syst.				Total unc.
			Window	Bkg subtraction	Energy	Total	
[25, 35]	0.0409	0.0001	0.0009	0.0016	0.0012	0.0022	0.0022
[35, 45]	0.0465	0.0001	0.0006	0.0004	0.0016	0.0017	0.0017
[45, 55]	0.0469	0.0001	0.0002	0.0004	0.0021	0.0021	0.0021
[55, 65]	0.0528	0.0003	0.0002	0.0005	0.0037	0.0037	0.0037
[65, 75]	0.0557	0.0005	0.0005	0.0013	0.0039	0.0041	0.0042
[75, 100]	0.0612	0.0007	0.0007	0.0019	0.0048	0.0052	0.0053
[100, 150]	0.0711	0.0013	0.0007	0.0030	0.0038	0.0049	0.0051
[150, 250]	0.0818	0.0026	0.0014	0.0016	0.0051	0.0055	0.0061

Table 22: Fake rates for the $1.81 \leq \eta \leq 2.01$ bin for $25 \leq p_T \leq 250$ evaluated from the events selected using the *overlap algorithm favouring photons*. The table reports the central value, the statistical, the systematic and the total uncertainty.

$1.81 \leq \eta \leq 2.01$

p_T [GeV]	$F_{e \rightarrow \gamma}$	Stat.	Syst.				Total unc.
			Window	Bkg subtraction	Energy	Total	
[25, 35]	0.0522	0.0002	0.0002	0.0004	0.0027	0.0027	0.0027
[35, 45]	0.0592	0.0002	0.0008	0.0000	0.0024	0.0025	0.0025
[45, 55]	0.0622	0.0002	0.0009	0.0012	0.0029	0.0033	0.0033
[55, 65]	0.0677	0.0005	0.0005	0.0012	0.0035	0.0038	0.0038
[65, 75]	0.0724	0.0008	0.0002	0.0004	0.0036	0.0036	0.0037
[75, 100]	0.0778	0.0010	0.0005	0.0022	0.0038	0.0044	0.0045
[100, 150]	0.0928	0.0020	0.0020	0.0024	0.0041	0.0052	0.0056
[150, 250]	0.1054	0.0043	0.0011	0.0025	0.0067	0.0072	0.0084

Table 23: Fake rates for the $2.01 \leq \eta \leq 2.37$ bin for $25 \leq p_T \leq 250$ evaluated from the events selected using the *overlap algorithm favouring photons*. The table reports the central value, the statistical, the systematic and the total uncertainty.

$2.01 \leq \eta \leq 2.37$

p_T [GeV]	$F_{e \rightarrow \gamma}$	Stat.	Syst.				Total unc.
			Window	Bkg subtraction	Energy	Total	
[25, 35]	0.0829	0.0002	0.0007	0.0003	0.0034	0.0035	0.0035
[35, 45]	0.0969	0.0002	0.0009	0.0020	0.0035	0.0041	0.0041
[45, 55]	0.1026	0.0002	0.0003	0.0001	0.0051	0.0052	0.0052
[55, 65]	0.1138	0.0006	0.0005	0.0009	0.0068	0.0069	0.0069
[65, 75]	0.1216	0.0010	0.0007	0.0019	0.0088	0.0090	0.0091
[75, 100]	0.1254	0.0009	0.0013	0.0020	0.0089	0.0092	0.0093
[100, 150]	0.1363	0.0022	0.0010	75 0.0029	0.0081	0.0087	0.0089
[150, 250]	0.1694	0.0052	0.0018	0.0038	0.0090	0.0100	0.0112

5.2 Background from electrons faking photons

After measuring the electron-to-photon fake rate, the number of electron fakes in each region of the analysis was estimated. For each region of the analysis an additional Control Region, called Probe-electron Control Region, is defined: the probe-e CR is defined in the same way as the corresponding CR of the analysis, except that the requirements for the leading photon are replaced with a request to have an electron. The electrons need to satisfy the same criteria used for the fake rate measurement (probe electrons): they need to meet the preselection classification of the Mono-Photon analysis (see Section 4.2.2); the transverse momentum is required to be larger than 25 GeV and $|\eta| < 1.37$ or $1.52 < |\eta| < 2.37$; finally, they need to be isolated: electrons are required to be selected by the *Loose* isolation working point and photons need to fit in the *FixedCutTight* isolation working point. The event yield in each probe-e CR is then rescaled with the fake rate values, depending on $|\eta|$ and p_T of the selected probe electrons. The result is the estimation of electrons faking photons in each region of the analysis. The number of electron fakes was estimated using the electron-to-photon fake rate measurements reported in Tables from 12 to 17. The results for every inclusive region of the analysis for the three thresholds on E_T^{miss} (150 GeV, 225 GeV, and 300 GeV) are shown in Tables 24, 25, and 26 using 36.1 fb^{-1} of data collected in 2015-2016. The nominal value of the background yields from electrons faking photons is reported, with its three uncertainties. The first source of uncertainty for the number of electron fakes is the number of events selected in the probe-e CRs, while the second and the third are the statistic and systematic uncertainties related to the measurement of the electron-to-photon fake rate. The yields of electron fakes are consistently larger than the corresponding results obtained for the Mono-Photon analysis in 2016 [24].

The major contribution to the total uncertainty in the three SRs is the systematic uncertainty related to the electron-to-photon fake rate.

Table 24: Number of electrons faking photons estimated in the SR and its CRs for the lower threshold of E_T^{miss} , i.e. $E_T^{miss} > 150$ GeV. The uncertainty is expressed in three terms: the first term is the statistical uncertainty related to the number of events found in the probe-e CR; the second and third terms are the statistical and systematic uncertainties related to the electron fake rate, respectively. The total uncertainty, calculated as the combination of the three uncertainties listed above, is also shown.

$$E_T^{miss} \geq 150 \text{ GeV}$$

	Electron fakes	Stat. for number of events in probe-e CR	Stat. for fake rate	Syst. for fake rate	Total unc.
SR	604	5.2	22.2	52.2	57.0
1 μ CR	44.45	1.36	1.59	3.80	4.34
2 μ CR	1.28	0.22	0.04	0.11	0.25
2e CR	0.19	0.11	0.01	0.02	0.11
PhJet CR	191.34	2.98	7.06	16.56	18.25

Table 25: Number of electrons faking photons estimated in the SR and its CRs for the middle threshold of E_T^{miss} , i.e. $E_T^{miss} > 225$ GeV. The uncertainty is expressed in three terms: the first term is the statistical uncertainty related to the number of events found in the probe-e CR; the second and third terms are the statistical and systematic uncertainties related to the electron fake rate, respectively. The total uncertainty, calculated as the combination of the three uncertainties listed above, is also shown.

$$E_T^{miss} \geq 225 \text{ GeV}$$

	Electron fakes	Stat. for number of events in probe-e CR	Stat. for fake rate	Syst. for fake rate	Total unc.
SR	148.6	2.5	5.3	12.7	14.0
1 μ CR	11.09	0.65	0.38	0.93	1.20
2 μ CR	0.36	0.10	0.01	0.03	0.10
2e CR	0.11	0.09	0.00	0.01	0.091
PhJet CR	191.34	2.98	7.06	16.56	18.25

Table 26: Number of electrons faking photons estimated in the SR and its CRs for the middle threshold of E_T^{miss} , i.e. $E_T^{miss} > 300$ GeV. The uncertainty is expressed in three terms: the first term is the statistical uncertainty related to the number of events found in the probe-e CR; the second and third terms are the statistical and systematic uncertainties related to the electron fake rate, respectively. The total uncertainty, calculated as the combination of the three uncertainties listed above, is also shown.

$$E_T^{miss} \geq 300 \text{ GeV}$$

	Electron fakes	Stat. for number of events in probe-e CR	Stat. for fake rate	Syst. for fake rate	Total unc.
SR	44.6	1.3	1.5	3.7	4.2
1 μ CR	2.67	0.31	0.09	0.22	0.39
2 μ CR	0.13	0.06	0.00	0.01	0.061
2e CR	0.09	0.09	0.00	0.01	0.091
PhJet CR	191.34	2.98	7.06	16.56	18.25

6 Conclusions

An estimation of the background yield from electrons faking photons for the Mono-Photon analysis was performed. To determine the number of such electron fakes, a two-step approach was employed. The first step consists in evaluating the *electron-to-photon fake rate* that can be seen as the probability for true electrons to be mistakenly reconstructed and identified as photons. The measurement of the fake rate is performed selecting $Z \rightarrow ee$ decays, where the two electrons in the final state can be reconstructed either as a ee or as a $e\gamma$ couple, where the γ is a fake photon. The ratio of reconstructed $e\gamma$ yields to reconstructed ee yields provides an estimation of the electron-to-photon fake rate. The e -to- γ fake rate is measured as a function of the pseudorapidity η in the range (-2.37, 2.37) and as a function of the transverse momentum p_T in different $|\eta|$ intervals (0-0.8-1.15-1.37, 1.52-1.81-2.01-2.37) where the transverse momentum values lie between 25 GeV and 250 GeV. The fake rate for the Mono-Photon selection as a function of η , $F_{e \rightarrow \gamma}(\eta)$, was found to increase with the absolute value of η : for $|\eta|$ close to 0, $F_{e \rightarrow \gamma}(\eta) \sim 2\%$, reaching approximately 9% for $\eta \sim \pm 2.4$. On the other hand, the fake rate as a function of $|\eta|$ and p_T , $F_{e \rightarrow \gamma}(|\eta|, p_T)$, is approximately constant as a function of the transverse momentum for every $|\eta|$ bin, with a slight tendency to increase with increasing p_T . Three main sources of systematic uncertainty on the measure of the e -to- γ fake rate were identified and their contribution to the total uncertainty was evaluated. The three identified sources are: the mass range used to select $e\gamma$ and ee yields from the Z boson mass spectra, the jet background subtraction and the bias in the calibration of the energy of the fake photon in $e\gamma$ final states. The total uncertainty varies approximately from 1% to 10% of the e -to- γ fake rate and it is always dominated by the systematic component.

The second step consists in using the e -to- γ fake rate to compute the number of electron fakes for every region of the Mono-Photon analysis. For each region of the analysis an additional CR, the probe-electron CR, is defined: the probe-e CR is defined in the same way as the corresponding CR of the analysis, except that the requirements on the photon are replaced with a request to have an electron. The yield of electron fakes in each region of the analysis is the event yield in the corresponding probe-e CR rescaled with the e -to- γ fake rate. As a cross-check, the electrons faking photons contributions reported in the published 2015-2016 analysis [24] have been compared with the results obtained from the work presented in this thesis on the same dataset: the updated numbers are consistently larger than the numbers obtained in the Mono-Photon analysis performed in 2015 and 2016. The number of electron fakes in the inclusive SR ($E_T^{miss} > 150$ GeV) is 604 ± 57 , which gives a doubled contribution to the total background with respect to the published analysis. This large difference is mostly attributed to changes in the identification procedure for electrons in the new data reconstruction: updated estimations of the e -to- γ contributions in all analysis regions using full Run 2 dataset (140 fb^{-1}) have been performed. The new analysis on the full Run 2 dataset is still ongoing and final results are expected by spring 2020.

Ringraziamenti

Vorrei innanzitutto ringraziare i miei supervisori Leonardo Carminati, Stefano Manzoni e Silvia Resconi per la loro presenza costante, per avermi mostrato con il loro esempio cosa vogliono dire professionalità, competenza e per avermi insegnato a dedicarmi con impegno e passione al mio lavoro. Vorrei anche ringraziare Donatella Cavalli e Miguel Villaplana per i loro preziosi consigli. Un grazie speciale alla mia famiglia senza il cui supporto non ce l'avrei fatta. Grazie ai miei grandi amici Laura, Nico, Giulia, Alberto per essermi stati sempre vicini, pronti ad aiutarmi, ad ascoltare i miei dispiaceri e ad accettare i miei "scusate non posso, devo studiare"; il vostro sostegno è impagabile. Ringrazio i miei amici Andrea, Denise, Eleonora, Giovanni, Irene, Marcello, Rebecca e tutti quelli con cui ho condiviso questo percorso: condividere con voi le emozioni, le risate e le fatiche è stata una vera fonte di sollievo. Un grazie speciale a Federica: la tua presenza in auletta è stata una grande fonte di consolazione, senza il tuo prezioso aiuto sarei probabilmente impazzita. Grazie alle mie amiche storiche Noghina, Alessia, Sara e Giulia. Per ultima vorrei ringraziare di cuore una persona che è impossibile inquadrare in qualcuna di queste categorie perché in qualche modo lei fa parte di tutte: grazie Lili.

References

- [1] Lyndon Evans and Philip Bryant. “LHC Machine”. In: *Journal of Instrumentation* 3 (2008). <http://stacks.iop.org/1748-0221/3/i=08/a=S08001>.
- [2] Luminosity Public Results Run2. https://twiki.cern.ch/twiki/bin/view/AtlasPublic/LuminosityPublicResultsRun2#Luminosity_summary_plots_for_AN3.
- [3] The ATLAS Collaboration, G. Aad et al., “The ATLAS Experiment at the CERN Large Hadron Collider”. In: *Journal of Instrumentation* 3 (2008), S08003. [10.1088/1748-0221/3/08/S08003](https://doi.org/10.1088/1748-0221/3/08/S08003).
- [4] C.W. Fabjan and F. Gianotti, “Calorimetry for particle physics”. In: *Review of Modern Physics* 75(4). <https://doi.org/10.1103/RevModPhys.75.1243>. *Rev. Mod. Phys.* 751243.
- [5] ATLAS Collaboration. “Performance of the ATLAS trigger system in 2015”. In: *The European Physical Journal C* 77.5 (May 2017). [10.1140/epjc/s10052-017-4852-3](https://doi.org/10.1140/epjc/s10052-017-4852-3).
- [6] ATLAS Collaboration. “Observation of a new particle in the search for the Standard Model Higgs boson with the ATLAS detector at the LHC”. In: *Physics Letters B* 716.1 (2012), pp. 1–29. [10.1016/j.physletb.2012.08.020](https://doi.org/10.1016/j.physletb.2012.08.020).
- [7] CMS Collaboration. “Observation of a new boson at a mass of 125 GeV with the CMS experiment at the LHC”. In: *Physics Letters B* 716.1 (2012), pp. 30–61. [10.1016/j.physletb.2012.08.021](https://doi.org/10.1016/j.physletb.2012.08.021).
- [8] Jalal Abdallah et al. *Simplified models for Dark Matter searches at the LHC*. 2015. <https://doi.org/10.1016/j.dark.2015.08.001>.
- [9] Planck collaboration: P.A.R. Ade et al. *Planck 2013 results. I. Overview of products and scientific results*. 2014. <https://arxiv.org/abs/1303.5062>.
- [10] R. Bernabei et al. *The Dark Matter annual modulation results from DAMA/LIBRA*. 2014. <https://doi.org/10.1051/epjconf/20147000043>.
- [11] CMS Collaboration, S. Chatrchyan et al., The CMS experiment at the CERN LHC, *JINST* 3 (2008) S08004. <https://doi.org/10.1088/1748-0221/3/08/S08004>.
- [12] LHCb collaboration A Large Hadron Collider beauty experiment, Technical Proposal, CERN-LHCC-98-004, <http://cdsweb.cern.ch/record/622031>.
- [13] ALICE collaboration Technical proposal for A Large Ion Collider Experiment at the CERN LHC, CERN-LHCC-95-71, <http://cdsweb.cern.ch/record/293391>.

- [14] MoEDAL Collaboration, The MoEDAL experiment at the LHC. Searching beyond the standard model, EPJ Web of Conferences 126, 02024 (2016). <https://doi.org/10.1051/epjconf/201612602024>.
- [15] TOTEM Collaboration, G. e. a. Anelli, The TOTEM Experiment at the CERN Large Hadron Collider, J. Instrum. 3 (2008) S08007.
- [16] LHCf Collaboration, O. Adriani et al., The LHCf detector at the CERN Large Hadron Collider, JINST 3 (2008) S08006.
- [17] R. Bruce, C. Bracco, R. De Maria, M. Giovannozzi, A. Mereghetti, D. Mirarchi, 240 Bibliography S. Redaelli, E. Quaranta, and B. Salvachua, Reaching record-low β^* at the CERN Large Hadron Collider using a novel scheme of collimator settings and optics, Nucl. Instrum. Meth. A848 (2017) 19–30. <https://doi.org/10.1016/j.nima.2016.12.039>.
- [18] J. Baars, J. Van Der Brugge, J. Casse, J. Hamaker et al., The synthesis radio telescope at Westerbork, (1973). <https://doi.org/10.1109/PROC.1973.9255>.
- [19] The ATLAS collaboration. *Electron efficiency measurements with the ATLAS detector using the 2015 LHC proton-proton collision data*. ATLAS 2016. <https://cds.cern.ch/record/2157687/files/ATLAS-CONF-2016-024.pdf?version=1>.
- [20] The ATLAS collaboration. *Measurement of the photon identification efficiency with the ATLAS detector using LHC Run-1 data*. ATLAS 2016. https://arpi.unipi.it/retrieve/handle/11568/826405/204943/EPJC_76_666.pdf .
- [21] Stefano Manzoni. *Physics with photons with the ATLAS Run 2 data: calibration and identification, measurement of the Higgs boson mass and search for supersymmetry in di-photon final state*. Milano, 2017. <https://cds.cern.ch/record/2303078/files/CERN-THESIS-2017-303.pdf>.
- [22] W Lampl et al. *Calorimeter Clustering Algorithms: Description and Performance*. 2008. <https://cds.cern.ch/record/1099735/files/larg-pub-2008-002.pdf?version=1>.
- [23] ATLAS Collaboration, *Electron and photon reconstruction and performance in ATLAS using a dynamical, topological cell clustering-based approach*, Tech. Rep. ATL-PHYS-PUB-2017-022, CERN, Geneva, Dec. 2017. <https://cds.cern.ch/record/2298955>.
- [24] ATLAS collaboration. *Search for dark matter at $\sqrt{s} = 13$ TeV in finale states containing an energetic photon and large missing transverse momentum with the ATLAS detector*. 2017. <https://arxiv.org/abs/1704.03848>.